Forschungszentrum Jülich

Institut für Kernphysik

Principles and methods for γ-ray tracking with large volume Ge detectors

Lucian Mihailescu

Jül-3871

Berichte des Forschungszentrums Jülich 3871

Principles and methods for γ-ray tracking with large volume Ge detectors

Lucian Mihailescu

Berichte des Forschungszentrums Jülich ; 3871
ISSN 0944-2952
Institut für Kernphysik Jül-3871
D 5 (Diss., Bonn, Univ., 2001)

Zu beziehen durch: Forschungszentrum Jülich GmbH · Zentralbibliothek
52425 Jülich · Bundesrepublik Deutschland
☎ 02461/61-5220 · Telefax: 02461/61-6103 · e-mail: zb-publikation@fz-juelich.de

ACKNOWLEDGEMENTS

This work would not have been possible without the help and friendship of many people. My special gratitude goes to my supervisor and chef of the Nuclear Spectroscopy group in Jülich, Prof. Rainer Lieder for discussions, continuous support and the perfect working atmosphere. It was a great pleasure to have him as a supervisor. I am thankful to all members of his group, to my friends, Werner Gast, for inspiring discussions, not only about pulse shape analysis, for fruitful ideas, for his invaluable help during measurements and fine tuning of the electronics; Marcel Rossewij, for the implementation of algorithms on the PPADC; Hartmut Brands, for his help in setting up experiments and for his help for the acquisition and analysis of detector pulse shapes; Herbert Jäger for all kinds of technical support.

I am also grateful to B. Alefeld from the Institut für Festkörperforschung for assisting us with running the neutron scattering spectrometer HADAS.

Furthermore I gratefully acknowledge the EU support in financing the travels abroad under the TMR Network contract EBFMRXCT970123.

I thank all collaborators of the TMR project "Development of γ-ray tracking detectors" for lively discussions and comments.

My wife, Mihaela was the source of inspiration for my work. I thank her for everything.

Finally, I want to address special thanks to Radu Grosescu from the NMR laboratory in IFIN Bucharest. He gave me the first lessons on how to do experimental research. I hope to remember them properly throughout my carrier. He also encouraged me to start this thesis, actually this work would not have existed without his encouragements.

TABLE OF CONTENTS

Chapter

LIST OF FIGURES

Figure Page

LIST OF TABLES

ABSTRACT

Principles and methods for γ-ray tracking with large volume Ge detectors

This work presents an approach for the development of a high resolution detection system suitable for γ-ray tracking. To obtain an optimal energy resolution, large volume germanium detectors are considered. Since the most challenging problem for the development of a γ-ray tracking system is to achieve a high position resolution, this topic is emphasized in the present work. A large attention is devoted to the methods and algorithms which allow to extract the positions of γ-ray interactions by the analysis of detector pulse shapes.

CHAPTER 1

INTRODUCTION

Recent results obtained from experiments carried out with modern γ-ray spectrometer arrays like EUROBALL and GAMMASPHERE [1] have demonstrated the importance of advanced detector technology in progressing our understanding of nuclear structure phenomena. These arrays represent multi-detector arrangements of anti-Compton spectrometers, optimized for high energy resolution, high efficiency, and high peak-to-total ratio. For the European γ-detector array EUROBALL, composite detectors such as the CLOVER and CLUSTER detectors have been developed [1]. They represent a major step forward in the development of γ-detectors, allowing for an increase in efficiency and granularity. To optimize the performance of a γ-detector array for the study of highly excited nuclei produced in heavy-ion induced reactions, a careful consideration of high multiplicity γ-ray cascades emitted from the fast recoiling nuclei is required. In particular, one must be careful to minimize the degradation of the performance of the detector system caused by multiple hits and Doppler broadening. An improved position sensitivity is therefore required.

For γ-rays with energies up to 3 MeV, the dominant interaction modes are Compton scattering and the photoelectric effect. Conventional anti-Compton spectrometers, in which the separate Ge detectors are shielded against each other by surrounding anti-Compton detectors, can only suppress the Compton-scattered γ-rays. In composite Ge detectors, however, Compton-scattered events can be reconstructed, and the full energy can be obtained by summing the energies deposited in adjacent crystals (the so-called *add-back* mode of operation). In this way, the efficiency of a composite detector can be considerably increased with respect to that of the constituant detectors [1]. Nevertheless, false summing (the *add-back* of individual, not scattered events, interacting in adjacent crystals) causes a degradation of the photopeak efficiency and peak-to-total ratio. To avoid this erroneous *add-back*, scattered events must be discriminated from individual events by γ-ray tracking.

Gamma-ray tracking is a new concept, which is intended to improve the performance of the next generation of 4π γ-ray spectrometers [2]. Tracking arrays will consist of highly-segmented Ge detectors in which a detailed analysis of the charge collection process in the inhomogeneous fields of the individual crystals will allow a localization of the interaction positions. The position sensitivity added to the high energy resolution of the Ge detectors will make possible to reconstruct the scattering sequence of the γ-rays interacting with one or several Ge detectors of the array. The resulting possibility of discriminating between scattered events and individual hits gives rise to an improved photopeak efficiency and peak-to-total ratio by *adding-back* only scattered events. A higher spatial resolution will determine also an improved energy resolution if Doppler broadening plays a role. Furthermore, since it is no longer necessary to shield the detectors against each other to avoid scattering, a larger coverage of the total solid angle with Ge will become available, and hence a higher total efficiency can be achieved.

The main requirement for an application of γ-ray tracking concepts is the determination of all γ-ray interactions with high spatial and energy resolution. Actually, the main challenges for the γ-ray tracking project are to develop the detection system and to design the related analysis methods allowing to extract the interaction positions in a detector of high energy resolution. Besides, powerful digital signal processing electronics are needed, able to accommodate the complex pulse shape analysis algorithms to extract the required information.

The present work will focus especially on the detection principles for an efficient γ-ray tracking array, as well as on the development of methods for the analysis of the detector signals to obtain besides a high energy resolution, also a reliable determination of the positions of γ-ray interactions.

The next chapter will provide an overview, although not complete, of the main nuclear spectroscopy topics which can be addressed with a γ-ray tracking array. Bearing to the unprecedent detection sensitivity of such an array, surprising new phenomena are expected to be discovered.

Chapter 3 will present the major existing γ-detector arrays and will introduce the new concept of a γ-ray tracking array. Expected performances of such an array will be given.

To develop methods based on the analysis of detector pulse shapes, a reliable knowledge of the pulse shape formation in detectors is required. Chapter 4 will present the involved physical phenomena responsible for the formation of detector signals. An emphasis will be made on the charge collection process in germanium detectors, especially with regard to the anisotropy of the charge drift velocity which was not treated in the literature with respect to its importance for the charge collection process in Ge detectors.

Chapter 5, the most extensive part of this work will present the basic concepts and methods for pulse shape analysis to obtain an improved position sensitivity from segmented Ge detectors. Design principles of a segmented Ge detector for γ-ray tracking will be discussed. The chapter will also contain the digital methods necessary for the preprocessing of the detector signals, viz., the procedures for signal triggering and timing in a digital environment. For the analysis of detector signal shapes, the Wide-Band wavelet transform (WB4) will be introduced and therefore, the basic features of this transform will be presented. The chapter will close with the presentation of methods based on pattern recognition concepts for the identification of positions for single and multiple interactions.

The last chapter will give an overview on applications, other than nuclear structure physics, which might benefit from the use of such a γ-ray tracking detection system.

CHAPTER 2

TOPICS IN NUCLEAR SPECTROSCOPY

2.1 Introduction

Due to the complexity of the atomic nucleus, a many-body system with a not fully understood nucleonic interaction, a model to describe all features of the nuclei has not yet been found. This is also the reason why the understanding of the nuclear structure and the deduced models were driven mostly by experimental studies. Better experimental equipment, with more efficient detectors lead to the discovery of new, surprising aspects of the nuclear matter. Despite the big progress, there are still many unanswered questions about the behavior exhibited by nuclei under extreme conditions of isospin, spin, temperature and mass. An improved knowledge of the nuclear structure under extreme conditions will also allow for a better understanding of the formation and evolution of nuclear matter in the universe. Of special interest are n-rich nuclei towards the neutron drip-line for the *rapid neutron capture* process (r-process), which exists in conditions of supernovae, or during the decompression of neutron stars, as well as those towards the proton drip-line for the *rapid proton* induced reactions (rp-process), which takes place at the surface of accreting white dwarfs and neutron stars.

For many of these exciting studies, superior accelerators, eventually for radioactive beams to produce the relevant nuclei, and high efficiency, high resolution γ-ray detectors to study their structure are required. This chapter is intended to review some of the actual challenges in nuclear structure which can be addressed by experiments involving a high efficiency, high resolution γ-ray tracking detector array.

2.2 Nuclear structure under extreme conditions

Although the nuclei close to the stability line have been intensively studied, leading towards a significant progress in the understanding of the nuclear properties, an extrapolation of the models for nuclear systems under extreme conditions of spin, isospin, mass and temperature is questionable. Therefore new experimental investigations should be made of the nuclear structure under these conditions. In the following, various topics of nuclear structure research addressed by spectroscopic studies of the nuclei under extreme conditions will be reviewed.

2.2.1 Nuclei far from stability line

The study of nuclei with a proton-to-neutron ratio Z/N which takes extreme values with respect to this ratio for β stable nuclei is an important experimental and technical challenge. The recent projects to build accelerators for the production of radioactive beams are ambitious projects meant to fill this experimental gap. A better knowledge of these nuclei will give an important input for an improvement of the theoretical description of the nuclear matter. On the other hand, a better understanding of the nuclei far off the stability line will be of special importance for the study of nuclear astrophysics phenomena, especially those involving explosive conditions. By this, the unstable nuclei become very important for nucleosynthesis models, since in the highly instable, explosive conditions occurring in stellar processes, such instable nuclei are produced.

Halo nuclei and neutron skin Recent data showed the existence of a new structural phenomenon consisting of a core nucleus and a small number of weakly bound neutrons located at a considerable distance from the core. These are the so-called "halo nuclei". Examples are the 4n halo nucleus ^{8}He, the 2n halo nuclei ^{6}He,

^{11}Li, ^{12}Be, ^{14}Be, ^{17}B, the 1n halo nuclei ^{12}Be, ^{19}C and the 1p halo nuclei ^{8}B, ^{17}F, ^{17}Ne. The main reaction mechanisms used for the study of halo nuclei were break-up reactions.

The study of neutron halos will give the opportunity to understand various related nuclear aspects like the properties of diffuse neutron matter with significance also in the formation of neutron stars, the reaction mechanisms involving halo nuclei, new modes of excitation. Nevertheless, a full understanding of the interplay between the bound states and continuum requires an improvement of data on known halo nuclei as well as investigation of halos and expected neutron skins in heavier weakly bound neutron rich nuclei. For this, more intense beams are required, eventually radioactive beams, as well as γ-ray detectors of higher efficiency and selectivity.

Neutron and proton drip lines. The experimental evidence for the position of the neutron and proton drip lines exists only for lighter nuclei. Experiments are required for heavier nuclei to find the borders of the nuclear chart, and to determine the relative difference of the binding energies of the nucleons, providing information for the improvement of the theoretical models. In the case of the proton drip line, the Coulomb barrier is expected to increase the lifetime of nuclei, given the possibility to discover nuclei beyond the drip line. The study of deexcitation modes near the drip lines are also of interest.

The path of r-process. As far as known, type II supernovae and neutron star mergers are the astrophysical phenomena which are responsible for the creation of a large part of the heavy nuclei through the *rapid neutron capture* or r-process. The r-process involves unstable neutron rich nuclei, which forms heavy nuclei under a continuous capture of neutrons and β^--decays. To accurately estimate the abundance of elements synthesized in this process, the nuclei on the r-process path should be investigated. Since the population probability of these nuclei is very weak under experimental conditions, high efficiency γ-detectors are required.

The rp-process. The rp-process is a sequence of rapid proton captures which takes place in X-ray bursts produced by the hydrogen-rich shell of a low-rate accreting neutron star, and in X-ray pulsars which are formed by high-rate accreting neutron stars. In the first case, the rp-process converts the nuclei produced in the CNO cycle to ^{56}Ni, whereas in the second case, the formation of elements up to masses in the range of 80 to 100, even to 150 for high accretion rates is expected. For an understanding of these neutron star processes, information is needed about the properties of the odd-Z nuclei found on the rp-process path, which is close to the proton drip line. Of special interest are the lifetimes of the β^+-decay rates, reaction cross-sections, proton separation energies, level structures and isomeric states.

N=Z nuclei. A topic of particular interest is the investigation of the N=Z nuclei, both experimentally and theoretically. Since the protons and neutrons fill the same orbitals, a p-n interaction is expected, leading towards neutron-proton pairing. Theoretical studies suggest that pairing correlations become weaker with the temperature and angular momentum. Thus, for an odd-odd N=Z nucleus, a transition from T=1 to T=0 should occur with increasing momentum. Improving the experimental spectroscopic data of these nuclei up to the doubly magic nucleus ^{100}Sn, will give important insights about the nuclear shell structure.

Breakdown of magic numbers. The study of closed shell nuclei (nuclei with a magic number of neutrons or protons) from the stable nuclei to the nuclei far from the stability line indicates a variation in the shell ordering with the departure from the stability line. The experiments made on n-reach light nuclei have allowed to reach the neutron drip line. Experimental evidence exists that the Ne, Mg and Na nuclei with $N = 20$, are not magic any longer. There are theoretical studies indicating that very neutron rich nuclei have a potential with a smoother slope than the Woods-Saxon potential. As far as the consequences of this phenomenon are concerned, a reduction of the shell gaps, would allow many-particle, many-hole excitations to become energetically possible, leading to shape changes. Nevertheless, to obtain a better understanding, more experimental data are needed for nuclei around the shell closures for neutron as well as proton-rich nuclei.

2.2.2 Nuclear structure at high spins

Nuclei at high spins are produced following mainly nuclear fusion-evaporation reactions induced by heavy ions. The high angular momenta produced in these reactions have a direct impact on the internal structure of the highly excited nuclei. The study of the nuclei under these conditions will give valuable insight about the interplay between collective and single-particle motion.

Exotic shapes. Recent nuclear mean field calculations based on the cranking formalism were able to reproduce many of the properties related to the existence of superdeformed nuclei (SD) at high spins. Superdeformed nuclei are considered to have an elongated rotational symmetric shape with an ratio of the axes of 2:1. From these calculations, parameters like single-particle configurations, moments of inertia and quadrupole moments were well reproduced. Despite the success of the theoretical calculations, the field of superdeformed nuclei is still offering surprises. With the discovery of identical superdeformed bands in neighbouring nuclei, new questions arises about the underlying physics. Furthermore, in most of the heavy superdeformed nuclei, the superdeformed bands are not linked to normal deformed states which means that their excitation energies, spins and parities are not known. Only in a few nuclei in the A=190 region and in ^{143}Eu in the A=150 region linking transitions were found. The deexcitation of the SD bands proceeds at their lower ends when high-energetic transitions to normal deformed states can compete with the fast in-band E2 transitions. It is assumed that the depopulation spreads over a large number of weak transitions. Only a few transitions are strong enough (a few percent of the SD band intensity) to be observable with present day arrays like EUROBALL and GAMMASPHERE. A much more sensitive γ-detector array is required to observe the weak linking transitions.

The mean field calculations also predicts the existence of very large deformations, what is called *hyperdeformations*, with a ratio of the main axes of 3:1 for nuclei at even higher spins. Though, various experiments up to now failed of identifying the rotational bands characteristic of hyperdeformed nuclei, the small probability of populating such high spin nuclei would require superior, more efficient γ-detector arrays.

High spin isomers. Due to the conservation of the angular momentum projection, K, on the symmetry axis, the deformed nuclei in the Rare Earth region, reveal long-lived isomers at high spin. Though, in recent experiments in the mass A=180 region, new unexpected deexcitation modes of high-K isomers were observed. They are characterized by the decay of high-spin isomers with large values of the K quantum number into K=0 bands by transitions which should be highly K-forbidden. Thus, various questions are posed concerning the limits of K-forbiddeness, whether K remains a good quantum number at very high angular momenta, and what are the underlying processes in the deexcitation of the high-K levels? Possible explanations for the K-forbidden decays are tunnelling through barriers in the $\beta - \gamma$ plane, and the reorientation of their angular momentum from an alignment along the symmetry axis to an alignment along the rotation axis.

So far it was only possible to study high-spin isomers in p-rich nuclei. For a complete representation of the high spin isomers new experiments are necessary for the study of neutron rich nuclei. For proton rich nuclei a surprising linear correlation was found between the hindrance factor per degree of K-forbiddeness f_ν ($\nu = \Delta K - L$) and the product between the valence proton and neutron number. An interesting question is how the hindrance factor f_ν changes for n-rich nuclei.

Magnetic rotations. In recent experiments on weakly deformed nuclei close to magic numbers in the mass regions 200, 140 and 110, dipole bands consisting of enhanced magnetic dipole transitions have been found. Since the nuclei are only weakly deformed or even spherical, these rotational bands have been explained by the existence of a large magnetic dipole moment which breaks the symmetry, and induces a rotational direction. The dipole moment rotates around a fixed angular momentum axis, creating the experimentally observed magnetic dipole radiation. This phenomenon was named “magnetic rotation”. Magnetic rotations are expected to exists in many other nuclei near magic number.

2.2.3 Nuclear structure at high temperature

With increasing the excitation energy of the atomic nucleus, a transition from ordered to chaotic motion of the nucleons takes place. The transition appears at relatively small temperatures, being accompanied by a large mixture of states. Whereas the mean field approximation characterize the quantic structure of the low-energetic nuclear states, the quantum chaos is represented by the random matrix theory. For the development of the involved theories, it is important to determine the exact temperature at which the transition from order to chaos takes place, as well as the change of the excitation modes with increasing temperature. In the following, one particular aspect related to changes appearing with increasing temperature is reviewed.

Rotational damping Due to level density increase with the excitation energy, the coupling between the rotational bands will become more pronounced. As a result, the excited rotational states will have a large mixture of rotational frequencies. This phenomenon is known under the expression "*rotational damping*". For rare earth nuclei it was discovered that rotational damping occurs roughly at an excitation energy of 1MeV over the yrast band. For a better understanding of the onset of band mixing, more sensitive spectroscopic data are required.

CHAPTER 3

CONCEPT OF A γ-RAY TRACKING ARRAY

3.1 Introduction

The development of in-beam γ-ray spectroscopy took place in close relation with the development of detection techniques. The introduction of germanium detectors in the late sixtieth increased the resolution performances by a factor of 15. This gave a significant advance in the study of nuclear structure leading towards the discovery of the backbanding phenomenon [3, 4]. The construction of arrays of composite Ge detectors along with BGO (bismuth germanate) escape-suppression shields detectors in the eightieth gave an improvment of the peak-to-total ratio by a factor of ≈ 4. The use of arrays of anti-Compton spectrometers made possible the discovery of superdeformed bands in medium-heavy nuclei at high spins [5]. The later technological advances, with the construction of the large arrays EUROBALL III in Europe and GAMMASPHERE in the USA, allowed for a detailed investigation of e.g., superdeformation, magnetic rotation, nuclei around ^{100}Sn. The physics topics presented in the previous chapter suggest that detector arrays of higher efficiency and better energy resolution are required. This can be achieved by using an array of large segmented Ge detectors which possess γ-ray tracking capabilities. This chapter will present the main features of the γ-ray detector arrays and will introduce the new concept of γ-ray tracking detector arrays.

3.2 Detector arrays for nuclear spectroscopy

The existing γ-ray detector arrays represent multi-detector arrangements of anti-Compton spectrometers, optimized for high energy resolution, high efficiency, and high peak-to-total ratio. The excellent energy resolution of the Ge detectors is degraded in in-beam spectroscopy experiments due to a Doppler broadening of the γ-lines resulting from the fact that the nuclei are produced in nuclear reactions, flying usually with a velocity of $v/c \approx 4\%$, and due to the large solid angle of the Ge detectors. A better definition of the γ-ray emission angle than the one provided by the detector opening would allow for a reduction of the Doppler broadening. Since for γ-rays with energies of up to $\approx$ 4 MeV, the dominant interaction modes are the Compton scattering and photoelectric effect, the detection systems are required to allow for a reduction of the Compton background in order to obtain a higher peak-to-total value.

The conventional anti-Compton spectrometers are formed by Ge detectors shielded against each other by surrounding anti-Compton detectors. This arrangement can only suppress the Compton-scattered γ-rays. The composite Ge detectors used in EUROBALL however, consist of clusters of Ge detectors in a tight geometry and are surrounded by common BGO anti-Compton shields. Using this arrangement, the Compton-scattered events can be reconstructed, and the full energy can be obtained by summing the energies deposited in adjacent crystals (the so-called *add-back* mode of operation). In this way the efficiency of a composite detector can be considerably increased [1]. Unfortunately, if several γ-rays will interact in the same cluster of detectors, a decrease in the P/T will occur due to the false summing of the energies of the detectors. For a correct assignment of the γ-ray interactions in the detectors to a certain incident γ-quanta, a method to "track" the interaction sequence will have to be introduced.

3.2.1 Fundamental parameters of γ-detector arrays

The features of a γ-detector array can be defined by three main parameters: the energy resolution ΔE_γ, the total photopeak efficiency P_{ph} and the peak-to-total ratio P/T. Ultimately, these three parameters will determine the figure of merit of the γ-detector arrays which is the *observational limit*, defined as the minimum intensity of a γ-ray transition that can be detected. The performance of a γ-detector array depends on the intrinsic parameters of the array, on the detectors composing the array, as well as on the existing experimental conditions. Among the experimental conditions, the multiplicity of the γ-rays will influence the photopeak efficiency and peak-to-total ratio, whereas the velocity of the recoils produced in heavy-ion reactions will cause a Doppler shift of the γ-ray lines, influencing the energy resolution. Nevertheless, if the angle of the γ-ray emission is known, correction for the Doppler shift can be made.

In the following, the fundamental parameters characterizing a γ-detector array will be defined.

Energy resolution The total energy resolution of the detector array is determined by the intrinsic resolution of the individual detectors $\Delta E_\gamma^{(intr.)}$, and by the energy spread due to the Doppler effects which takes place for in-beam experiments $\Delta E_\gamma^{(Doppler)}$:

$$\Delta E_\gamma = \sqrt{(\Delta E_\gamma^{(intr.)})^2 + (\Delta E_\gamma^{(Doppler)})^2} \tag{3.1}$$

The typical energy resolution of a Ge detector is $\Delta E_\gamma = 2$ keV for an energy of $E_\gamma = 1.33$ MeV. One should note that if segmented Ge detectors are used, and the total energy E_γ is calculated as a sum of the energies deposited in the various segments $E_\gamma^{(i)}$, the resolution is calculated:

$$\Delta E_\gamma^{(intr.)}(E_\gamma) = \sqrt{\sum_{i=1}^{N_S} \Delta E_\gamma^{(i)}(E_\gamma^{(i)})} \tag{3.2}$$

where N_S is the number of segments which fire.

The Doppler effects depend on the existing experimental conditions although it can be reduced by having known more precisely the angle at which the γ-ray is emitted. In principle, three factors contribute to the Doppler broadening: 1.) the finite solid angle within which the incident γ-ray interaction is detected; 2.) the angular spread of the recoiling nuclei and 3.) the variation of the recoils velocity due to the slowing down in the target. The first factor is at present the most significant component in the final energy resolution. Therefore, the Doppler broadening can be strongly reduced by minimizing the solid angle of detection. Presently, the solid angle can only be reduced by an increase of the distance between target and detector. For tracking detectors however, the acceptance angle can be so much reduced that the second factor will become dominant, requiring the measurement of the recoil direction. A relation which gives the connection between the angle of emission θ_γ, the half-opening angle of detection $\Delta\theta\gamma$ and the Doppler broadening $\Delta E_\gamma^{(Doppler)}/E_\gamma$ is:

$$\frac{\Delta E_\gamma^{(Doppler)}}{E_\gamma} = 2\frac{v_r}{c}\sin\theta_\gamma \sin\Delta\theta_\gamma \tag{3.3}$$

where v_r is the recoil velocity.

If the directions of the recoils have an angular spread, the precision of the angle θ_γ will be further limited. Moreover, the relative variation of the recoil velocity which is typically $\Delta v_r/v_r \approx 0.1$ will also limit the attainable energy resolution. Nevertheless, the last two factors can be minimized by measuring the recoil angle with position sensitive recoil detectors and by determining the recoil velocity v_r by using time-of-flight techniques.

Photopeak efficiency and Peak-to-total ratio The absolute efficiency of a γ-ray detector system ϵ_{abs} is defined as the number of events recorded divided by the total number of quanta emitted by the source. In a detector array, this absolute efficiency is related to the intrinsic efficiency ϵ_{int} of the individual detectors by:

$$\epsilon_{abs} = \frac{N\Omega}{4\pi}\epsilon_{int} \tag{3.4}$$

where N is the number of detectors and Ω is the solid angle covered by an individual detector when viewed from the source. The intrinsic detector efficiency is defined as the ratio of the number of recorded events to the number of quanta incident on detector. In general, ϵ_{int} depends on the detector material, its geometry (thickness) and the energy of the incident γ-ray. Since the detection of γ-rays which deposit their whole energy are of interest, the important parameter which represents the detection efficiency is the photopeak efficiency ϵ_{ph}. The value of the photopeak efficiency ϵ_{ph} is proportional to the absolute efficiency ϵ_{abs}, with a proportionality factor given by the peak-to-total ratio P/T:

$$\epsilon_{ph} = \frac{P}{T}\epsilon_{abs} \tag{3.5}$$

The peak-to-total ratio P/T for a γ-ray of energy E_γ is the ratio between the number of photopeak events and the total number of detected events, which include the photopeak and Compton background.

Both *photopeak efficiency* and *peak-to-total ratio* depend on the energies of the γ-rays, but are affected by the multiplicity of the γ-ray events as well. The peak-to-total ratio $(P/T)_{M_\gamma}$ for γ-rays of multiplicity M_γ can be approximated by the relation:

$$\left(\frac{P}{T}\right)_{M_\gamma} = W(M_\gamma)\left(\frac{P}{T}\right) \tag{3.6}$$

where (P/T) corresponds to a multiplicity $M_\gamma = 1$ and $W(M)$ is the probability of having non-overlaping interactions from different incident γ-rays of multiplicity M_γ (the isolated hit probability).

3.2.2 The observational limit

For an objective comparison of the sensitivities of various γ-ray detector arrays, the *observational limit* was introduced as the *figure-of-merit* of γ-detector arrays for high multiplicity events. The *observational limit* is defined as the minimum intensity of a γ-ray transition which can be observed. The *observational limit* is determined by the minimum number of counts a γ-ray peak has to have on a fluctuating background to be statistically significant. A typical nuclear spectroscopy experiment involves a cascade of M_γ transitions occurring in the deexcitation of a highly excited nucleus. Usually, the number of detected events (called fold) F is less than the multiplicity M_γ. In this context, it is of interest to determine the number of counts $N_P^{(F)}$ detected in a F-dimensional peak, given the intensity I_0 of the cascade involving M_γ transitions. This can be estimated from:

$$N_P^{(F)} = \left(0.76\frac{P}{T}\right)^F \frac{I_0 N_c^{(F)} F!}{M!} \tag{3.7}$$

The factor 0.76 results from the consideration of a F-dimensional volume element determined by the FWHM of the γ-ray peak. The value $N_c^{(F)}$ represents the number of F-fold coincidences obtained by combining the measured F'-fold coincidences with $F \leq F' \leq M$ as:

$$N_c^{(F)} = \sum_{F'=F}^{M} N(F')\frac{F'!}{F!(F'-F)!} \tag{3.8}$$

The distribution in the number of F'-fold coincidences $N(F')$ depends mainly on the multiplicity M_γ and the array photopeak efficiency ϵ_{Ph}. The intensity I_0 is a relative value, being normalized to the sum of intensities of all cascades which feed the ground state.

For an estimation of the background on which the peak stands, generally, a simple model is used, which takes into account the average separation between peaks S_γ, the energy resolution ΔE_γ and the multiplicity M_γ[6]:

$$N_B^{(F)} = \left(\frac{\Delta E_\gamma}{S_\gamma}\right)^F \frac{N_c^{(F)}}{M_\gamma^F} \tag{3.9}$$

This relation was obtained assuming that the background under a peak is not correlated with events from the other peaks, which means that when an energy window is set on a particular peak, the background component will not be coincident with the other γ-rays from the corresponding cascade. This is a rather correct approximation, since a large part of the background results from the collective transitions in the quasi-continuum. A better approximation which takes into account also the correlated background from Compton contributions along with statistical and feeding γ-rays is presented in [5].

Based on Eq. 3.8 and Eq. 3.9, one can approximate the number of counts in a peak with respect to the number of counts in the background as:

$$\left(\frac{N_P}{N_B}\right) = I_0 R_0 (0.76R)^F \tag{3.10}$$

where

$$R = \left(\frac{S_\gamma}{\Delta E_\gamma}\frac{P}{T}\right) \tag{3.11}$$

is the resolving power of the spectrometer [6]. The factor R_0 represents the background reduction obtained by using various selective devices or informations.

Finally, the *observational limit* $I_{0,min}$ of a spectrometer is found when the minimum conditions necessary to imply the existence of a peak are satisfied. These conditions are fulfilled when the ratio of Eq. 3.10 is statistically significant, i.e. the number of events in the photopeak are three times larger than the standard deviation of the background:

$$N_P \geq 3\sqrt{N_B}. \tag{3.12}$$

The *observational limit* $I_{0,min}$ will become:

$$I_{0,min} = \frac{9}{N_P^{(F)} R_0 (0.76R)^F} \tag{3.13}$$

For a given multiplicity M, $I_{0,min}$ will be mainly a function of the *photopeak efficiency* ϵ_{ph} contained in $N_P^{(F)}$, and the energy resolution and the *peak-to-total ratio* P/T contained in the resolving power R. Since the resolving power R is decreasing with increasing the fold F, whereas the photopeak efficiency increases with F, a certain value F_{optim} will minimize the observational limit. Given R, ϵ_{ph}, and the multiplicity M_γ, F_{optim} can be determined using Eq. 3.13.

3.2.3 Present γ-detector arrays

Since around 1980, the complexity of the γ-detector arrays increased continuously. Going through different development phases, in the present days, the largest detector arrays are the European project EUROBALL [7] and GAMMASPHERE of the USA [8]. For a larger photopeak efficiency, a larger fraction of the solid angle had to be covered by the Ge detectors. The number of Ge detectors used in arrays increased to 239 for the EUROBALL array, and 110 for the GAMMASPHERE array. On the other hand, to optimize the peak-to-total value, the Ge detectors were sorrounded by scintillators able to supress the γ-rays which are Compton scattered outside the Ge detector volume. In this way it was possible to reduce the Compton background. For most existing arrays, bismuth germanate (BGO) has been used as escape suppression scintillator. Although the energy resolution of this scintillator is not outstanding, it has a very high efficiency due to its high density and Z-number so that compact anti-Compton detectors for the absorption of the Compton scattered γ-rays can be built. The features achieved with these detector arrays are summarized in table 1. The table presents also the features of the third biggest γ-detector array, GASP [9] which is installed at the Laboratori Nazionali di Legnaro - Italy.

The EUROBALL array was designed based on the idea to increase the detection efficiency by using composite Ge detectors. The composite detectors are formed by close packing a number of Ge detectors, and using escape-suppression shields being placed around the whole "pack" of Ge detectors. By "adding-back" the energies of coincident events in the composite detectors, a higher photopeak efficiency can be achieved. Two designs of composite detectors were developed for the EUROBALL array: the CLOVER detector [7] and the CLUSTER detector [10]. The whole array consists of 15 CLUSTER detector, 24 CLOVER detectors and 30 individual escape-suppressed Ge detectors.

Table 1 Parameters of the present largest γ-detector arrays for $E_\gamma = 1.33$ MeV, $M = 30$, $v/c = 0.025$ and $S_\gamma = 70$keV (from [1])

Array	N_D	ΔE_γ $[keV]$	$\left(\frac{P}{T}\right)_M$	ϵ_{ph}	R	F_{optim}	$I_{0,min}$
GASP	40	6.9	0.61	0.028	6.2	4	$2 \cdot 10^{-4}$
EUROBALL	239	6.0	0.55	0.088	6.4	5	$5 \cdot 10^{-5}$
GAMMASPHERE	110	6.3	0.56	0.092	6.2	5	$5 \cdot 10^{-5}$

The US project GAMMASPHERE [8] is using 110 individually escape-suppressed Ge detectors. About 80 detectors have a two-fold segmentation of the outer electrode resulting in a reduction of the Doppler broadening, thus increasing the energy resolution. The main parameters of this array are presented in table 1.

3.2.4 Requirements for the next generation of γ-detector arrays.

The existing large γ-ray spectrometers are optimized for the study of high-spin states, characterized by high multiplicity γ-ray cascades. However, for the study of nuclei far from the stability line, radioactive beams of low intensity will be used.

For experiments involving the study of rare γ-decays or involving radioactive beams of low intensity, new detector arrays have to be developed optimized for a high total photopeak efficiency, retaining the requirements for optimum energy resolution and peak-to-total ratio.

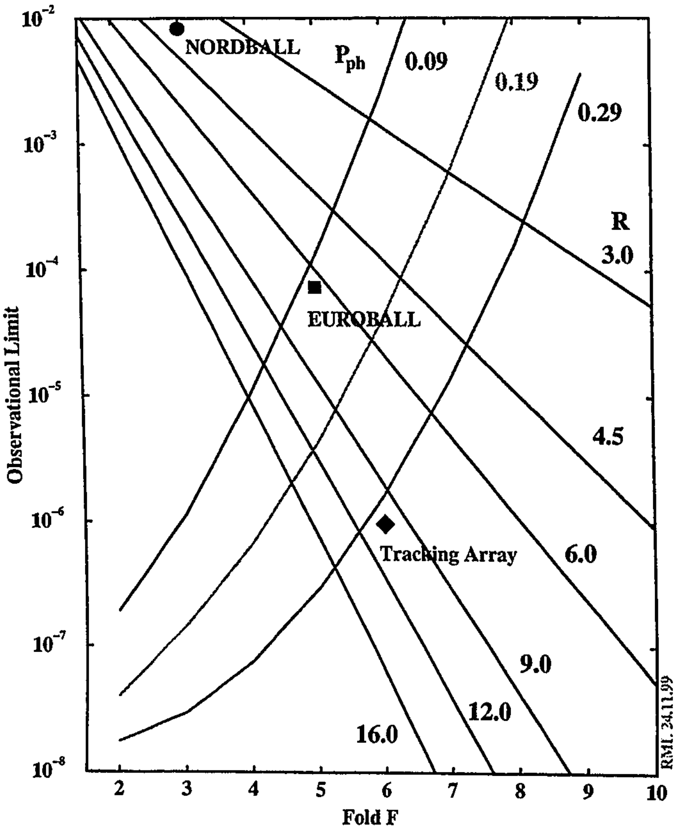

Figure 1 Observational limits for two built γ-detector arrays compared with the new array based on γ-ray tracking (Courtesy of R. Lieder).

3.3 A detector array based on γ-ray tracking

3.3.1 The concept of γ-ray tracking

For the present-days γ-detector arrays used in in-beam spectroscopy, a strong limitation in the achievable efficiency comes from the limited solid angle covered by the Ge detectors around the source, since the escape-suppression detectors cover already roughly 50% of the total solid angle of 4π, and from the fact that a large number of γ-rays undergo Compton scattering and are only partially absorbed by the Ge detectors. Ideally, all γ-rays emitted from the source in a cascade with multiplicity M_γ should be detected, being required a 4π solid angle coverage with Ge detectors of large thickness. This could be achieved by eliminating the escape-suppression elements formed by BGO scintillators. A step toward the reduction of the solid angle occupied by the BGO shields was already made by the developement of composite detectors. Unfortunately, for a high multiplicity M_γ there exists a high probability of having multiple incident γ-rays interacting in the same "cluster" of Ge detectors. In this case, the advantage offered by the possibility of "adding-back" the energies from neighbouring detectors diminishes since a discrimination between Compton interactions induced by one single incident γ-ray and the interactions produced by different incident γ-rays in the same "cluster" is not possible. Therefore, the "add-back" procedure will lead to a wrong summing of the energies of different incident γ-rays.

The concept of *γ-ray tracking* offers a mean to get around these problems, by using the knowledge on the Compton scattering process, which is the most important interaction of γ-rays with the germanium material at the energies of interest for nuclear spectroscopy. Theoretically, if the energies and positions of all interactions induced by sequential multiple Compton scatterings are known, the Compton scattering formula can be used to "track" back the sequence of Compton scatterings ending with a photoabsorbtion when the energy is low enough. Though, there are limitations on one hand, in the achievable energy and position resolution, and on the other hand, in the Compton scattering process which does not give an accurate relation between the energy of the incoming γ-ray, the energy of the scattered γ-ray and the scattering angle, due to scattering on bound electrons which have various angular momenta. These uncertainties can be overcome to a certain extent by utilising statistical information provided by the Klein-Nishina formula. In this way, algorithms for γ-ray tracking can provide information about the Compton and photoelectric interactions which belong to the same incident γ-ray, allowing to recover the initial energy of the incident γ-ray, and to determine the position of the first Compton interaction in the detector. Various algorithms have already been developed which, assuming a series of energy and positioning resolutions are able to "track" the γ-rays [11, 12, 13].

However, as it will be discussed below, the most sensitive topic of the γ-ray tracking concept and its implementation is the requirement for a superior spatial position resolution in a high resolution Ge detector. To some extend, this can be achieved with an increased granularity of the detector array, obtained by segmenting the detector electrodes and having for each segment a high resolution acquisition channel. This is only a partial solution since, for an efficient γ-ray tracking, a higher position resolution is needed which the segmentation of the electrode can not cover due to technical limitations which does not allow an extremely high-fold segmentation. For a superior position sensitivity, a digital analysis of the segment pulse shapes has to be employed.

3.3.2 Features of the tracking detector array

A detector array based on γ-ray tracking should be formed by a complete spherical shell containing medium-segmented Ge detectors (around 30 segments/detector) which, for best performance, are assumed to be coaxial n-type Ge detectors. Due to the large coverage of the full solid angle ($\approx 80\%$), the γ-ray tracking array is expected to have a large photopeak efficiency. Instead of using escape-suppression detectors, the improvement of the P/T will be achieved by γ-ray tracking. Due to the increased granularity of the detectors by segmentation, the probability of having interactions produced by different incident γ-rays in the same detection element (the segment) is strongly reduced. The possibility of correctly reconstructing the events will then depend mostly on the performance of the tracking algorithm which, at its turn, will depend on the achievable positioning resolution.

The figure-of-merit of a tracking detector is expected to improve by two orders of magnitudes in comparison to that of the present-day γ-detector arrays. For a shell of tracking detectors, with an inner radius of $20cm$, for a γ-ray multiplicity $M_\gamma = 30$, assuming a conservative positioning resolution of $\delta r = 5mm$, it is expected to reach a photopeak efficiency of $\epsilon_{ph} = 24\%$ and a peak-to-total $P/T = 58\%$ [11]. This would lead toward an observational limit of $\approx 10^{-6}$, which represents an improvement by two orders of magnitude with respect to the current EUROBALL array.

Another big advantage of a γ-tracking array is its compactness. The intelligence involved in pulse shape analysis and tracking algorithms will make possible to separate Compton interactions within small distances even for a large multiplicity of the incident γ-rays. Accordingly, the shell of detectors can have a small distance to the source, providing a significant reduction of the amount of detection material required.

Finally, by employing γ-ray tracking and pulse shape analysis, the first γ-ray interaction will be identified with a good position resolution which allows an accurate estimation of the direction of the incident γ-ray. The Doppler broadening is proportional to the obtainable position resolution, hence a significant improvement of the energy resolution is expected.

3.3.3 Detector requirements

In order to allow for an efficient implementation of γ-ray tracking methods, some basic detector requirements have to be fulfilled. Since for tracking, the most important relation is the Compton scattering formula, the parameters involved in this formula should be determined as well as possible. Thus, the energies and positions of the interactions are the important values which should be given with good resolution by the detection system.

Energy resolution and efficiency For general applications of γ-ray spectroscopy, the detection efficiency and energy resolution are the most important parameters to be optimized. Particularly for a reliable γ-ray tracking implementation, the energy deposited in each interaction has to be known with a high accuracy. In table 2 some important parameters which determine the efficiency and attainable energy resolution for a few crystals used in γ-ray detection are presented. The problem with most high-Z semiconductors is the high rate of charge trapping which, depending on the position of interaction between the electrodes, leads toward incomplete charge collection. Despite their high efficiency, this problem makes such semiconductors unsuitable for high-resolution spectroscopy. The use of Ge crystals cooled to liquid nitrogen (LN2) temperatures appears to be at present the best choice for an

Table 2 Features of materials used for γ-ray detectors [15].

Crystal	Z	Density $[g/cm^3]$	Charge transport	Energy gap @300K[eV]	Ioniz. mean en.@77K[eV]	Dielectric constant
Ge	32	5.327	good	0.664	2.96	16
Si	14	2.328	good	1.124	3.62	11.9
Diamond	6	3.515	poor	5.5	13.1	5.7
CdTe	48/52	5.86	poor	1.475	-	10.2
GaAs	31/33	5.318	poor	1.424	4.3	15.7

optimum performance with respect to efficiency and energy resolution. Besides, there exist reliable technologies of producing large, high-purity Ge single crystals necessary for high- efficiency detectors. Pertaining to its high purity, the depletion of Ge detectors can be made at reasonable low electriv fields, which creates the basis for building large detectors whithout the need to increase the applied bias voltage which would otherwise give increased leakage currents.

The most direct way to increase the efficiency is to use a high density, high Z material, as well as to increase the detection volume. However, as one can see in table 2, the highest Z, high density materials like CdTe or CdZnTe do not offer a high energy resolution. Furthermore, at present only small detectors can be produced (i.e. with the size of $\approx 9cm^3$). The best option for both high energy and intrinsic efficiency is the use of the germanium crystal. In the following, a few comments will be made for an optimization of the efficiency for the use of using high-purity germanium crystal as detector.

To device a semiconductor detector, electrodes have to be made by creating doped regions, (p^+) for one electrode and (n^+) for the other. By applying a reversed electric bias to the diode, the impurities within the detector volume are depleted, and the electrodes are ready to detect the charge carriers produced by a γ-ray interaction inside the depleted detector volume. Ideally, to minimize the volume of the "dead" material, the doped regions should be as thin as possible. For germanium detectors this is achieved by creating the (p^+) electrode through implantation of a thin layer $(50\mu m)$ with boron atoms. Unfortunately, for the creation of the (n^+) electrode in Ge, no reliable method of using implantation technique exists. Although there are studies to use phosphorus implantation or amorphous germanium to create the (n^+) electrode [14], the only reliable and stable method is the use of drifted lithium. On the expense of a thickness of up to $500\mu m$, the lithium drifted electrodes are stable in the annealing process. As a consequence, the area of the (n^+) contact should be minimized. The best way to do this is to use a Ge detector of coaxial geometry, with the (n^+) contact covering the interior cylindrical hole of the detector. This imposes the use of a n-type germanium crystal (Ge crystal with n-type impurities), since for an efficient depletion of the whole volume at reasonable electric fields, the sign of the potential at the inner hole should be the same as that of the spatial charge produced after the depletion of the impurities. Besides, the sign of the potential applied at a contact determines the type of dopant of that contact. Another advantage of using n-type Ge is that the detector would be less affected by the neutron damage, which is a sensitive issue for in-beam experiments.

Position resolution A good energy resolution and high efficiency were always the main requirements for γ-ray spectroscopy, whereas the requirement to determine the γ-interaction positions is particular for the γ-ray tracking concept. Most tracking simulations suggest an increased performance of the tracking algorithm if a better positioning resolution is achieved [12]. Normally, a position resolution of $1-2\,mm$ would offer acceptable tracking performances. Prior to this work no techniques were developed to obtain the interaction position from a large Ge detector to this level of accuracy. Actually the largest part of the present work will study the possibilities to achieve such a high position resolution using Ge detectors.

The standard way to gain information about the interaction position from a semiconductor detector is to make an electrical segmentation of the electrodes. Assuming segments formed by cells or voxels of 2mm each side, for a standard detector 7cm long and 6cm diameter, a number of ≈30,000 elements are imposed. Besides that, only an azimuthal and longitudinal but no radial segmentation can be achieved for a cylindrical Ge detector. Anyway, a very high-fold segmentation would create serious technical difficulties as it will be explained subsequently. Germanium detectors for high resolution spectroscopy are operated in a high vacuum, low temperature environment. Therefore, it is difficult to accommodate the high resolution transmission lines to read-out the segments, and to provide the large number of *feed-throughs* for vacuum. Consequently, the detectors should be designed to have a medium-fold segmentation, like 20 to 40 segments. Improved position resolution will be achieved by employing methods to analyze the shape of the detector segments pulses. The features needed to discriminate the various pulse shapes, and the methods to deduce the interaction positions by pulse shape analysis will be presented in chapter 5.

CHAPTER 4

INVESTIGATION OF THE SIGNAL FORMATION IN GERMANIUM DETECTORS

4.1 Introduction

The knowledge of the detector signal formation is essential for the development of pulse shape analysis methods, and for improvements in the detector design to obtain superior energy and position resolution. For this, a good understanding of the involved physical processes is required. Moreover, the pulse shape analysis methods for position determination requires reliable pulse shape simulations for a concise representation of the characteristic signal features, and to substitute intensive measurements of experimental detector pulse shapes. In this context, it is important to have a good control on the charge carrier collection, which involves a reliable representation of the charge carrier drift velocity, as well as of the electric fields inside the Ge detector.

This chapter will review the significant aspects involved in the signal formation. An emphasis will be put on the charge carrier drift velocity, with the study of the drift velocity anisotropy in Ge material, since its effects on the pulse shapes of Ge detectors were not previously considered in the literature. Therefore, a method for a realistic calculation of the electrons drift velocity will be presented, and the corresponding pulse shape simulation results will be compared with experimental signals obtained with a large volume closed-end Ge detector.

4.2 Interaction of γ-radiation with Ge detectors. Charge carrier production.

4.2.1 Interaction of γ-radiation with a Ge material

Although γ-radiation has various interaction mechanisms in matter, for the range of energies which are of interest for nuclear spectroscopy, only four mechanisms are relevant: *photoelectric effect*, *Compton scattering*, *pair production* and *Rayleigh scattering*. In the following, these mechanisms will be reviewed, pointing to the relevant features for γ-ray detection, as well as for tracking.

Photoelectric effect The photoelectric effect is the main interaction mechanism for γ-rays at low energies (up to about 200 keV for Ge). The γ-quantum interacts with an atom, the entire γ-ray energy being transferred to a bound electron which leaves the atom. The energy of the produced free electron (*photoelectron*) is given by the difference between the energy of the γ-quantum $h\nu$ and the binding energy E_b:

$$E_e = h\nu - E_b \tag{4.1}$$

For conservation of the impulse, the nucleus has to take over most of the impulse. Therefore, the γ-quanta are predominantly absorbed by K and L electrons. Part of the binding energy E_b will be transferred to X-rays emitted from the atom when the vacancy left by the first photoelectron will be filled by a less-bound electron. The X-rays are in turn absorbed by other atoms producing further photoelectrons. For γ-rays interacting photoelectrically with the detector, no tracking is needed, since the whole energy of the γ-ray is released in only one step. However the interaction position has to be determined. The estimation of the initial direction of the γ-ray will only be possible assuming an emission from a known source (the target).

Compton scattering The Compton scattering is the predominant interaction process for γ-rays of energies between about 200keV and 5-6MeV for germanium. For example, a γ-ray of 1.33MeV will undergo on average 3 Compton interactions before being absorbed by a photoelectric effect. In a Compton interaction, the γ-ray scatters on a weakly bound electron (quasi-free), transferring only part of its energy and impulse, the remaining energy and impulse being transferred to a scattered γ-ray. Neglecting the binding energy of the electron, the energy of the scattered photon due to Compton scattering of a photon of initial energy $h\nu$ at an angle θ is:

$$h\nu' = \frac{h\nu}{1 + \frac{h\nu}{m_0 c^2}(1 - \cos\theta)} \tag{4.2}$$

with m_0 being the rest mass of the electron, and c the speed of light.

The Klein-Nishina formula predicts the angular distribution of the scattered γ-rays. The differential cross section reads:

$$\frac{d\sigma}{d\Omega} = Zr_0^2 \left(\frac{1}{1+\alpha(1-\cos\theta)}\right)^2 \left(\frac{1+\cos^2\theta}{2}\right) \left(1 + \frac{\alpha^2(1-\cos\theta)^2}{(1+\cos^2\theta)[1+\alpha(1-\cos\theta)]}\right) \tag{4.3}$$

where r_0 is the classical electron radius and $\alpha = h\nu/m_0c^2$. The Compton scattering plays an important role in γ-ray tracking. Using the Compton scattering formula and Klein-Nishina formula it is possible to predict the scattering sequence of an incident γ-ray if all positions and energies of the interactions are known. Moreover, using the Compton scattering formula it is possible to predict the direction of an incident γ-ray up to the surface of the cone made by the angle of the first Compton interaction. If a statistical number of events are detected, by analyzing the intersection of the cones, an imaging of the source would be possible.

Pair production Although production of electron-positron pairs is possible in the electrostatic field of the nuclei for γ-rays with energies exceeding twice the rest mass of the electron (1.02MeV), a significant cross section for this interaction mechanism takes place only over 4-5MeV in Ge. In the pair production, the energy of the γ-ray is used to create the $e^+ - e^-$-pair, the remaining energy being transferred to the created electron and positron as kinetic energy, and part of the impulse is transferred to the nucleus. After loosing its energy in the detector material through ionisations, the positron will annihilate, giving rise to two 511keV gammas.

Rayleigh scattering Rayleigh scattering is an elastic scattering of γ-rays which occurs at low energies. In general, with a cross section at least one order of magnitude smaller than that of the photoelectric effect, the Rayleigh scattering is important for the tracking of the γ-rays due to the fact that the direction of the γ-ray is changed without loosing energy, making it in principle difficult to apply the tracking concept. Fortunately, since occurring at low energies, the Rayleigh scattered γ-ray will be absorbed at a short distance by a photoelectric effect.

4.2.2 Production of charge carriers in germanium

The photoelectrons produced following a γ-interaction in the Ge detector loose their energy in the detector material through ionizations and excitations according to the formula derived by Bethe for the linear stopping power S_c [16]:

$$\begin{aligned} S_c = -\left(\frac{dE}{dx}\right)_c = \; & \tfrac{2\pi N Z e^4}{m_0 v^2} \left[ln \tfrac{m_0 v^2 E}{2I^2(1-\beta^2)} - (ln2)(2\sqrt{1-\beta^2} - 1 + \beta^2) + \right. \\ & \left. (1-\beta^2) + (1-\sqrt{1-\beta^2})^2/8 \right] \end{aligned} \tag{4.4}$$

where $\beta = v/c$ with v being the speed of the electron and c the speed of light. N is the number of atoms per volume unit and Z is the atomic number of the stopping material (for Ge, $N = 0.44 \cdot 10^{23} cm^{-3}$ and $Z = 31$), e is the electron charge, m_0 the electron rest mass, I is an experimentally determined parameter which expresses the excitation and ionization potential of the material (for Ge, $I \approx 300 eV$).

Besides the energy loss through excitations and ionizations, the electrons are loosing energy by radiating *bremsstrahlung* due to deflections of their trajectories. The radiative specific linear loss is given by:

$$S_r = -\left(\frac{dE}{dx}\right)_r = \frac{NEZ(Z+1)e^4}{137m_0^2c^4}\left(4\ln\frac{2E}{m_0c^2} - \frac{4}{3}\right) \tag{4.5}$$

The notations are the same as for the previous equation. The radiative losses of the photoelectrons of low to medium energies, amount to only a few percent of the total energy loss. Since the *bremsstrahlung* is of small energy, it will also interact photoelectrically within a small distance creating other photoelectrons.

In a semiconductor detector, the ionizations created by the energetic photoelectron gives rise to electron-hole pairs, which normally would recombine if an electric field was not existent. Due to the reverse voltage applied in a semiconductor detector, the electrons and holes ("charge carriers") separate drifting towards the electrodes. Of importance for the semiconductor detectors is the number of electron-hole pairs produced per unit of energy by the photoelectrons. The higher this number, the lower will be the statistical fluctuation of the number of charge carriers, thus providing an improved energy resolution. The parameter representing the average energy necessary to create an electron-hole pair ϵ gives a measure of the ionization efficiency. Since part of the energy of the photoelectron is wasted in producing vibrations in the crystal lattice, ϵ represents a statistical value which is larger than the semiconductor gap between the conduction and valence bands. For germanium at 77K, $\epsilon = 2.96$eV.

4.3 The drift of the charge carriers

4.3.1 Introduction. Electric field calculation.

Following a γ-ray interaction, the produced electron-hole pairs will separate and start to drift under the influence of the electrostatic field produced by the potential applied on the detector electrodes. In a simple approach one can define the mobility $\mu_{e,h}$ of the electrons e and holes h as the variable which gives the proportionality factor between the electric field and the drift velocity:

$$\mathbf{v}_{e,h}(\mathbf{r}) = \mu_{e,h}\mathbf{E}(\mathbf{r}) \tag{4.6}$$

Unfortunately, the calculation of the drift velocities is not obvious, since the electron and hole mobilities $\mu_{e,h}$ are tensorial variables for the range of temperatures and electric fields of interest. Therefore, this topic will be emphasized in the next subsection. However, to determine the drift velocities, the electrostatic field has to be first calculated. The value of the potential at any point inside a detector of defined geometry is found by solving the Poisson equation:

$$\nabla^2\Phi(r) = -\frac{\rho(r)}{\epsilon} \tag{4.7}$$

where $\rho(r) = e \cdot n$, and $\epsilon = \epsilon_0\epsilon_r$ with $\epsilon_r = 16$ for a germanium detector. n is the impurity concentration defined as the difference between the density of donors N_d and the density of acceptors N_a. For the *n-type* germanium which will be assumed in this work, the density of acceptors is negligible, so $n \cong N_d$. For most *n-type* Ge detectors the value of n varies between $0.4 \cdot 10^{10} cm^{-3}$ and $2.5 \cdot 10^{10} cm^{-3}$. Having calculated the potential map in the detector, the electrostatic field can be then found as:

$$\mathbf{E}(\mathbf{r}) = -\nabla\Phi(\mathbf{r}) \tag{4.8}$$

For simple detector geometries, the electric field can be calculated analytically, but for more complex, non-symmetric geometries, with various border conditions, finite element or finite differences methods have to be applied. For a simple, true coaxial detector the analytical formula for a cylindrical capacitor can be used [18]:

$$E(r) = \frac{\rho r}{2\epsilon} - \frac{V + \rho\frac{r_2^2 - r_1^2}{4\epsilon}}{r\ln(r_2/r_1)} \tag{4.9}$$

where V is the applied reverse voltage, r_1 and r_2 are the inner and outer radii, ρ is the space charge density inside the capacitor, and ϵ is the dielectric constant of the material.

4.3.2 Study of the anisotropy of the electron drift velocity

Background knowledge

Germanium has the same crystalline structure as silicon and diamond, namely a face-centered cubic (FCC) structure, in which each atom lies at the center of a regular tetrahedron, and is surrounded at its apices by four atoms. The band structure of Ge has been investigated both theoretically and experimentally [19, 20, 21, 22]. These studies have established that the absolute minima of the conduction band in Ge lie along the $\langle 111\rangle$ directions, and that the minimum isoenergetic surfaces in k-space have an ellipsoidal shape ("ellipsoidal valleys"). Therefore there are four equivalent ellipsoids along the corresponding $\langle 111\rangle$ directions. Other local minima in the conduction band are found along the six equivalent $\langle 100\rangle$ directions ("ellipsoidal valleys"), and a spherically shaped band resides at the center of the Brillouin zone. These upper valleys can be populated by electrons only in very high electric fields, so it is not important to include them in calculations involving Ge detectors. In the following discussion, only the $\langle 111\rangle$ ellipsoids are considered in the simulations of electron transport. The valence band structure of Ge is similar to that of all covalent semiconductors, being formed by three bands around the center of the Brillouin zone [23, 24]. The most important band for hole transport is the heavy hole band, which has a warped parabolic shape (the term "heavy hole band" denotes the band with the highest effective mass).

In the present work the study of the electron transport properties is emphasized. The ellipsoidal parameters of the valleys are the effective electron masses:

$$\epsilon(k) = \frac{\hbar^2}{2}\left(\frac{k_x^2 + k_y^2}{m_{\|}} + \frac{k_z^2}{m_{\perp}}\right) \tag{4.10}$$

where $m_{\|}$ and $m_{\perp}$ are the effective masses. The "**kp**" method was used for the calculation of these effective masses [19, 20, 21].Experimentally, the effective masses were determined in cyclotron resonance experiments [20] and through galvanomagnetic effects [22]. Accepted values for the ellipsoidal effective masses in Ge are $m_{||} = 1.64m_0$ and $m_{\perp} = 0.0819m_0$, with m_0 denoting the free electron mass.

Due to the band structure of germanium crystals, similar to any cubic semiconductor, the electric conductivity at high electric fields and low temperatures is anisotropic. As a consequence of this anisotropy, the drift velocity of the charge carriers has different values for different orientations of the applied electric field with respect to the crystallographic axes. In addition, the drift velocity vector will have a nonzero angle ϕ with respect to the applied electric field, if the electric field does not lie along a rotational symmetry axis. The first calculations on the anisotropy in n-type Ge were carried out by Shibuya [25]. Further development of the theoretical model, taking into account intervalley scattering and carrier repopulation in different valleys was reported by Reik and Risken [26]. Nathan [27] presented a method for estimating the electron drift velocities for any value of the applied electric field, using a phenomenological approach. The introduction of Monte-Carlo methods for carrier transportation calculations in semiconductors has improved the quality of the calculated values, resulting in a good quantitative agreement with the experimental data. Jacoboni and Reggiani have published a comprehensive paper on this subject [28]. Experimental values for the angle between the drift velocity and the applied electric field have been presented by Sasaki et al. [29, 30], and the results were confirmed in subsequent work [31]. The dependence of the drift velocity on the applied electric field, for different temperatures and for particular directions ($\langle 111\rangle$, $\langle 100\rangle$ and $\langle 110\rangle$) were the subjects of detailed measurements by the Modena group [32, 34, 35, 36], using a "time of flight" method [37].

Method for simulation of the electron drift velocity

Since the drift velocity of the electrons does not have a simple analytical form as function of the electric field and temperature, we have followed a phenomenological approach [27] to calculate this dependence, using experimental data for the electron drift velocity along the $\langle 100\rangle$ and $\langle 111\rangle$ directions [32] at a temperature of 78 K and expressions for the drift velocity due to Reik and Risken [26]. In the present work, the dependence of the electron drift velocity on the applied electric field is taken to be [33]:

$$\mathbf{v}_\mathrm{d} = \mathcal{A}(|\mathbf{E}|)\sum_j \frac{n_j}{n}\frac{\gamma_j \mathbf{E}_0}{(\mathbf{E}_0\gamma_j\mathbf{E}_0)^{1/2}} \tag{4.11}$$

where γ_j is the effective mass tensor for the j-th valley, n_j/n is the fraction of the carriers in the j-th valley, $\mathcal{A}$ is a function of the magnitude of the electric field and temperature, and $\mathbf{E}_0$ is the normalized electric field vector. The values $m_l = 1.64$ and $m_t = 0.0819$ were used in the effective mass matrix γ_0,

$$\gamma_0 = \begin{pmatrix} m_t & 0 & 0 \\ 0 & m_l & 0 \\ 0 & 0 & m_t \end{pmatrix}.$$

The effective tensor in the j-th valley is $\gamma_j = \mathcal{R}_j^{-1}\gamma_0\mathcal{R}_j$ where the rotation matrix is: $\mathcal{R}_j = \mathcal{R}_{x'}(\beta)\mathcal{R}_z(\alpha_j)$, with $\beta = acos(\sqrt{2/3})$ and $\alpha_j = j\pi/4$.

The dynamics of the electrons is influenced not only by the band structure, but also by interactions with optical and acoustical phonons, impurities and other charge carriers which exist in the crystal lattice. These interactions may result in the scattering of charge carriers from one band to another, which is referred to as "interband" scattering ("intervalley" for electrons). If the carriers are scattered within the same band, the scattering is "intraband" ("intravalley"). Intervalley scattering is very important since it can repopulate valleys that have different orientations with respect to the electric field.

The general expression for the dependence of repopulation of the j-th valley on the orientation of the applied electric field is given by the following formula [26] (l is a index of the valleys, the corresponding sum being over all valleys):

$$\frac{n_j}{n} = \frac{(\mathbf{E}_0\gamma_j\mathbf{E}_0)^{-1/2}}{\sum_l(\mathbf{E}_0\gamma_l\mathbf{E}_0)^{-1/2}} \tag{4.12}$$

In the original paper of Reik and Risken, a relation for the repopulation was obtained which is independent of temperature and field strengths. In their calculations they assumed that the intervalley scattering has no influence on the Maxwellian energy distribution of the electrons, but only on the population distribution between valleys, and that the energy loss induced by interactions is given only by the optical intravalley scattering. Furthermore, approximate relations for the electron temperature were used. In this approach, eq. (4.12) represents a limiting case in which the repopulation does not depend on the norm of the electric field, but only on its orientation. In fact, the repopulation ratio n_j/n varies due to different carrier scattering processes on phonons for different lattice and charge carrier temperatures. In the present phenomenological approach it is not necessary to know the complex dependence of the conduction band population on the scattering mechanisms, since it is estimated from experimental data on the drift velocity at a fixed temperature. For an experimental determination of the repopulation amplitude, the deviation from a uniform population distribution n_e/n (1/4 for germanium) is assumed to vary with the electric field weighted by the factor $\mathcal{R}$:

$$\frac{n_j}{n} = \mathcal{R}(|\mathbf{E}|)\left[\frac{(\mathbf{E}_0\gamma_j\mathbf{E}_0)^{-1/2}}{\sum_l(\mathbf{E}_0\gamma_l\mathbf{E}_0)^{-1/2}} - \frac{n_e}{n}\right] + \frac{n_e}{n} \tag{4.13}$$

If the electric field vector is equally oriented with respect to all the $\langle 111 \rangle$ directions, there is an uniform repopulation of the conduction bands. An electric field applied along the $\langle 100 \rangle$ direction, which satisfys this condition, assures that $n_j/n = 1/4$ at any electric field strength. By employing the experimental drift velocity for an applied electric field in the $\langle 100\rangle$ direction at a specific temperature, the value of the parameter $\mathcal{A}$ can be determined using Eq. (4.11) for various values of the electric field. Furthermore, using Eq. (4.13) for n_j/n in the drift velocity formula (4.11), the parameter $\mathcal{R}$ can be calculated employing the experimental drift velocity along the $\langle 111\rangle$ direction. After determination of the parameters $\mathcal{A}$ and $\mathcal{R}$, the drift velocity can be calculated for any direction and any strength of the electric field.

The dependence of the experimental $\langle 111\rangle$ and $\langle 100\rangle$ drift velocities on the electric field can be fitted with the empirical formula [38]:

$$v_{exp} = \frac{\mu_0 E}{\left(1+\left(\frac{E}{E_0}\right)^{\beta}\right)^{1/\beta}} - \mu_n E. \tag{4.14}$$

This formula differs from that given in [38], in the last term which was added to fit the negative differential mobility of the electrons at very high electric fields. The fitted parameters values are presented in Table 3.

Table 3 Fit parameters for the experimental drift velocities in the $\langle 100\rangle$ and $\langle 111\rangle$ directions

Direction	μ_0 $\left[\frac{cm^2}{Vs}\right]$	E_0 $\left[\frac{V}{cm}\right]$	β	μ_n $\left[\frac{cm^2}{Vs}\right]$
$\langle 100\rangle$	40180	493	0.72	589
$\langle 111\rangle$	42420	251	0.87	62

Simulation results

The dependence of the experimental drift velocity in a Ge crystal on the applied electric field for the $\langle 100\rangle$ and $\langle 111\rangle$ directions [32], together with the calculated drift velocities for the $\langle 110\rangle$ direction, are shown in fig. 2.

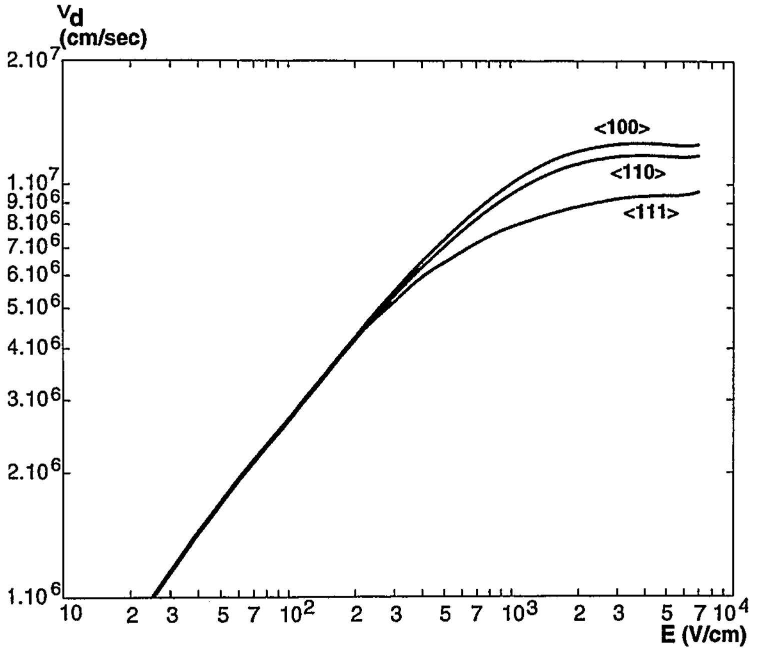

Figure 2 The experimental drift velocities of electrons in a Ge crystal along the ⟨111⟩ and ⟨100⟩ directions at a temperature of T=78K (from [32]) and the simulated drift velocity for a field oriented along the ⟨110⟩ direction.

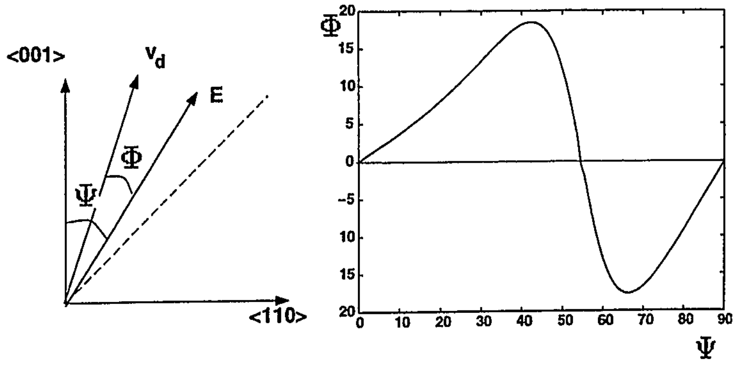

Figure 3 The simulated angular shift between the drift velocity and the applied electric field in the {110} plane. An electric field of E=2000Vcm^{-1} and a temperature of T=78K was assumed.

The simulated dependence of the drift velocity on electric fields oriented along the $\langle 110 \rangle$ direction agrees qualitatively with the behavior measured by Neukermans and Kino [37]. Unfortunately, a quantitative comparison cannot be made since the drift velocities in [37] are systematically smaller than those of [32], suggesting a higher impurity concentration in the crystal investigated in [37]. The simulated angular shift between the drift velocity and the applied electric field in the $\{110\}$ plane agrees with the experimental values of Sasaki et al. [30]. In fig. 3 the angular shift is shown for an electric field of 2000V/cm; here Ψ is the angle between the electric field vector and the crystallographic direction $\langle 100 \rangle$, and Φ is the angle between the drift velocity and the electric field vector.

4.4 Formation of detector signals

4.4.1 Induction of signals in the detector electrodes

A signal is induced on the sensing electrodes of a detector by the cumulative influence of electrons and holes moving toward the electrodes. To determine the electric current induced by a moving charge in an electrode, the Green's "reciprocity theorem" is used. Accordingly, the induced current $I(t)$ is determined by the charge amplitude Q_0, the *weighting field* $\mathbf{E}_\mathrm{w}(\mathbf{r})$ and the charge drift velocity $\mathbf{v} = d\mathbf{r}/dt$ [39, 40]:

$$I(t) = Q_0 \mathbf{E}_\mathrm{w}(\mathbf{r}) \frac{d\mathbf{r}}{dt} \tag{4.15}$$

The weighting field $\mathbf{E}_\mathrm{w}$ of an electrode is defined as the electric field calculated by solving the Poisson equation 4.7, taking a potential of 1 Volt on the considered electrode and zero on all the other detector electrodes [40]. In the case of a cylindrical detector, the relation 4.9 can be used for the charge induced in either external

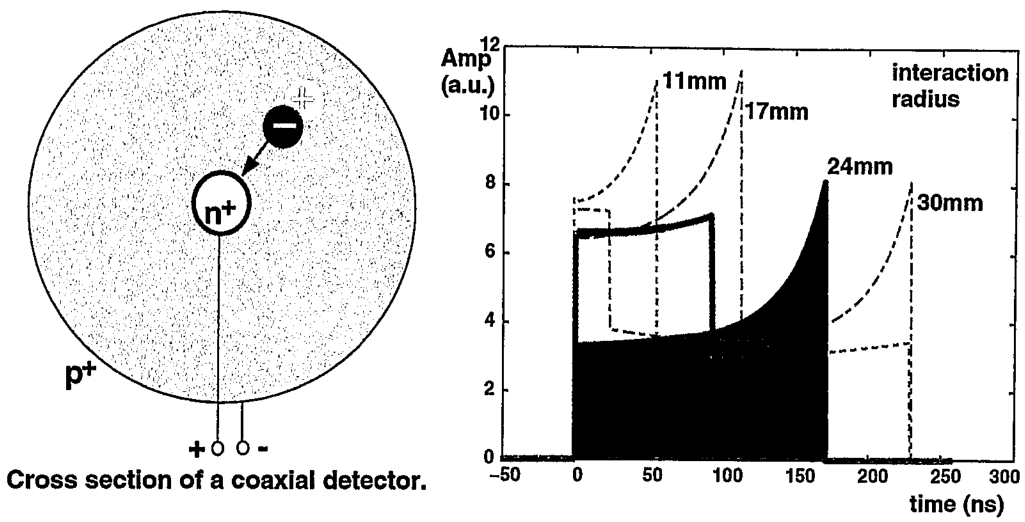

Cross section of a coaxial detector.

Figure 4 Left: transversal section through an n-type coaxial detector showing the drift directions of the charge carriers. Right: induced current signals in the detector corresponding to four interaction radii.

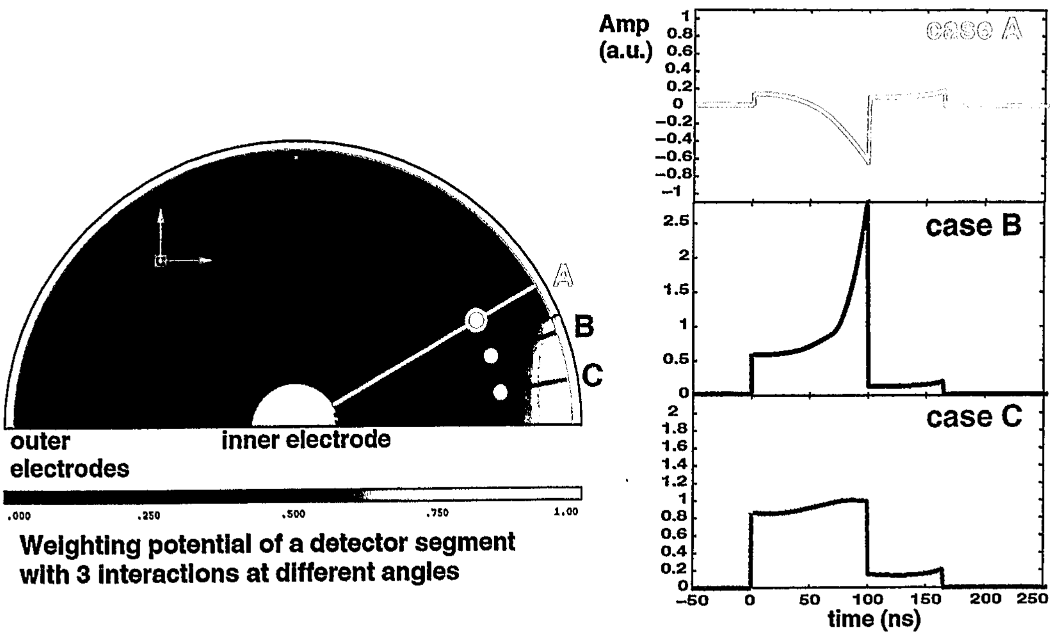

Weighting potential of a detector segment with 3 interactions at different angles

Figure 5 Weighting potential of a segment in a coaxial detector with three examples of interactions occurring at the same radius but at different azimuthal angles (left), and the corresponding induced current signals (right).

or internal electrode, but with the note that the spatial charge density ρ should be assumed zero here, since this field should exclusively represent the capacitive coupling between the electrode and the moving charge. Examples of induced currents in a coaxial detector are presented in fig. 4. In the left part of the figure, a transversal cut through a coaxial detector is presented together with the drift directions of the charge carriers. Depending on the radius where the charge carriers are produced, they will have different drift distances to the detector electrodes. Accordingly, the shapes of the induced currents will be different for different interaction radii. The right part of the figure 4 depicts 4 such examples. For a segmented detector however, the induced currents will give either a net charge deposited in the segment or a zero charge, depending on whether the carriers are collected in the segment or not. The left side of figure 4 pictures the weighting fields of a segment in a coaxial detector and three cases of interactions occurring at the same radius but at different azimuthal angles. The corresponding current signals in the segment are shown on the right side.

4.4.2 Detector and preamplifier noise

The noise in the detection systems generally originates from randomly generated impulses which have a Poisson distribution in time. The main sources of noise in a Ge detector system are the detector itself and the field effect transistor (FET) of the preamplifier [39, 42]. At the detector level, the thermally generated charge carriers give rise to what is called "leakage current". The statistical variation in time of these charge carriers is of concern for the noise problem. The noise produced in the detector can be represented as a current source with an equivalent resistance R_P in parallel with the preamplifier input. However, since the detector is operated at cryogenic temperatures, the most significant noise in the experimental signal is produced by the FET [41], by thermal fluctuations of the conducting channel modified by the effect of channel width modulation. The corresponding potential fluctuations are equivalent to the one produced by the thermal noise in an equivalent resistance R_S in series with the preamplifier input.

4.4.3 Preamplifier shaping

The aim of the preamplifier is to amplify the detector charge signal, making it suitable for further amplification with analog electronics, or for sampling with an *Analog-to-Digital Converter* (ADC). Typically, the first stage of the preamplifier is a charge sensitive operational amplifier, with a capacitive feed-back. In the amplification process, a shaping of the input signal is unavoidable, the frequency band of the input signals being limited by the preamplifier bandwidth. This can be represented in the time-domain by a convolution of the detector signal $I(t)$ with the preamplifier impulse response function $T(t)$:

$$S(t) = \int I(t')T(t-t')\,dt' \tag{4.16}$$

where $S(t)$ is the preamplified signal.

For many preamplifiers, the impulse response function can be approximated by:

$$T(t) = \begin{cases} \frac{A}{T_d - T_r \frac{\sqrt{\pi}}{2\sqrt{1.3}}} \left[\exp\left(-\frac{t}{T_d}\right) - \exp\left(-\frac{1.3t^2}{T_r^2}\right)\right] & \text{for } t > 0 \\ 0 & \text{otherwise} \end{cases} \tag{4.17}$$

Here, T_r and T_d are the rise and decay times, respectively, and A is the amplification factor. In the simulation, values of $T_r = 45ns$ and $T_d = 50\mu s$ were used, which were appropriate for the preamplifier employed in our experiments. For the subsequent applications of pulse shape analysis methods, the knowledge of the preamplifier shaping is necessary, since it produces an important bandwidth limitation of the signals.

4.5 The influence of the drift velocity on the signal shapes

4.5.1 Realistic simulation of pulse shapes

Using the presented method to calculate the drift velocities, the next requirement for the simulation of detector pulse shapes is to determine the map of the electric field between the electrodes. For a complex detector geometry, like it is the closed-end detector, the electric field values are obtained by solving the Poisson's equation numerically, using discrete Maxwell's equations. The software package MAFIA was used for this purpose [17]. For a true coaxial detector, the analytical formula 4.9 is used. To simulate the charge carrier trajectories, an initial point $\mathbf{r_0}$ is taken to be the position where the γ-ray interacted within the detector volume. The electric field vector at this position is then used to find the drift velocity vector. The next point on the carrier trajectory is approximated by $\mathbf{r_1} = \mathbf{r_0} + \mathbf{v_d}(\mathbf{r_0}) \cdot \delta t$, where δt is a time interval which was chosen to be small enough so that the drift velocity could be considered as a constant vector. The calculation of the next steps on the trajectory is continued until the carriers reach the detector contacts, which terminates the trajectory. Finally, the pulse shape is calculated using the expression 4.15 for the current induced at the electrode of a detector characterized by the weighting field E_w for a charge Q_0.

A note needs to be made regarding the induced current at the electrodes of a segmented detector. In this case the anisotropy will not only affect the signal shapes of the segments in which the charges are collected, but it will also modify the induced signal shapes of the neighbouring segments. The different trajectories of the electrons, which depend on the different crystallographic orientations with respect to the segmentation lines, will produce different induced currents in the non-irradiated segment, since the paths of the carriers pass through different weighting fields.

The influence of the charge-sensitive preamplifier was taken into account by convolving the detector signal with the impulse response of the preamplifier.

Since a realistic attempt of pulse shape analysis requires the use of digital signal processing, an antialiasing filter has to be included between the preamplifier and the sampling ADC to limit the bandwidth of the signal according to the sampling frequency and to filter the pick-up noise (see sections 5.3 and 5.4 for a more extensive presentation of this subject). This filter is approximated by averaging the simulated preamplifier signal over a window of 30ns. The influence of trapping centers in the detector was not considered since this effect varies among the individual detectors, due to the radiation damage history. However, this influence is negligible for a good Ge detector.

Simulation of electron trajectories

For absorption of γ-quanta close to the surface of the detector, mainly the drift of electrons towards the inner electrode contributes to the detector signal, whereas the holes reach the external electrode shortly after the interaction. This situation is taken into account in the pulse shape simulations, since the present method for the calculation of the drift velocity applies only to electrons. In the calculation of the electric field a cylindrical, closed-end design was assumed, with a charge density of $0.4 \cdot 10^{-9} C/cm^3$. The trajectories of the electrons produced by photoelectric interactions close to the surface of the rear, coaxial part of the detector, as well as of those produced by interactions in the front part at a detector radius of 20 mm, are shown in fig. 6. In the front view, an azimuthal bending of the trajectories can be seen. One can observe a larger bending effect for the front region case.

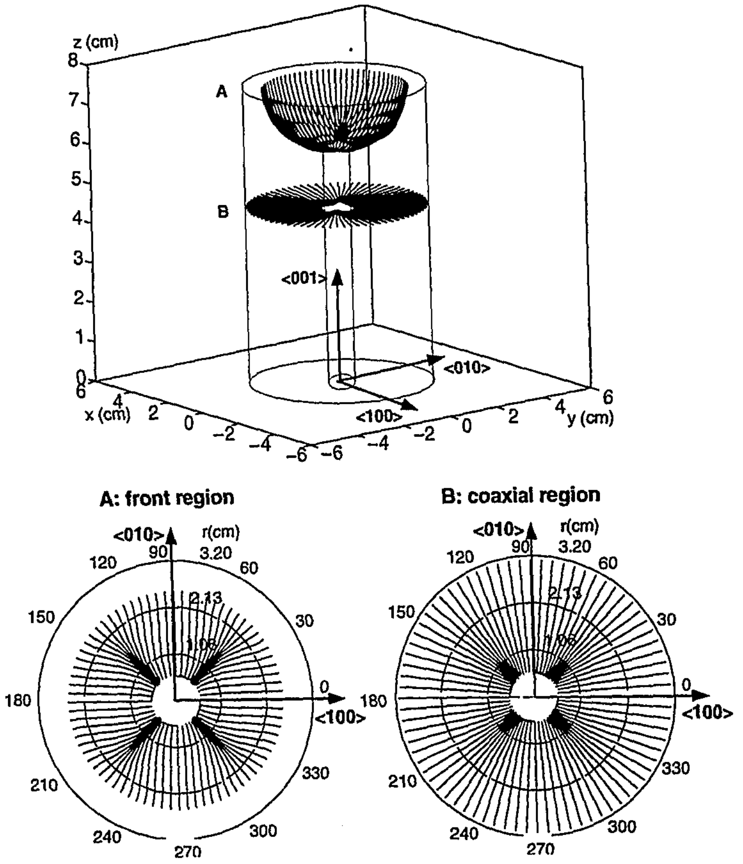

Figure 6 Simulated charge carrier trajectories in a closed-end HPGe detector, from interactions of γ-quanta in the front part (**A**) and in coaxial part (**B**) of the Ge detector. The upper drawing shows a spatial representation, and the lower drawings show front views.

Examples of simulated pulse shapes

Information on the charge carrier transport in the detector is contained in the current signal. Since only the charge signal integrated by the preamplifier can be measured experimentally, for the purpose of pulse shape analysis, the preamplifier signal needs to be differentiated. In what follows, the term "pulse shape" will refer to the differentiated signal of the preamplifier. The simulated pulse shapes in a closed-

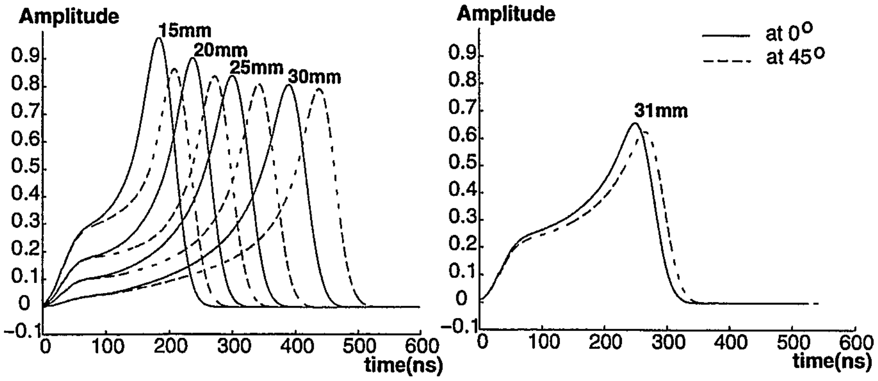

Figure 7 Several simulated pulses are shown. Left, interactions in the front part of the detector at various radii; right, interactions in the coaxial region at a radius of 31 mm. Pulse shapes for azimuthal angles of 0° and 45° with respect to the $\langle 100 \rangle$ direction are shown.

end detector with interactions at the detector surface are shown in fig. 7, for a range of interaction radii and azimuthal angles.

4.5.2 Experimental results

Measurements of pulse shapes were made using an encapsulated, semihexagonal, n-type HPGe detector from the EUROBALL project [1] (Figure 8). The detector is of closed-end type, operated with a reverse bias of $4500V$, and has a height of $76mm$, a radius of $35mm$ at the rear end, and a central hole of $5mm$ diameter and $61mm$ length. The impurity concentration is estimated to be $\approx 1.5 \cdot 10^{-9} C/cm^3$ at the rear end of the detector, decreasing to $\approx 0.4 \cdot 10^{-9} C/cm^3$ at the front.

For pulse shape measurements, γ-ray sources of ^{22}Na and ^{241}Am were used.

Measurement of the Ge crystal orientation

The orientation of the Ge crystal was determined by means of neutron scattering measurements using the neutron reflectometer HADAS which is installed at the FRJ-2 Research Reactor DIDO of the Forschungszentrum Jülich.

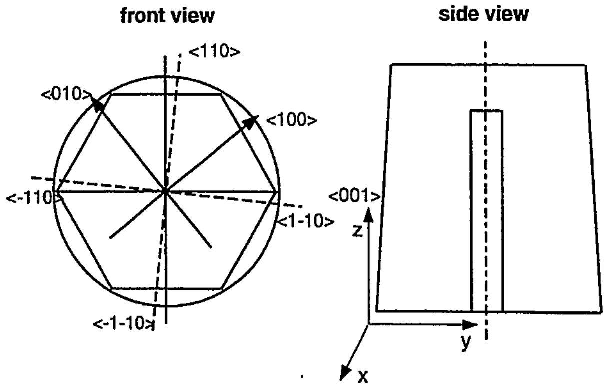

Figure 8 Geometry of the semihexagonal closed-end Ge detector and its crystal orientation. The detector has a hexagonal front side and a circular rear side.

Since the distance between the corner atoms of Ge is $a = (5.6575 \pm 0.0001)$Å, the neutron wavelength was set to $\lambda = 2.828$Å, corresponding to reflections of the (220) Bragg planes for an angle of $\theta = 90°$ between the neutron beamline and neutron detector. In the orientation measurement we found that the $\langle 110 \rangle$ crystallographic axis has an angle of $(4.5 \pm 0.2)°$ with respect to the median of the hexagonal detector geometry, as shown in fig. 8. The $\langle 001 \rangle$ direction was found to be almost parallel to the symmetry axis of the detector, the deviation being only $(1.7 \pm 0.1)°$.

Pulse shape measurements with a ^{22}Na source

For a ^{22}Na source, the pulse shapes of the 511 keV positron annihilation quanta were determined. A NaI(Tl) scintillator was placed opposite to the Ge detector (see fig. 9). The γ-radiation from the ^{22}Na source was collimated with lead collimators in both directions (towards the Ge detector with a hole of $1.5mm$), in order to irradiate the Ge detector within a well defined solid angle and to minimize chance coincidences.

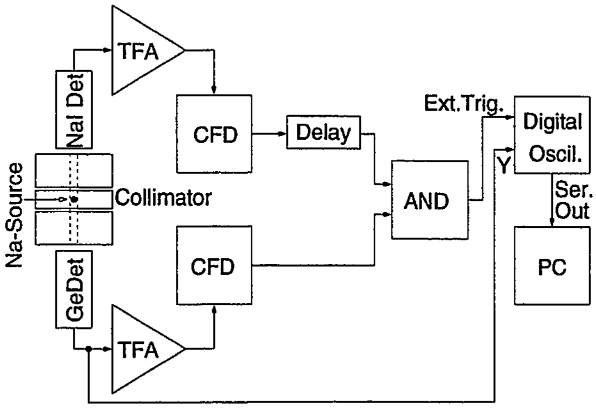

Figure 9 The coincidence circuit used in measurements with the ^{22}Na source.

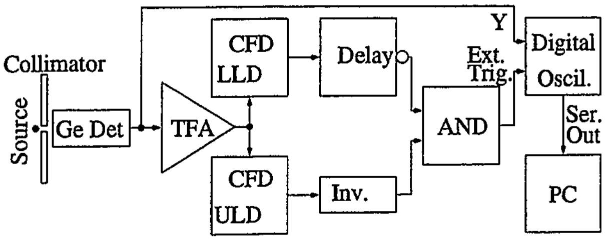

Figure 10 The acquisition system used in measurements with an ^{241}Am source.

The preamplifier pulse shapes were recorded using a digital oscilloscope with a sampling rate of up to 1 Gs/sec and 8 bit resolution. An external trigger signal for the oscilloscope was obtained by requiring a coincidence between the NaI(Tl) scintillator and the Ge detector. The coincidence circuit is shown in fig. 9. The trigger time reference of the recorded pulses was defined by the constant-fraction discriminator of the scintillator. For a given radius, the front face of the Ge detector was scanned in steps of 15° around the detector symmetry axis, and pulse shapes were recorded.

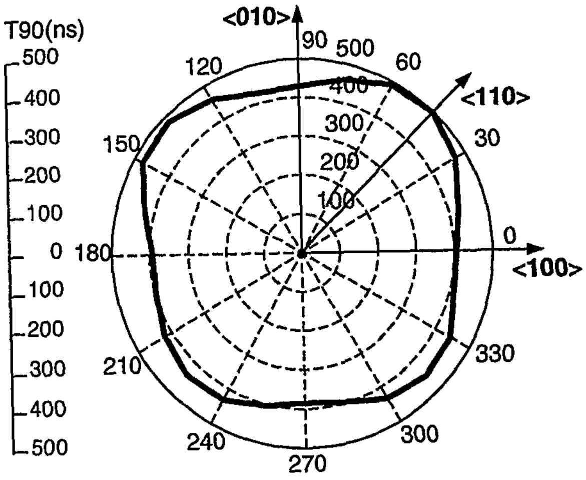

Figure 11 Polar plot of the centroids of the T90 spectra for 511 keV γ-rays from a ^{22}Na source irradiating the Ge detector at different azimuthal angles, at a radius of 25mm.

A separate measurement of a spectrum of the time elapsed between the beginning of the pulse and the time corresponding to 90% of the preamplifier charge amplitude (T90) was performed using the ^{22}Na source. The T90 time characterizes the signal shape, since it indicates how quickly charges are collected at the electrodes. With a start signal given by the constant-fraction discriminator of the scintillator, and a stop signal given by a leading-edge timing discriminator of the Ge detector with a threshold set at 90% of the 511keV signal amplitude, a T90 spectrum was acquired using a time-to-amplitude converter, followed by an ADC and a multichannel analyzer. A polar plot of the centroids of the T90 spectra versus angle at a radius of 25 mm is shown in figure 11. It is evident that the T90 values have an angular dependence which is correlated to the crystallographic directions of the detector. The largest values correspond to the $\langle 110 \rangle$ crystallographic direction, while the smallest

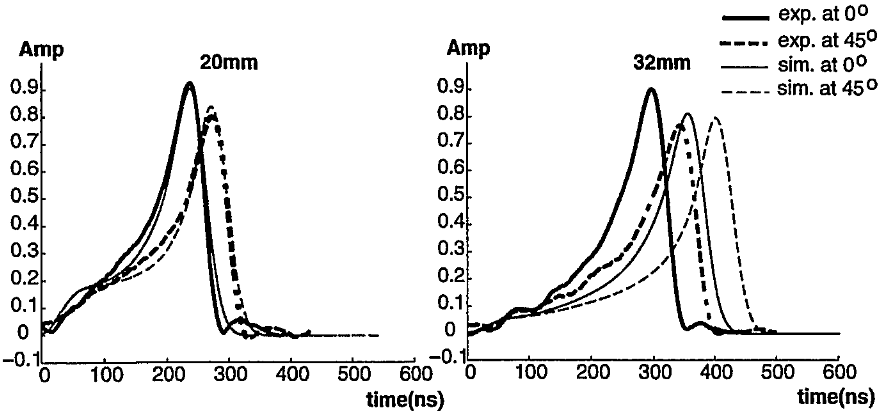

Figure 12 Examples of experimental signal shapes obtained from interactions in the front part of the detector at azimuthal angles of 0° and 45° with respect to the $\langle 100 \rangle$ direction, for 60 keV γ-rays from an ^{241}Am source. The thin lines indicate the corresponding simulated shapes. Left, interactions at a radius of 20 mm; right, interactions at a radius of 32 mm.

ones correspond to $\langle 100 \rangle$. The deviation from 90° symmetry results from a non-centered skew mounting of the detector.

Pulse shape measurements with an ^{241}Am source

An ^{241}Am source emitting γ-rays of 60 keV was used to investigate the detector response to interactions close to the surface of the detector. The γ-radiation was collimated using a lead collimator, which allowed the irradiation of an area of approx. 1 mm^2. The detector was irradiated on the front face as well as from the side in the coaxial region every 15° around the symmetry axis. The pulse shapes were recorded using the digital oscilloscope described above, however an average over 128 pulses was carried out to give a better signal-to-noise ration. The acquisition system used is shown in fig. 10.

Typical pulse shapes obtained with the ^{241}Am source are shown in figs. 12 and 13. The most important observation is that the difference between the pulse

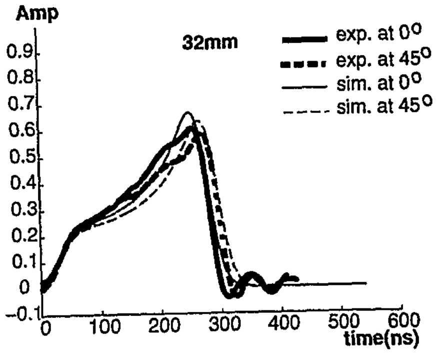

Figure 13 Examples of experimental signal shapes obtained from interactions in the coaxial part of the detector at azimuthal angles of 0° and 45° with respect to the ⟨100⟩ direction, for 60 keV γ-rays from an ^{241}Am source. The thin lines indicate the corresponding simulated shapes.

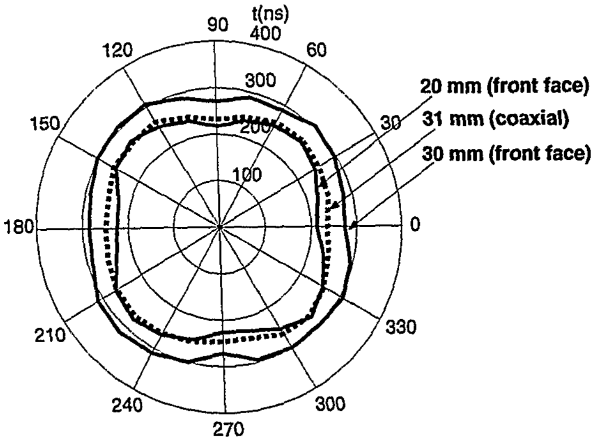

Figure 14 Polar plot of the average time-to-maximum for pulses from 60 keV ^{241}Am γ-rays.

shapes measured at positions with angles differing by 45° is larger if the detector is irradiated from the front than irradiated on the side. This observation is in qualitative agreement with the results of the simulation. In the following, we use a *time-to-maximum* parameter to represent the pulse lengths. This is defined as the interval between the beginning of the pulse and the time when the pulse shape (the differentiated charge signal) reaches its maximum value. Experimentally, we observed a difference between the *time-to-maximum* values obtained at positions differing by 45° which varied almost linearly with the radius, increasing from $0ns$ at $5mm$ to $50ns$ at $32mm$, for frontal irradiation of the detector. In comparison, the difference is $14ns$ for side irradiation. These differences are consistent with our simulations, but the calculated time-to-maximum values for all azimuthal angles are bigger, especially at large radii. The deviation between the calculated and measured values may be due to the fact that the electric field used in the simulations was calculated for a cylindrical detector, whereas a semihexagonal EUROBALL detector was used in our experiments. If so, the largest deviations are expected at the edges of the detector front face. A more detailed program for the electric field estimate is required to treat the actual geometry of the EUROBALL detector. The time-to-maximum values measured over the whole 360° range for different radial positions are shown in fig. 14.

4.5.3 Comments

Experimental evidence for the dependence of pulse shapes in closed end HPGe detectors on the electron drift velocity anisotropy, and hence on the crystallographic orientation, has been established for the first time. The simulated pulse shapes agree rather well with experiment. Some differences between the simulations and measurements are still evident, and are mainly due to the assumption of the electric field of a cylindrical detector rather than the electric field of the semihexagonal Ge detector used in the measurements. Similar effects on the induced currents are expected from the anisotropy of the hole drift velocity.

The presented method for the calculation of charge carrier trajectories in three dimensions should prove to be useful in simulating realistic pulse shapes for Ge detectors of various geometries. In this approach, the effect of the drift velocity anisotropy can be accurately estimated in the development process of Ge detectors and in pulse shape analysis for position determination. The principal conclusion is that the drift velocity anisotropy should be included in order to obtain reliable results for the position at which the γ-quantum interacts with the Ge detector. Neglecting this effect, the spatial resolution attainable with Ge detectors would be severely limited, especially in a closed-end geometry. In the case of segmented detectors, the anisotropy will affect not only the pulse shapes in the segments at which the charge is collected, but also those of the induced charges in the neighbouring segments.

CHAPTER 5

PULSE SHAPE ANALYSIS FOR POSITION SENSITIVITY

5.1 Introduction

The coarse position sensitivity of a semiconductor detector is given by its volume. Usually, detection with position sensitivity better then the physical volume is achieved by making a segmentation of the detection unit, either by segmenting one of the read-out electrodes, or by segmenting both electrodes, and combining the information from the two channels. Examples for the first case are planar pixel detectors whereas for the second case are the strip detectors. These are imaging detectors with broad applications in high energy physics, medicine and other imaging applications. The use of high-resolution Ge detectors for γ-ray position determination has important particularities, since there are strong limitations on the segmentation level which can be made. In this context, the solution for an optimum position sensitivity is to use a medium segmentation scheme of the detector, and to achieve a superior position resolution by digitally analyzing the pulse shapes of the detector segment signals.

In section 5.2 the segmented Ge detector used in simulations will be presented, and the arguments for the chosen design will be given. Section 5.3 will emphasize the main features a digital signal processing system has to have for analyzing detector pulse shapes, along with the presentation of the PPADC, the digital device currently used for on-line implementation of the developed algorithms. In order to be able to use the experimental data for analysis, a set of procedures are necessary for conditioning the raw detector signals. The developed digital algorithms for signal triggering and timing are presented in section 5.4. The results of the on-line implementation of the algorithms will be also featured. A larger section (section 5.5) will be assigned to the wavelet transform which is used for preprocessing the data. The preprocessing is intended to make the data suitable for feeding into a pattern recognition system able to identify the positions of the interactions within the detector. Section 5.6 study two examples of such systems for identification of the interactions.

5.2 Design of segmented Ge detectors

5.2.1 *The development status of segmented Ge detectors*

A number of segmented Ge detectors were already developed, either intended for the reduction of Doppler broadening for in-beam experiments, or directly aimed for testing various γ-ray tracking concepts. One of the first important stable detector was the *MINIBALL* detector developed by a collaboration among the University of Köln, Eurisys Mesures, MPI-K Heidelberg and Forschungszentrum Jülich [43]. This detector is based on the general design of the EUROBALL detector, which is a coaxial detector having a semi-hexagonal geometry (hexagonal at the front face and cylindrical at the rear side), being contained in a vacuum tight capsule, and which has an azimuthal 6-fold segmentation. The segmentation for this detector was designed especially for Doppler broadening correction [44].

Various detector prototypes were developed for γ-ray tracking concepts. To this category belongs the cylindrical 25-fold segmented Ge detector designed by INFN, Sezione di Padova, and developed by Eurisys Mesures. This detector is of closed-end cylindrical type, having 6 azimuthal segmentations and 4 longitudinal ones, plus an extra circular segment on the front face [45]. The detector electrodes are read-out through 26 cooled field-effect transistors (FET), giving on average an energy resolution of 2.1 keV for the segments. Another tracking detector has been developed by the Lawrence Berkeley National Laboratories (LBNL) with Eurisys Mesures [46]. This is an 36 fold segmented closed-end Ge detector, having a tapered hexagonal shape. The segmentation scheme is given by 6 azimuthal times 6 longitudinal segmentations. The detector electrodes are read-out through 37 cooled FET, with an average energy resolution of 2.15 keV for the segments [47].

Other prototypes are currently under development at the companies Eurisys Mesures and Ortec. In principle, the main technologies for the development of segmented HPGe detectors are well established. Nevertheless, further improvements are required regarding passivation techniques, implantation of electrodes, coating or encapsulation of the detector, in order to improve the reliability of the segmented Ge detectors.

5.2.2 Characteristics of an improved design

General features

It has been demonstrated in section 3.3 that, with present days technology, only a high-purity Ge detector, in particular the n-type detectors, can fulfill the requirements for high resolution spectroscopy of γ-rays. Yet, the use of HPGe detectors poses a few restraints on the design, which will be discussed subsequently.

Besides high energy resolution, a γ-ray tracking detector should have additional important features, namely a high photopeak efficiency and good position sensitivity. As for the detection efficiency, once having selected the detector material, this can be increased by increasing the volume of the detector. On the other hand, a full depletion of the detector at reasonable bias voltages puts an upper limit on the thickness of a detector. This limit depends The attainable depletion depth depends on the impurity concentration, on the high voltage which can be applied but also on the detector geometry. It was proven a long time ago that, compared with planar or other geometries, a coaxial geometry is the best solution for this problem, because of the high electric field created towards the inner contact. Furthermore, the ratio between the area of the electrodes and the detector volume should be minimal since a large area of the electrodes will involve an increased dead volume of the detector, due to its thickness which can be relatively high, especially for the Li-drifted (n^+) contacts. At present, the thickness of the (n^+) contact gives a limitation which has to be considered in the detector design. For n-type Ge detectors the (n^+) contact lies in the central hole so that the dead material due to the contact is minimal. Nevertheless, the situation can improve if other methods will be found to create reliable thin (n+) contacts. Other advantages of a coaxial detector lies in its compactness, in the low capacitance with respect to the total volume, having consequences in the preamplifier noise level, as well as in the convenience to accommodate the thermic contact between the Ge material and the cool finger, since to obtain a high energy resolution, the detector should be cooled to liquid nitrogen (LN2) temperature.

In contrast to the efficiency, to achieve a high position resolution small detector volumes are suggested. This can be normally achieved by segmentation of the electrodes. Unfortunately, the segmentation cannot go very far, since serious technical difficulties appear in reading out the many channels from the detector cryostat, which is a low pressure, low temperature environment. An analysis of the segment pulse shapes is necessary to obtain supplementary information about the position of the interaction. But for an efficient pulse shape analysis, supplementary conditions are implied in what regards the detector design.

A closed-end detector has disadvantages, due to the stronger effect of the drift velocity anisotropy and the existence of low electric fields toward the edges of the closed-end front region of the detector. Therefore, large variations for the drift times of the carriers will exist in this region, corresponding to the different crystallographic directions. As shown in chapter 4, in the closed-end front region, the difference between the drift times can be as much as 25%. Moreover, due to the low electric fields, and larger drift distances, the overall drift time of charge carriers for the same radius and azimuthal angle, is in the closed front region 25% bigger than in the rear coaxial region of the detector. These large variations in the pulse shapes for equivalent positions of interactions implies difficulties in designing compact algorithms for pulse shape analysis. Ideally, the same analysis procedure should apply for all regions of the detector and for all segments, where for compactness, symmetries would be desirable. Therefore it is proposed to use a "true" coaxial detector design. This design is characterized by coaxial cylindrical electrodes, having two open surfaces at the bottom and the top of the cylinder. Both open surfaces have to be passivated. The segmentation scheme of such a detector is discussed in the following.

Segmentation pattern

As will be presented in section 5.7, the accurate determination of the full three-dimensional position of the interaction will involve the correlation of the induced pulse shapes of the irradiated segment with the pulse shapes of the neighboring segments in the azimuthal as well as longitudinal direction. This implies that the power of the induced signals in both directions should be maximized and made relatively comparable. This requirement correlates the segmentation geometry in one direction to the segmentation in the other direction, a certain width of the segments in one direction determining that of the other direction. Since the calculated weighting fields appear to decrease faster in the longitudinal direction (see figure 16), the height of the detector segment should be smaller than the width if the determination of the interaction depth is as important as that of the azimuthal angle. In order to have the azimuthal segmentation geometry symmetric with respect to the crystallographic

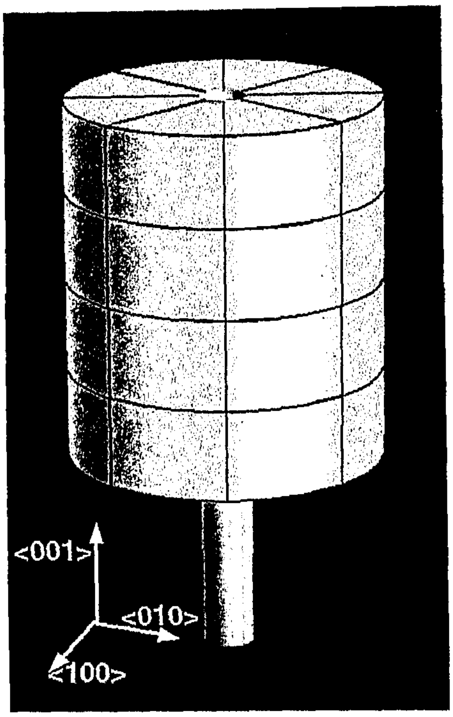

Figure 15 View of the proposed coaxial 8x4-fold segmented detector. The crystallographic axes of the Ge crystal are also depicted.

axes of Ge, a multiple of a 4-fold segmentation is required. For example, an 8-fold segmentation would give reasonably small segments. Accordingly, the ⟨001⟩ crystallographic axis should be along the detector axis, whereas the ⟨100⟩, ⟨010⟩ axes should point toward medians of the azimuthal detector segments. Having chosen an 8-fold segmentation in the azimuthal direction, for a detector of 72mm length and 32mm radius, a 4-fold longitudinal segmentation is required. Figure 15 shows the view of such a detector, together with the orientation of the Ge crystal.

The proposed detector design involves some technical challenges which have to be addressed:

1.) The passivation of the two open surfaces has to be improved;

2.) A correction of the field distortions at the open surfaces has to be made for better performances and to minimize the dead volume of the detector.

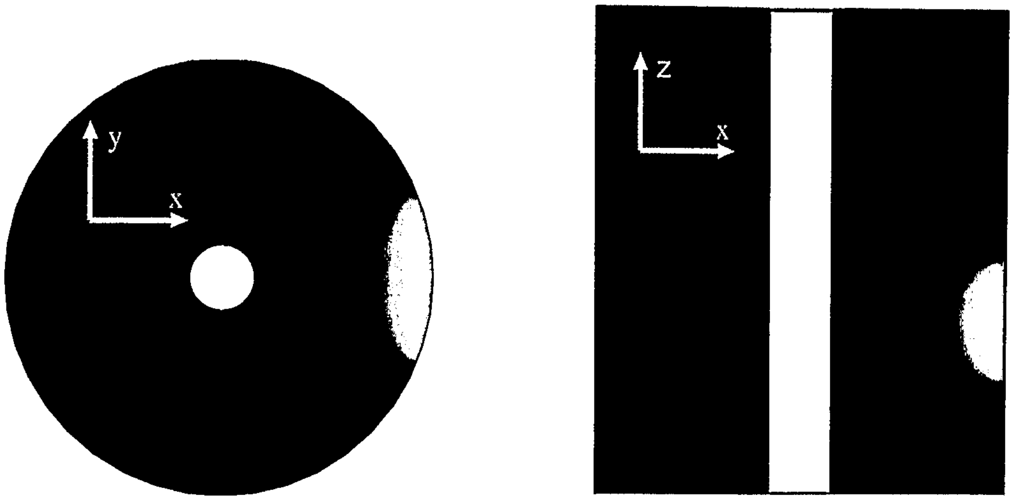

front view **side view**

Figure 16 Front and side views of the weighting potential corresponding to median sections through a segment in an 8x4-fold segmented true-coaxial Ge detector. The calculations were made using the MAFIA program [17].

It should be noted that considerations regarding a compact arrangement of the detector in an array were not taken into account. Nevertheless, for the aim of testing pulse shape analysis concepts, the simulations of section 5.7 are based exclusively on this detector design.

5.3 Electronics for digital signal processing

5.3.1 General requirements

For an efficient γ-ray tracking spectrometer, a compact array of about 100 Ge crystals which are up to 36-fold segmented is foreseen. The high dynamic range as well as the bandwidth of the preamplifiers in the range of 25MHz implies the requirement to sample the preamplifier output signal at 50 Msps/s with at least 12 bits. This gives a total number of about 3700 processing channels, each with a primary data rate of 75 Mbyte/s. Accordingly, compact digital signal processing electronics is required, able to read the sampled data and to process the signals in real time to reduce the data rate to be stored, by extracting the most essential information. A general working scheme is shown in fig. 17. In a first approximation, the digital signal processing electronics should be able to execute basic conditioning and preprocessing of the signal, like signal triggering, precise event timing, γ-ray energy determination, and to create a compact representation of the signal shapes for further analysis in the next processing levels, or for storage for off-line data analysis.

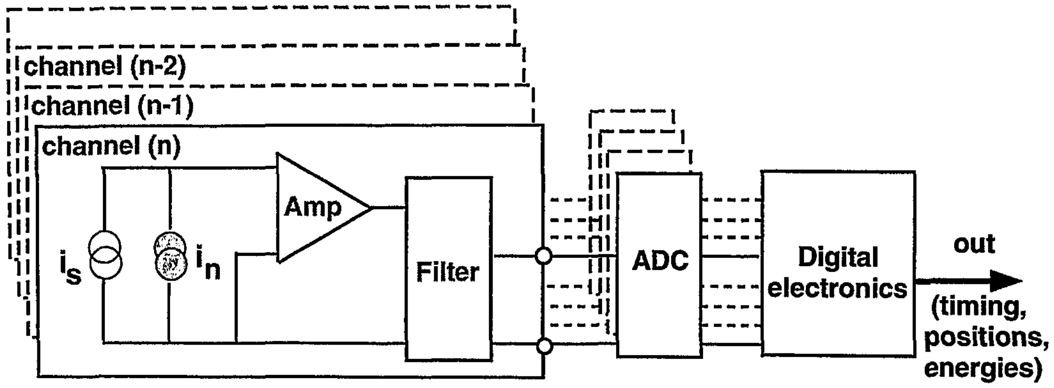

Figure 17 General scheme of electronics for acquisition and processing of the segment signals. Ideally, the digital electronics should give information about the event time, the released energy and the position coordinates in three dimensions.

5.3.2 *The Pulse Processing Analog to Digital Converter (PPADC)*

For implementation and testing of the presently developed algorithms, a new prototype of the Pulse Processing Analog to Digital Converter (PPADC) was used. The PPADC is a development of the Forschungszentrum Jülich and the manufacturer *target systemelectronic gmbh*, based on the original concept of a digital signal processing system for high resolution spectroscopy [48]. The new device is designed as part

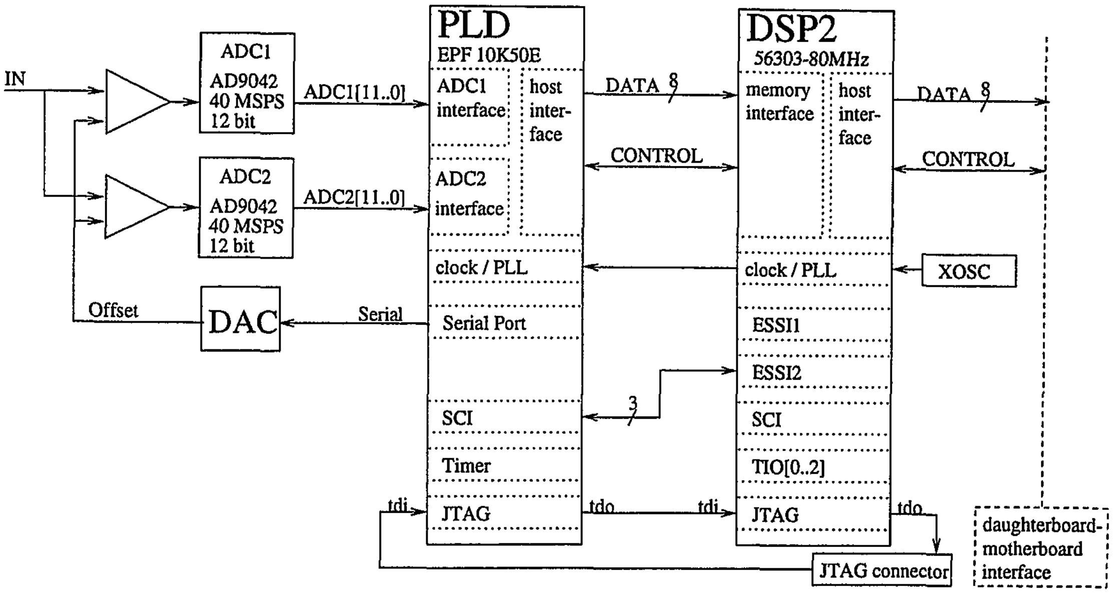

Figure 18 Blockdiagram of the PPADC daugtherboard (Courtesy of W. Gast).

of a compact, modular system, which allows up to 8 PPADC daughterboards to be plugged on a full size PCI/ISA motherboard. As main components, the motherboard contains a Digital Signal Processor (DSP), Programmable Logic Devices (PLDs) and memory for interfacing, control, and on-line histogramming. The block diagram of the PPADC daughterboard is shown in fig. 18. It employs two sampling Analog to Digital Converters (ADCs) of 12 bit resolution and 40 Msps/s speed each, to perform the A/D conversion of the preamplifier output signal, as well as a PLD and a DSP for on-line signal processing tasks.

5.4 Conditioning of the raw signals

5.4.1 Analog filtering and sampling

The first step of the signal preprocessing process takes place at the level of analog electronics. Since the preamplifier impulse response function is not an ideal low-pass filter, at the input of the sampling ADC an antialiasing filter is imposed to cut the high frequencies leaking from the preamplifier, as well as those acquired on the cable (pick-up noise) due to various environmental influences. Furthermore, for experiments involving high event rates, a differentiation is introduced to optimize the dynamic range, by reducing the probability of pile-up signals. The choice of the differentiation constant will be an compromise between the optimization of the dynamic range and the maximization of the signal-to-noise ratio. In a practical setup, the differentiation time constant of $50\mu s$ of a normal preamplifier, can be brought down to $5-10\mu s$. However, for experiments involving low event rates, the differentiation module can be switched off.

In order to extract information from the detector pulse shapes, it is important that the frequency components corresponding to the signal features have a power bigger than the noise power at those frequencies. It was shown in [50] that due to the serial delta noise which increases as a power function with the frequency, the signal-to-noise ratio becomes $S/N < 1$ for frequencies larger than about 100MHz. This is the first aspect which puts an upper limit on the required sampling frequency which, according to the Nyquist theorem, should be twice the frequency band. Besides this intrinsic limitation, the preamplifier bandwidth is a second factor which limits the bandwidth of the signal. The existing high performance preamplifiers have a bandwidth lying in the 20-30 MHz range. Correspondingly, the necessary maximum sampling frequency should be 40 to 60MHz. It is useful to note that if the Nyquist condition is fulfilled, interpolated points on the signal can be exactly obtained from the non-aliased sample points, if they are required for specific analysis tasks.

5.4.2 Digital triggering

The determination of the event occurrence is essential for the subsequent digital pulse shape analysis. Conventional analog triggering and timing methods in nuclear spectroscopy are based mainly on the Constant Fraction Discrimination (CFD) concept [52]. Since the whole analysis process is designed to take place in a digital environment, the event triggering should preferably also be based on a digital algorithm. In this way, the digitized triggering information can be directly used in the subsequent processing algorithms. Moreover, the digital environment provides a flexible mean for a triggering solution in the sense that the algorithm can be made recursive, since virtually any part of the input signal can be made available for analysis at any time.

The main requirements for a triggering system is to provide a low threshold level, a reasonable time resolution and to support high event rates. A low threshold level triggering is required since besides incident γ-rays, also scattered γ-rays of low energy have to be detected by individual detectors, which, if not noticed, contribute to a larger background in the final γ-ray spectra. Correspondingly, the triggering system should be designed to optimize the output signal-to-noise ratio S/N of the trigger signal. Normally, an improved precision of the triggering signal is produced on the expense of a reduced time accuracy. Therefore, by the modification of the parameters used in the algorithm, a compromise has to be found between accurate timing and low threshold discrimination. Moreover, triggering at high event rates is a sensitive issue, due to the difficulty of triggering pile-up events. Of particular concern is to identify signals of small energy occurring on the relaxation tail with small differentiation constant of a high-energy event. Such an example is depicted in fig. 19 **A**. The negative slope of the first event makes it difficult for the conventional discriminators to correctly identify the occurrence of the second low energy event.

Having considered the requirements stated above, a new triggering algorithm was developed, the main features of which will be discussed in the following. To design a triggering system, a number of filters have to be applied beforehand, in order to emphasize the important features and to eliminate the ones which are not of

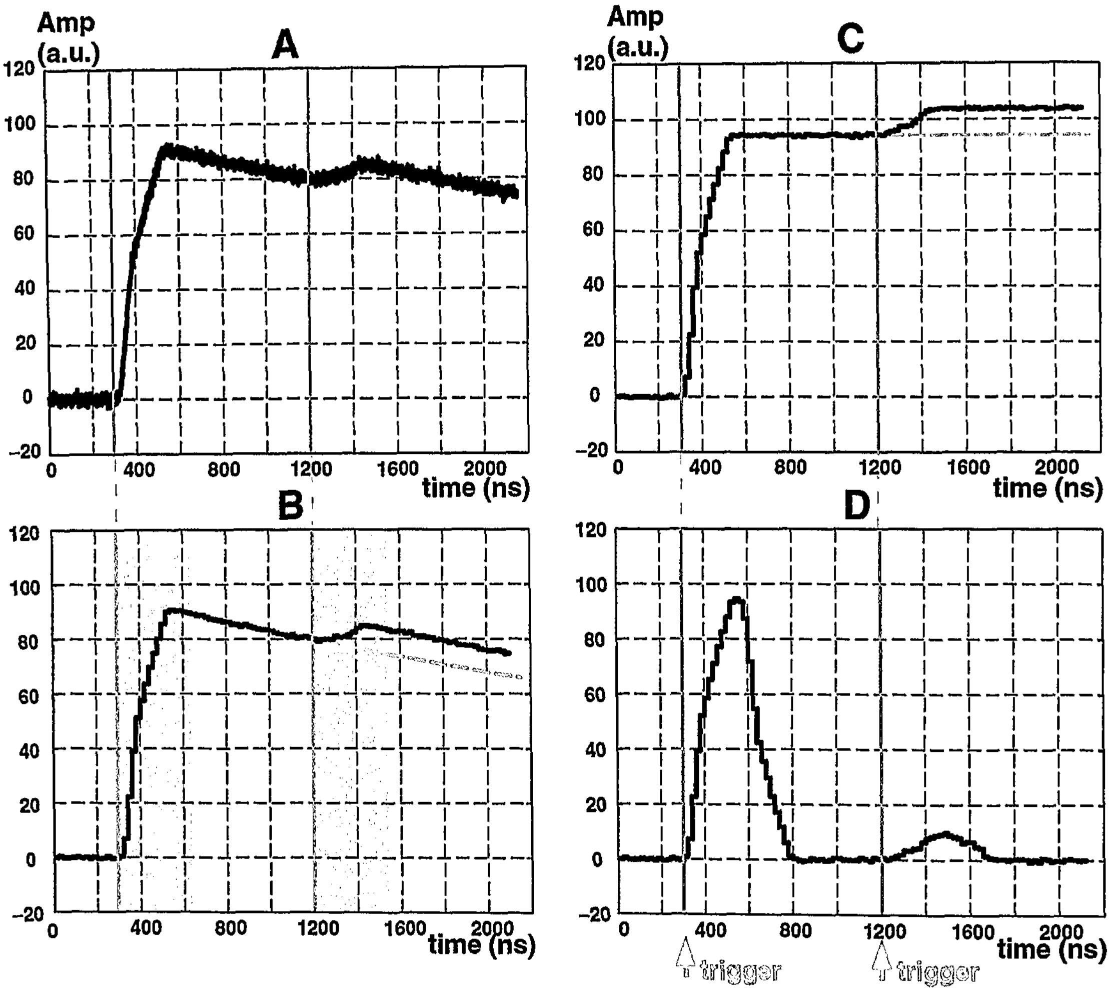

Figure 19 Processing stages required for event triggering of a typical detector signal. The raw preamplifier signal shown in frame (**A**) is formed by the contribution of two successive events. Frame (**B**) pictures the digitized version of the signal. The time range of the signal of interest for pulse shape analysis is represented by the shaded regions. As can be seen in portion (**C**), the preamplifier decay is cancelled by digital signal processing. In portion (**D**) a delay line differentiation has been used to create the signal ready for the triggering algorithm. The pulse beginnings are represented by the two vertical lines, which are determined by the triggering algorithm.

interest. Following the processing flow depicted in Figure 19, after the discretization of the analog input signal shown in portion **A** using a sampling Analog-to-Digital-Convertor (ADC) (see portion **B**), the filtering steps are pictured in frames **C** and

D. The exponential decay, which takes place following each charge collection event, is important for the limitation of the dynamic range, but it is a disadvantage for an accurate energy determination as well as for the triggering system. In Figure 19**B**, the dashed line indicates the shape of the exponential decay following the first event. For a correct identification of the second low-energy event, the decay component in the signal has to be cancelled. The decaying exponential is converted by means of digital signal processing to constant values, which are proportional to the energy deposited in the detector (see the dashed line in Figure 19 **C**). The corresponding filter which produces this result is obtained by adding to the current sample, the moving average of all previous samples weighted by the factor K_e [48]:

$$S'(k) = S(k) + K_e \sum_{j=-\infty}^{k-1} S(j) \tag{5.1}$$

The factor K_e is related to the decay time constant T_d through:

$$K_e = 1 - e^{-(\Delta/T_d)}. \tag{5.2}$$

with Δ being the sampling time interval. The application of this filter algorithm results in the digital values shown in 19C, which correctly represent the induced signal amplitude at each time. These are the data which are relevant for the determination of the deposited energy, as well as for subsequent pulse shape analysis for position determination. The time interval of interest for such pulse shape analysis is represented by the shaded regions in Figure 19 **B**. Actually, only the digital samples of these intervals will be stored and used for further pulse shape analysis.

The main idea of the present triggering algorithm is to determine the beginning of the leading edge, considering that the leading edge has a linear variation with time. To do this, the value of a moving average

$$A_w(k) = \sum_{i=k}^{k+w-1} S(i) \tag{5.3}$$

over a fixed window of w number of samples is compared with a threshold value h.

$$A_w(k) > h, \tag{5.4}$$

If this is "true", the first condition for the trigger is fulfilled, viz., that in the window w starting with the sample k, the amplitude of the signal is sufficiently large to conclude that an event took place. For a more accurate timing, and to avoid "time-walk" due to the variation in the signal amplitudes, another value $D_w(k)$ which is the moving difference between the second and the first half of the window w is calculated:

$$D_w(k) = \sum_{i=k+w/2}^{k+w-1} S(i) - \sum_{i=k}^{k+w/2-1} S(i) \tag{5.5}$$

and the second condition for triggering becomes:

$$D_w(k) = A_w(k)/2. \tag{5.6}$$

which in practice corresponds to a zero-crossing discrimination. This last condition is fulfilled when in the time interval w, the variation between the integral of the second half, and the integral of the first half indicates a linear variation. Ultimately, this condition can be understood as a linear regression of the rising shape.

To determine low energy events with a high efficiency, a bigger length of the window w is required. On the other hand, for a better time precision, a shorter, more localized window is suggested. Since the variations in the signals are the main features which are used for triggering, practically, the size of the window will be determined by the length of the signal rise time.

For a practical on-line implementation, for the aim of triggering, the two filters formed by the cancellation of the preamplifier decay and the delay line differentiation can be combined, the new set of sampling data to be used in the triggering algorithm being obtained as:

$$S_{new}(k) = S(k) - K_d S(k - w) \tag{5.7}$$

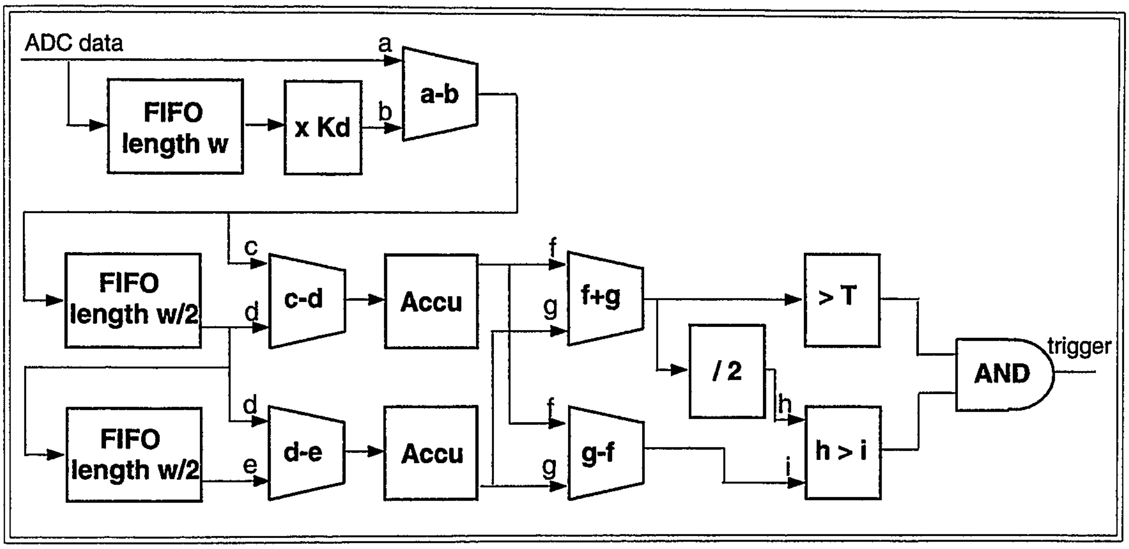

Figure 20 Diagram of the triggering algorithm. K_d stands for the correction factor (cf. eq. 5.7), w for the window size, and T for the threshold level.

where the factor K_d is $K_d = exp\{-w\Delta/T_d\}$, with w being the extent of the delay line (which is actually the same as the moving average window used in the triggering algorithm). This is equivalent to a delay line differentiation of the filtered signal with a time constant corresponding to the rise time of the signal (≈300ns). This procedure is required for the correction of the offsets, drifts and pile-ups of the input signal (see fig. 19 **D**). Accordingly, two consecutive events can be triggered if they are separated by a time interval of at least two times the differentiation time constant (i.e. around 600ns). The diagram of the triggering algorithm including data filtering, optimized for an on-line implementation, is shown in fig. 20.

The timing information offered by the triggering system has a limited resolution, mainly because of the approximation of the rising shape with a linear function, and is ultimately limited by the sampling time, since the trigger algorithm will point a certain sample index. A supplementary more accurate timing algorithm is imposed in the next processing level, for a determination of the event timing with a sub-sampling interval resolution.

5.4.3 The Normalized Step Response (NSR): A subsampling interval timing algorithm

Concept and algorithm

For the subsequent pulse shape analysis as well as for life time measurements experiments, a precise determination of the event timing is needed. The triggering algorithm has the important quality of being fast, sensitive. Though, for a precise time determination, an analysis on intervals shorter than the one used for triggering is imposed. The main idea behind the *Normalized Step Response* algorithm is that for small time intervals ($\approx$ 50ns), the main limitation in the bandwidth is given by the preamplifier transfer function, since it is known that the experimental signal $S(t)$ is obtained by the convolution between the detector current signal $I(t)$ and the preamplifier impulse response function $T(t)$ (see formula 4.16). Therefore, for an accurate determination of the position of sharp variations in the detector signal I(t) corresponding to the onset of an event, the preamplifier impulse response function has to be deconvolved from the experimental signal. For deconvolution problems, a very sensitive issue is the noise amplification. To put a limit in the noise amplification, regularization methods are applied, normally making use of information known a priori about the original signal which has to be reconstructed. In the present case, it is acceptable to assume that the beginning of detector current signal is a step function. The subsequent variations in the pulse shape due to the charge collection process are considered not to influence considerably the resulting preamplified signal shape in its very beginning. If a step function is chosen to represent the original signal, then there are only two parameters to be determined, namely, the amplitude of the step, and its position in time.

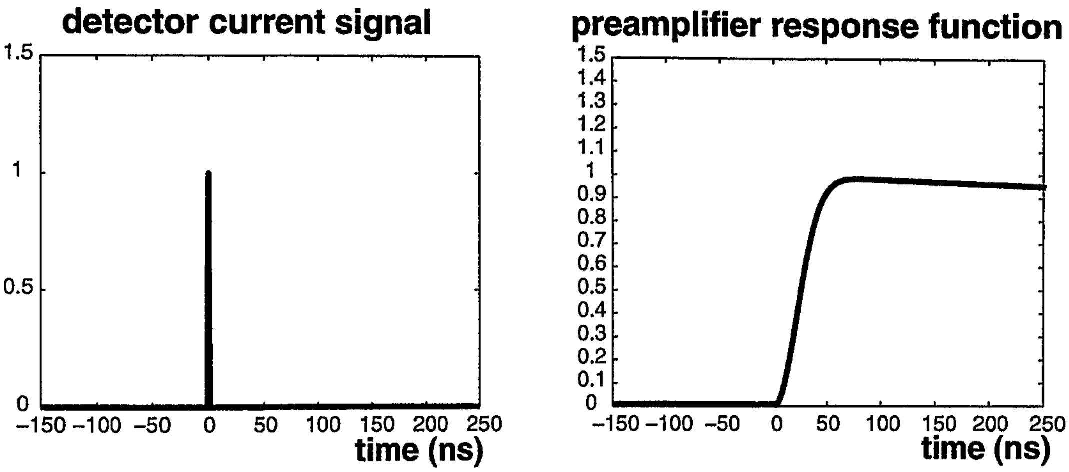

Figure 21 A typical preamplifier impulse response function. The corresponding detector signal $I(t)$ is a delta function.

In fig. 21, a typical preamplifier impulse response function $T(t)$ is pictured along with the corresponding detector signal. A good analytical representation of the preamplifier impulse response function $T(t)$ is given by 4.17.

Assuming that the typical detector current signal has a step like shape (Heaviside function) when an event occurs, and considering that the influence of the preamplifier decay is negligible in short time intervals, the corresponding preamplifier response function becomes:

$$S(t) = t - \frac{\sqrt{\pi}T_r}{2\sqrt{1.3}} erf(\frac{1.3t}{T_r}) \tag{5.8}$$

The shape of this function is shown in fig. 22. This is the typical shape of the preamplifier signal which is obtained immediately after the onset of an event. Out of this shape the parameters of the initial step have to be extracted. Since the determination of the amplitude is not of interest here, for a fast procedure, the deconvolution method should also normalize for the variation in amplitude of the step input signal. In the present approach, for each sample of index k a parameter R is calculated by

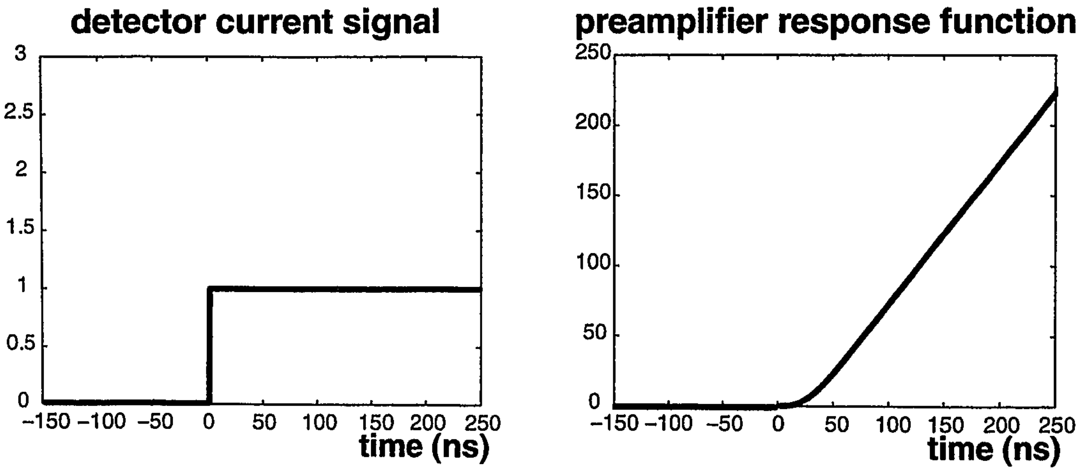

Figure 22 The preamplifier response function $S(t)$ of a Heaviside input function $I(t)$.

the normalized difference:

$$R(k) = \frac{S(k+1) - S(k)}{S(k+1) + S(k)} \tag{5.9}$$

If the parameter R is calculated for different delay times relative to the time corresponding to the current sample, the shape of fig. 23 is obtained. Having calculated the value R for a certain sample, then the delay time can be directly found from the function of fig. 23. The parameter R offers important advantages, (i) it is monotonic with the delay time, (ii) it normalizes for the variations of the step amplitudes, (iii) it is very local, involving samples from a short interval. The most efficient way for an on-line implementation of a timing determination system is to form a look-up table containing the delay times for various R values. The created look-up table is particular for the chosen preamplifier type. If a different preamplifier type is used, a new look-up table has to be generated for best results. The final timing procedure has the following steps:

1.) Calculate the value R with the relation 5.9, for the 4-5 samples following the sample indicated by the triggering algorithm;

2.) Check the look-up table containing the delay time t_d corresponding to the values R;

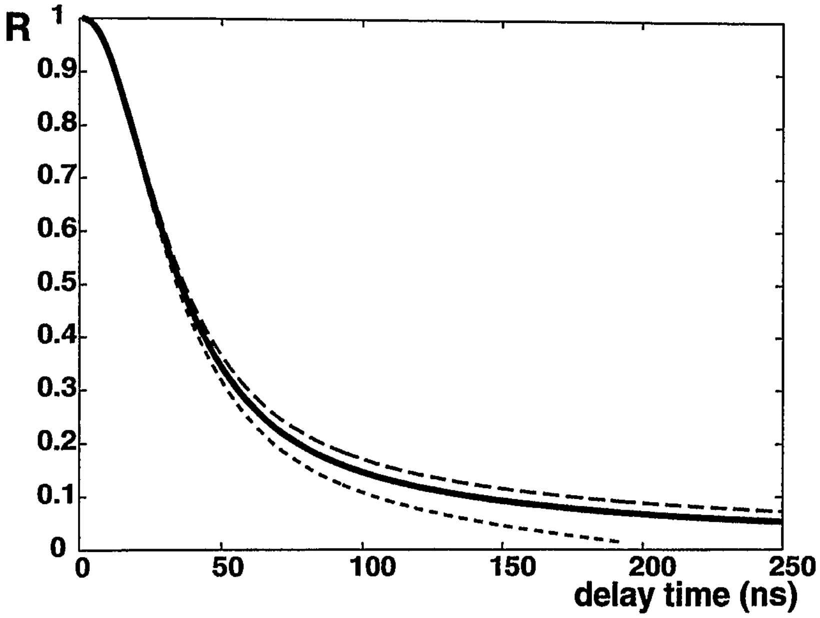

Figure 23 The variation of the parameter R with the delay time. The continuous line corresponds to a step input function, whereas the dashed and dotted lines correspond to steps with positive and negative slopes, respectively (see text).

3.) Evaluate the best estimated delay time t_d out of the 4-5 estimations;

4.) Eventually, further correct the obtained time, assuming that instead of an input step function, a step with a positive or negative slope can occur.

Regarding the processing step no. 3.), one should note that for the samples which are at the very beginning of the leading edge, a very bad signal-to-noise ratio exists, due to the very small amplitudes of the signal. On the other hand, if the considered samples are too late on the leading edge, the approximation of the input signal to a step function is not accurate any longer, so that the obtained time using samples in this region will be biased, being affected by the detector signal shape. This means that only a short time interval can be used for this procedure, which lies in the region of 30 to 70 ns for a preamplifier of 47ns rise time. This is also the reason why a number of 4 to 5 samples are checked after the trigger onset, in order to extract the one which indicate a delay in this time region. The point 4.) of the algorithm indicates that a correction can be made for a better time estimation, if the computing resources are sufficient, by assuming that the step has a nonzero slope $\alpha \neq 0$:

$$I(t) = \begin{cases} I_0 + \alpha t & \text{if } t > 0 \\ 0 & \text{otherwise} \end{cases} \tag{5.10}$$

and determining it. In Figure 23 the values of the parameter R for positive and negative slopes of the detector input function are shown as dashed and dotted lines, respectively. To find the slope α, a new parameter C is calculated as:

$$C(k) = R(k+1) - R(k) \tag{5.11}$$

The obtained $C(k)$ values are compared with values of the parameter C for a step function C_{step} at the estimated times t_d. The slope of the detector signal will be a function of $C(k) - C_{step}(t_d)$ and $R(k)$:

$$\alpha = f(C(k) - C_{step}(t_d), R(k)). \tag{5.12}$$

The corresponding time correction is obtained as:

$$\Delta t = \alpha \sqrt{a1 \frac{1}{R(k)^3} + a2 \frac{1}{R(k)^2} + a3 \frac{1}{R(k)} + a4}. \tag{5.13}$$

and finally, the corrected time delay becomes:

$$t'_d = t_d + \Delta t. \tag{5.14}$$

In principle, for an efficient implementation of this correction, another look-up table can be made containing the values Δt as function of R and $(C - C_{step})$. Nevertheless, as it will be indicated by the results of this algorithm applied on experimental data, the correction will bring only a small improvement for delay times in the 30-70ns region.

One should mention that, following the processing flow for pulse shape analysis, after an accurate determination of the beginning of the pulse by using the sub-sampling interval timing algorithm, a defined number of samples which cover the time interval of the leading edge will be stored for further analysis, since only this part of the signal contains features which are relevant for the determination of the interaction position. The next section (5.5) will discuss the treatment of these data.

Results

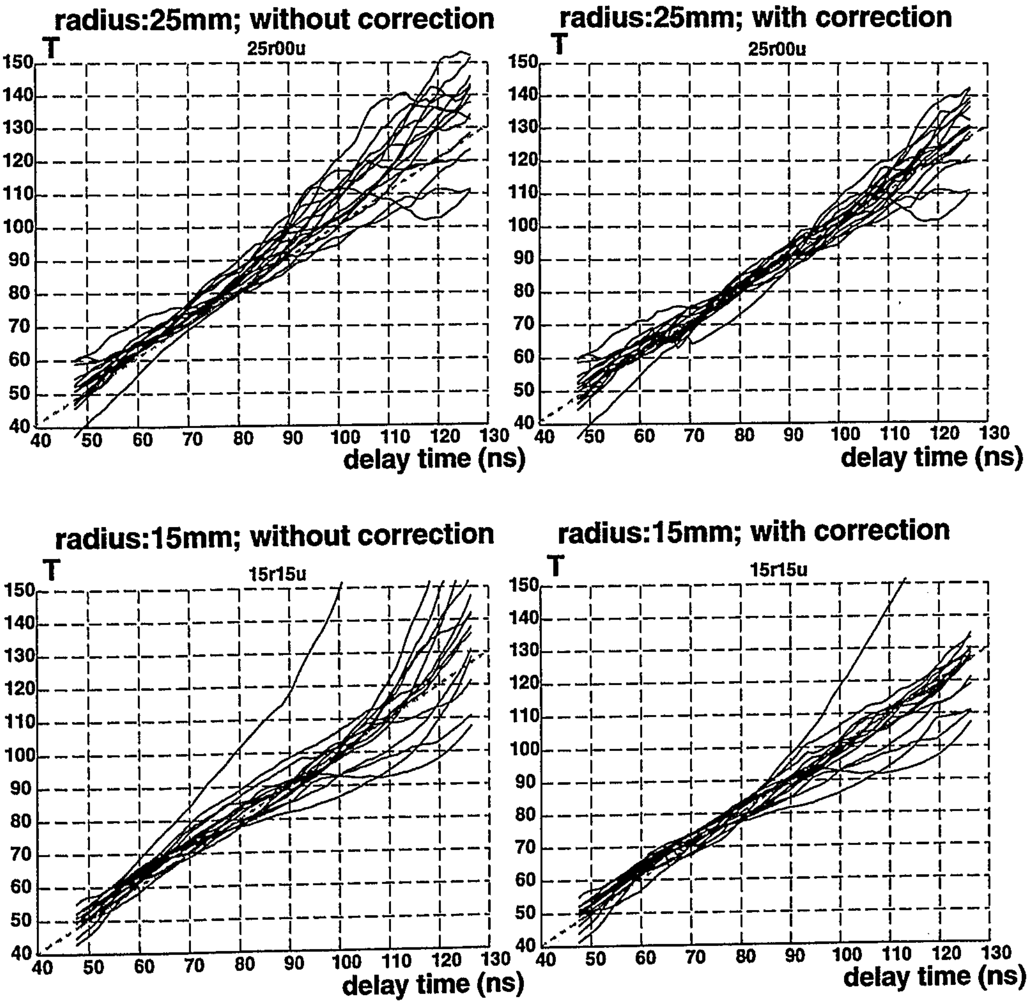

Figure 24 Results of the timing algorithm applied to experimental signals for two irradiation radii. Left: no corrections were applied; right: corrections were applied considering the detector signal as being a step function with a constant slope (see text).

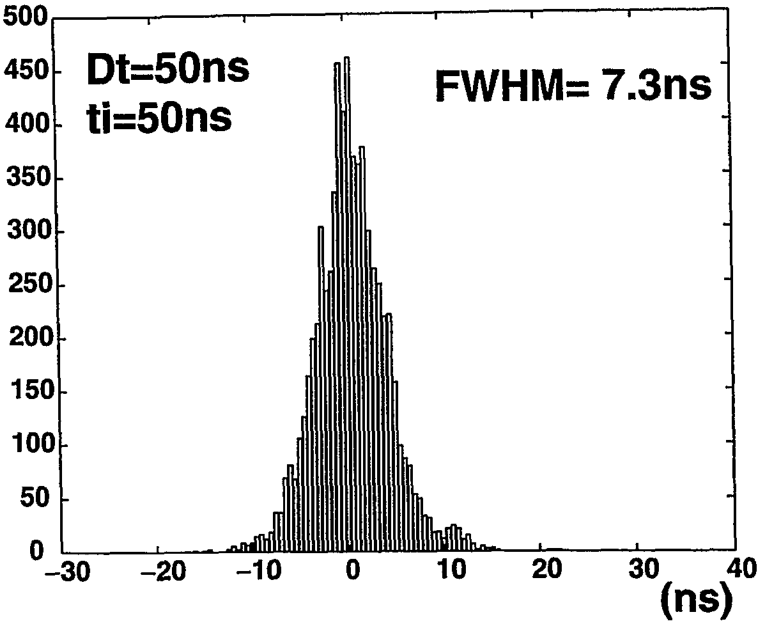

Figure 25 Time resolution obtained with the *Subsampling Interval Timing* algorithm using experimental signals of an EUROBALL type Ge detector.

The algorithm presented above was applied off-line to experimental signals taken with an EUROBALL type Ge detector. The 511 keV positron annihilation quanta of a ^{22}Na source were used in the measurements. The preamplifier had the impulse response function described by the relation 5.10, with $T_r = 47ns$ and $T_d = 50\mu s$. The preamplifier pulse shapes were recorded using a digital oscilloscope with a sampling rate of up to 1 Gs/sec and 8 bit resolution. An external trigger signal for the oscilloscope was obtained by requiring a coincidence between a NaI(Tl) scintillator and the Ge detector. In this way, the trigger time reference of the recorded pulses was defined by the constant-fraction discriminator of the scintillator, having the time resolution of the scintillator. Since the observation of the time performance is of interest for different detector pulse shapes corresponding to different interaction radii, between the ^{22}Na source and the Ge detector, a 1.5mm collimator was used, allowing for an irradiation of a well defined region.

Using the acquired signals, the data were oversampled to emulate a 20MHz sampling frequency, obtaining in this way similar data as in an on-line analysis system. Fig. 24 presents the results of the timing algorithm as function of delay time for two interaction radii. Ideally, for a perfect time determination, a diagonal line should be produced. One can observe deviations from the diagonal especially at large delay times, due to the variation of the detector current signals. The results are presented for time determination without corrections, and including corrections for shaping. The corrections have hardly an effect on the timing performance at small delay times. Fig. 25 represents the histogram of the time spectrum obtained using the timing algorithm on experimental signals taken at different interaction radii.

5.4.4 Determination of the released energy

For an accurate determination of the released energy in a digital environment, there are already available reliable algorithms. The Moving Window Deconvolution method [48,49] is based on a time invariant filter able to accurately extract the released energy by deconvolving the decaying exponential of the preamplifier. In this way, the resolution degradation due to the ballistic deficit effect can be corrected, and it gives an improved resolution at high count rates.

5.4.5 Results of implementation of algorithms on the PPADC

An on-line implementation of the timing algorithm was made using the digital electronics (PPADC) presented in section 5.3.2. Being a prototype, the PPADC module was not completely optimised in what regards the noise in the analog part of the electronics, cross-talks existing with the digital part. Therefore, an increased

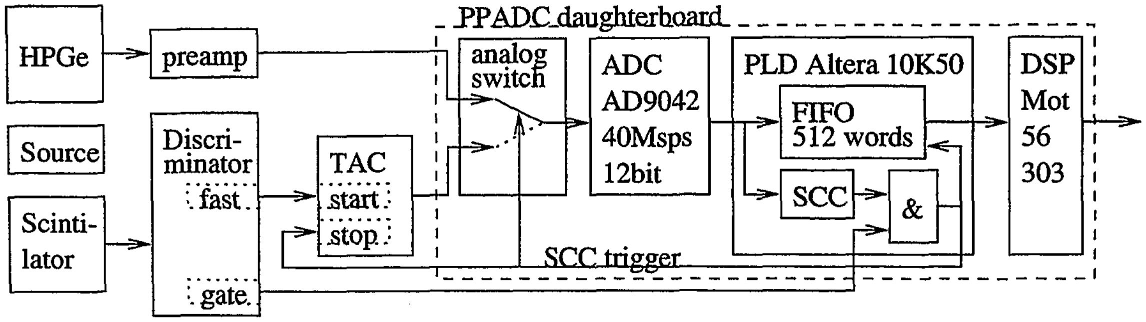

Figure 26 The acquisition diagram for timing measurements.

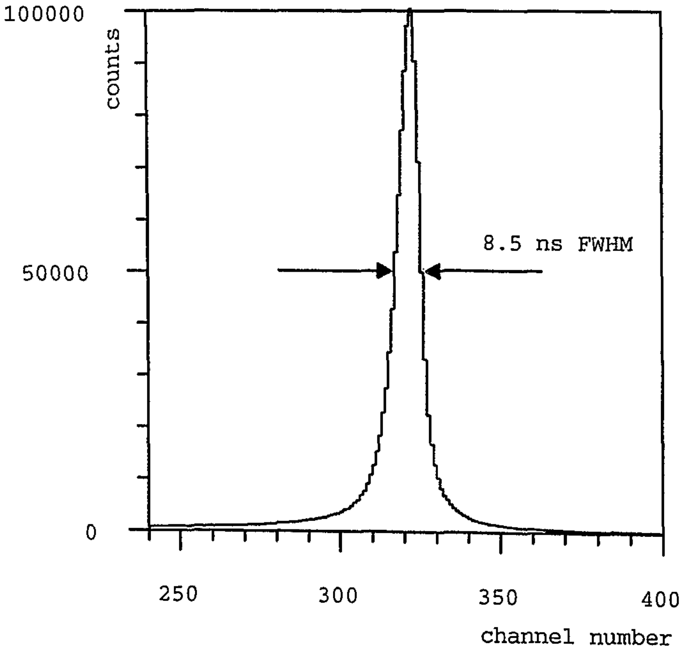

Figure 27 The measured time spectrum for full dynamic range.

noise was observed in the sampled detector signals as compared with signals acquired with a common digital oscilloscope. Despite the noise problem, it was still possible to obtain good results by using an on-line implementation of the proposed NSR timing algorithm. The electronic system for time measurements is presented in Figure 26. For the measurements, a ^{60}Co source was used, and a coincidence setup was made between the Ge detector signal and a lead glass scintillator signal. As a time reference, the constant fraction discriminator signal taken from the scintillator was used. The obtained time spectrum for the full dynamic range is shown in Figure 27. The corresponding full width at half maximum (FWHM) is 8.5ns. It is expected that with an optimized analog electronics, the performances can be further improved. In the table below, the performance of the NSR algorithm implementation are presented along with the performance of two other implemented algorithms which use linear and quadratic regressions for timing measurement.

Table 4 Performance of the Normalized Step Response (NSR) timing algorithm obtained with the PPADC in an on-line implementation compared with other two algorithms: the linear and quadratic Extrapolated Baseline Crossing algorithms: EBC1 and EBC2 respectively.

	Full dynamic range		Dynamic range 1.0-1.4 MeV	
Algorithm	FWHM[ns]	Efficiency[%]	FWHM[ns]	Efficiency[%]
NSR	8.5	68.5	6.5	80.2
EBC2	9.0	63.4	7.0	79.9
EBC2	14.0	63.1	11.5	76.8

5.5 The discrete wavelet transform for signal preprocessing

5.5.1 Optimum signal representation

Preprocessing concepts

As pointed out in section 4.4, due to the complexity of the detector signal shapes, an analytical approach to represent and to recognize the signals is hardly feasible, hence a pattern recognition system will be used to identify the interaction positions. This means that a data base has to be constructed which has to cover the various expected classes, and the recognition system has to identify to which class the experimental data pertain. A "class" corresponds to a set of particular interaction positions characterized by a specific signal shape. It will be seen in section 5.7, in which way the classes are used and correlated to extract the interaction positions. For most pattern recognition applications, for better performances it is necessary to transform the raw data into a new representation before feeding them to the recognition system. To a large extent, a careful optimization of the preprocessing will determine the success rate of the identification, being one of the most important steps in the development of the analysis method.

In the present case, the problem is even more demanding than for a common pattern recognition problem, since the aim is not only to identify a single class within the experimental data, but a superposition of different classes with different weights. This request of having the possibility to decompose among different components in the experimental signal on a noisy background, emphasize the importance of the preprocessing. In this respect, the new representation of the signals should concisely highlight the features characterizing the signals. It should also be able to differentiate the signal components corresponding to different classes. These representation aspects suggest two fundamental questions: What are the features characterizing the signals, and are these features capable to orthogonalize the various classes? This last point is very important regarding the possibility to successfully decompose different classes. Ideally, the features should be represented by vectors which are orthogonal to each other for various classes. This ideal situation cannot be found in our case, since the shapes are changing gradually with the position of interaction, leading to a smooth variation of any parameters that would be chosen. What can be done is to find the representation that would maximize the separation between classes which correspond to more distant physical positions.

Another preprocessing approach would be to consider linear or non-linear combinations which leads towards a decrease of the dimensionality of the original data, for faster, more efficient recognition with less data to be transferred and analyzed. Ideally, following such a preprocessing, a few variables will be obtained, which could be even directly identified with the physical features of interest (for example, in our case, the radius, azimuthal angle and the depth of interaction). In this hypothetical situation, each class is characterized by these three parameters, which are the cylindrical coordinates of the interaction positions. This is an extreme case, where basically, the identification takes place at the preprocessing level, no subsequent pattern recognition being necessary. But such extreme data reduction will make the decomposition of multiple interactions impossible, since usually even a slight reduction in the dimensionality creates a loss of information. Following this path, another question appears, namely, which is the minimum dimensionality necessary to preserve the most important information? As it has been already presented in subsection 5.4.1, the choice of the sampling frequency is the first factor which determines the amount of data to be read. It was shown there that the preamplifier bandwidth and the noise spectrum determine the maximum frequency sufficient to sample the signal. Any further data reduction has to start from this point. The following sections will try to better answer the question regarding the dimensionality of the data.

The main features of signals

In order to identify the features characterizing the signals, the variation in the detector pulse shapes has to be analyzed for different positions of interaction. In chapter 4 it was extensively presented how the drifting charge carriers induce signals in the detector segments. It has been pointed out that, depending on the interaction radius, the electrons and holes have different drift times, cumulatively inducing charge currents which drops in amplitude at the moment at which the carriers reach the electrodes. Correspondingly, it can be made a direct correlation between the radius of interaction and the position in time of the steps in the signal amplitude. Besides, a variation in the amplitude of the induced signals will exist, depending on the weighting fields through which the charge carriers travel, which depend on the distance from the segment border. Since our aim is to identify the full three dimensional position of the interaction, all these variations in the signals have to be analyzed and identified.

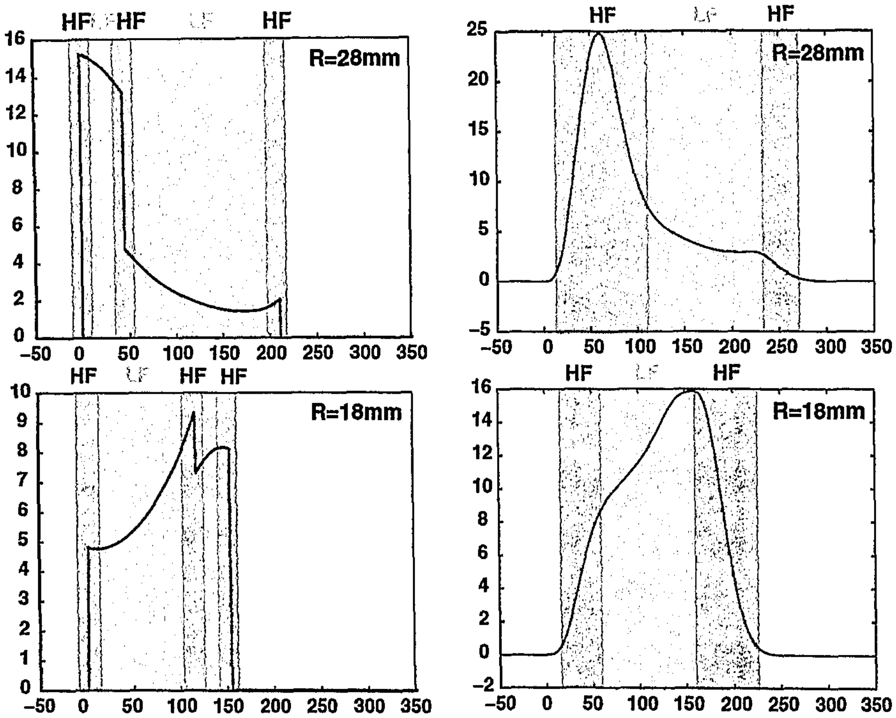

The detector signal

The differentiated preamplifier signal

Figure 28 Two examples of signals corresponding to interaction points at different radii. The low and high frequency components of the signal are positioned differently for the two cases. Left: the detector current signal, right: the differentiated preamplifier signal. LF=interval of low frequency, HF=interval of high frequency

Summarizing these aspects, it becomes evident the strong nonstationary character of the detector signals, with relatively small variations during the drift time of the carriers and steep slopes at the moment the carriers reach the electrodes. In the frequency domain, this is equivalent with the existence of low frequency components stretched in the time domain over longer intervals, and high frequencies for short periods, corresponding to the steps in the signal. In fig. 28 examples of two signals corresponding to interaction points at different radii are presented. It is to be compared the nonstationary characteristics of the signals with the different positioning of the low and high frequency components. Even after the preamplifier limits the bandwidth, washing out discontinuities of the detector signal, the low and high frequency components are distinguishable. Actually, the preamplifier shaping produces one of the main limitations for extracting the features of the pulse shape. The section 5.7.1 will have a complete overview on the other factors which limit the attainable position resolution.

The portions with low and high frequency components are the features which characterize the signal and should be extracted to produce the new representation of the data. For this purpose, a specially designed wavelet transform will be used, which will be presented in the next section. By comparison, a simple time-domain representation is not the ideal choice, since it is very sensitive to the noise, especially when it comes to the problem of decomposing several interactions, and it is not directly related to the features of interest. A value in the time domain has no relevance by itself, but only in relation to the neighbouring samples, at different scales in time. A Fourier analysis is again not suitable, since it is obvious that the signal, due to its non-stationary background, cannot be correctly represented by a Fourier series.

5.5.2 Discrete wavelet transform (DWT)

Introduction

For most signal processing problems, the Fourier transform has a paramount importance. From basic filter design to complex spectroscopic methods, the Fourier transform made the connection between the time-domain signal and its frequency components. However, in many applications requiring the analysis of non-stationary signals, a new method was necessary to give time resolution to the frequency components of the signal. For this purpose the *short time Fourier transform* (STFT) (or Gabor transform for the discrete case) was introduced [54]. The STFT is basically a Fourier transform applied on windowed intervals. Using this transform it was possible to gain time resolution, certainly on the expense of loosing in frequency resolution. The main draw-backs of STFT were: the increased computational complexity of the algorithm, the redundancy of the transformed data, and the fixed size of the analysis window, which did not allow for a variable time resolution depending on the frequency, or the other way around, it did not allow for a variable frequency resolution depending on the time scale.

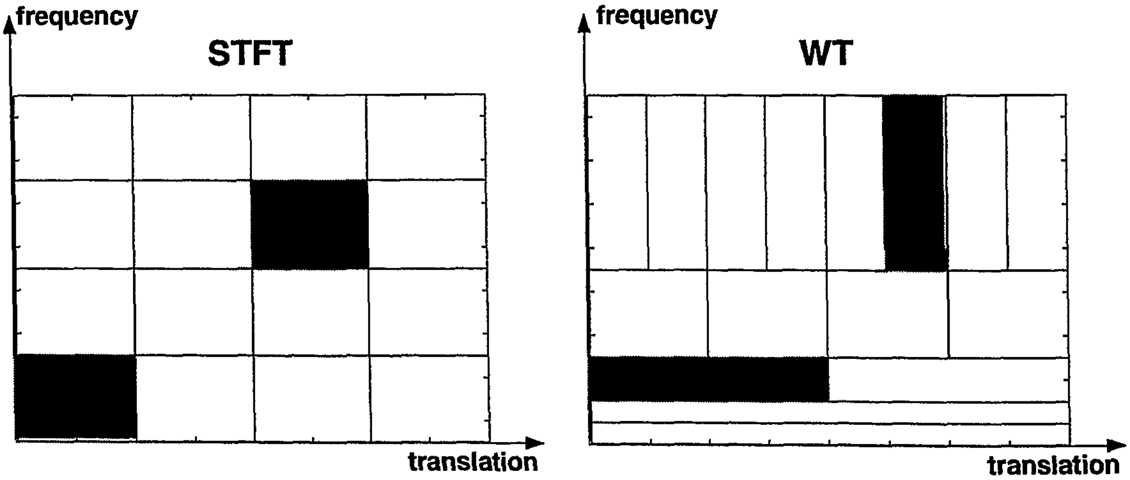

Figure 29 Comparison between data representation for short time Fourier transform (STFT) and wavelet transform (WT) in the time-frequency plane. It should be noted that the sampling grid is uniform for STFT and dyadic (i.e. varies in frequency and time translation by a factor of two) for WT.

The theory of the *wavelet transform* (WT) was developed rather recently as an alternative to the short time Fourier transform. In a general definition, the wavelet transform is based on *analysis functions*, or *basis functions* which are translated and dilated versions of a single prototype function, called *mother wavelet*. The standard result of a wavelet transform is a scale-time representation of the signal. The "scale" is equivalent to the inverse of frequency. The main advantage of the wavelet transform over the short time Fourier transform is that it gives good time resolution to the high frequency components of the signal, and bad time resolution, but good frequency resolution, at low frequencies (see fig. 29). This is exactly what is needed for most of the practical situations where non-stationary signals are involved, since they are usually formed by short bursts of high frequencies, on a background of low frequencies stretched over long time intervals. This is what makes the wavelet transform ideal in the applications involving non-stationary signal analysis.

Discrete wavelet transform and multiresolution

The main classification of the WT, similar to FT, distinguishes the *continuous wavelet transform* (CWT), which applies to continuous signals, and the *discrete wavelet transform* (DWT) which applies to discrete signals. Since the topic of this dissertation is the analysis of discrete signals, in the following the discussion will restrain to the definition and the properties of the DWT. It should be noted that the discrete wavelet transform is a version of the WT which is applied on discrete signals of finite length, with discrete translations and scales.

The wavelet basis w_{jk} is generated by dyadic (i.e., by a factor of two) rescalings and translations:

$$w_{jk}(t) = 2^{j/2} w(2^j t - k) \tag{5.15}$$

where j and k are integers defining the scale and the translation in time. Accordingly, the scale index j gives the width of the wavelet, whereas the translation index k gives its position in time. For either continuous or discrete case, the wavelet transform of an input function $f(t)$ is defined as the convolution between the input function and the wavelet basis functions:

$$W_w f(j,k) = \int f(t) w_{jk}(t)\, dt \tag{5.16}$$

The power of DWT over CWT is that the basis functions $\{w_{jk}\, j, k \in \mathrm{Z}\}$, if chosen careful, can form an orthonormal basis [55], especially if dyadic shifts and scalings are chosen. This property assures a very compact representation of the signal, and permits the computational algorithms to be made very fast due to the concept of "multiresolution". The *multiresolution analysis*, corresponding to an orthogonal wavelet transform, represents the type of analysis which characterizes the signal at different scales simultaneously, decomposing the signal space into a sequence of closed subspaces [56]. There is a very close theoretical connection between the multiresolution analysis represented by wavelets and the two-channel filter banks theory [55, 56, 57]. The standard application of the multiresolution analysis is to form a series of half-band filters which, for each scale, divide a spectrum into a high and a low frequency band.

For a scale j, the corresponding wavelet subspace W_j contains the combination of functions $w(2^j t - k)$, which can be defined using the *wavelet equation* that represents the wavelet function as a weighted sum with the coefficients b_k of the compressed and shifted versions of a scaling function $\Phi(t)$:

$$w(t) = \sqrt{2} \sum_{k=0}^{N-1} b_k \Phi(2t - k) \tag{5.17}$$

N stands for the number of coefficients. The coefficients $\{b_k, k = \overline{0\!:\!N-1}\}$ are named *wavelet coefficients*, and can be obtained from the *scaling function coefficients* $\{a_k, k = \overline{0\!:\!N-1}\}$ as:

$$b_k = (-1)^k a_{N-k-1} \tag{5.18}$$

The *scaling equation* defines the dilation of the scaling functions Φ, as a weighted sum of compressed and shifted versions of itself:

$$\Phi(t) = \sqrt{2} \sum_{k=0}^{N-1} a_k \Phi(2t - k) \tag{5.19}$$

It should be noted that the choice of the scaling function coefficients $a_k, k = 1 : N$ will determine the compact support of the wavelet (equivalent to a finite impulse response filter), and the orthogonality of the wavelet functions at all scales and translations:

$$\int_{-\infty}^{\infty} w(2^j t - k) w(2^J t - K)\, dt = \delta(j - J)\delta(k - K). \tag{5.20}$$

The theoretical framework developed by Mallat [56] requires a number of properties for the scaling function subspaces V_j. To be accomplished, the scaling function coefficients a_k must satisfy linear and quadratic constraints. The complete proof for the necessary and sufficient conditions to construct orthonormal wavelet bases is presented in ref. [58]. For the approximation of a polynomial signal with an accuracy h^p ($h = 2^{-j}$ is the scaling level), it is required that the Fourier transform of the scaling function has zeros of order p at all points $\xi = 2\pi n$. This translates into:

$$\mathcal{A}^{(m)}(\pi) = 0, m = \overline{0:p-1} \tag{5.21}$$

where $\mathcal{A}(\xi) = \frac{1}{2} \sum_{k=0}^{N-1} a_k e^{ik\xi}$ is the Fourier transform of the scaling function coefficients, equivalent to the transfer function of the low pass filter, in filter banks parlance. In terms of scaling coefficients, the relation is written:

$$\sum_{k=0}^{N-1} k^m a_k = 0, \;\; m = \overline{0:p-1} \tag{5.22}$$

The zeros order p is related to the number of coefficients and can have the maximum value $p = N/2$.

For normalization, it is desired that the area under the wavelet curve to be unity, which means that:

$$\sum_{k=0}^{N-1} a_k = 2, \tag{5.23}$$

and the sum of the squares of all coefficients is two (equ. 5.24).

The condition 5.18 assures the orthogonality of the wavelet basis across the scales. For orthogonality of the wavelet basis at different translations, the sum of the product of coefficients translated by a multiple of 2 should be zero:

$$\sum_{k=0}^{N-1} a_k a_{k+2l} = 2\delta_{l,0}. \tag{5.24}$$

This equation translates in the frequency domain as:

$$|\mathcal{A}(\xi)|^2 + |\mathcal{A}(\xi + \pi)|^2 = 1. \tag{5.25}$$

The scaling (a) and wavelet coefficients (b) obeying equ. 5.18, are named quadrature mirror filters in the signal processing terminology, and represent the low-pass (h) and high-pass (g) impulse response functions. The equivalence between the two pairs of terms is exact to a $\sqrt{2}$ factor:

$$h = \frac{1}{\sqrt{2}}a; \; g = \frac{1}{\sqrt{2}}b; \tag{5.26}$$

The simple definition of the DWT, forming bandpass filters based on a single set of coefficients, allows further important theoretical derivations, the theory of unitary finite impulse response filter banks providing a tool for exploring orthonormal wavelets [57].

DWT in signal processing

A major field of applications of the discrete wavelet transforms was found in digital signal processing, and is directly related to the need to represent digital data at different scales [59]. If the wavelet basis is chosen to best adapt to the signal, the result of the DWT will be a sparse representation of the signal. This property gives an important use of the wavelets, namely in data compression. Depending on the signal type, the compression algorithms based on wavelets succeed to obtain compression ratios ranging from 8:1 for high fidelity audio data to 140:1 for color dynamic images (video). For relatively "smooth" wavelets like the Daubechies wavelet family [55], the digitized signals can be efficiently interpolated with a good accuracy by a representation in terms of scaling and wavelet functions [56]. Further improvements with emphasis on denoising are described in [60].

In the present application it is of importance also that the wavelets can be used to highlight the features of the signals at different scales. Various applications were found in multiscale feature detection [57], in medical applications [61], image analysis [62], seismology [63]. A general disadvantage of using DWT for pattern recognition problems is that an aperiodic shift in time yields a different wavelet spectrum, making DWT shift variant. This is a general weak point of using wavelets for pattern recognition, since in most applications, a time reference in relation to which to compute the wavelet transform is not known. Nevertheless, new constructions have been developed trying to avoid this inconvenience [64], but on the expense of significantly increased computing requirements.

5.5.3 *Algorithm for computing DWT*

The method described in [65] offers a fast algorithm to decompose an $L = 2^M$ length signal into its wavelet transform coefficients. In case the signal does not have a 2^M length, an extension can be made by zero-padding, symmetric or anti-symmetric reflection, or periodic extension. The choice of the procedure should be adapted to the specific problem. For filter lengths bigger than $N = 2$, a similar border treatment is applied to the signals having a length of power of two, using supplementary $N - 1$ data points in the continuation of the border.

The set of $L = 2^M$ input data $\{s^0(l),\ l = 1, ..., L\}$ is decomposed in M sequential steps, each step corresponding to a scale level, starting with the smallest

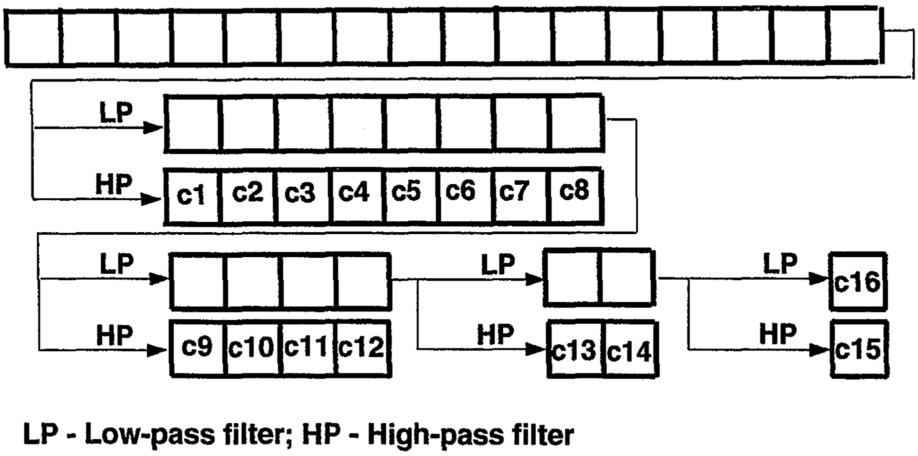

Figure 30 Diagram for representation of data flow for calculation of DWT coefficients. LF=low pass filter, HF=high pas filter

scale. For each scale, the signal is transformed using a low-pass and a high-pass filter produced by the scaling coefficients (a) and wavelet function coefficients (b), respectively (see fig. 30). The resulting DWT coefficients are noted by $\{c(l),\ l = 1, ..., L\}$. After each step j, following the low-pass filter, a half number "smoothed" data are obtained, which are fed as input data to the next step, and the high-pass filter produces the final DWT coefficients at scale j. For the step j, the corresponding decomposition can be written as:

$$s^j(n) = \frac{1}{\sqrt{2}} \sum_k s^{j-1}(k) a(2n-k), \tag{5.27}$$

$$c^j(n) = \frac{1}{\sqrt{2}} \sum_k s^{j-1}(k) b(2n-k), \tag{5.28}$$

Finally, the DWT coefficients are concatenated from $c^j(n)$ as:

$$\left\{c^{(j=1)}(1, ..., L/2), c^{(j=2)}(1, ..., L/2^2), ..., c^{(j=M)}(1), s^{(j=M)}(1)\right\} \tag{5.29}$$

For orthogonal DWT, the original signal can be exactly reconstructed by applying the above procedure in the inverse order. Due to the fact that it is based on convolutions, the algorithm can also be made parallel, being suitable to be implemented on a Programmable Logic Device (PLD) for a fast on-line implementation.

5.5.4 The 'Wide-band' wavelet transform

In this section the use of a particular wavelet will be discussed for our application. In this context, the *wide-band* discrete wavelet transform will be introduced, which is an orthogonal transform able to efficiently decompose the particular signals created by a segmented large-volume Ge detector.

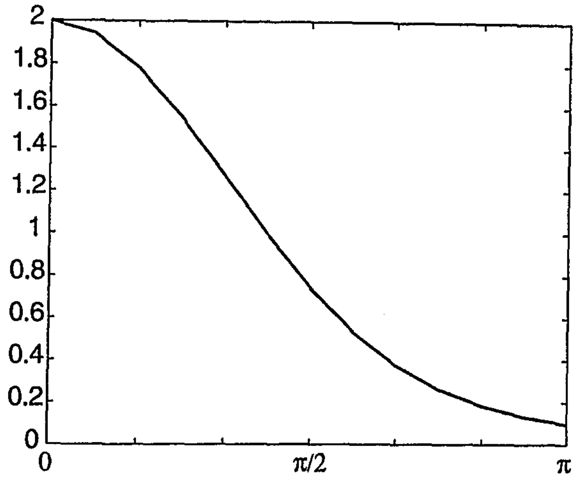

Figure 31 The transfer function of a preamplifier with 46 ns rise-time at a sampling frequency of 50 MHz.

In order to justify the use of a non-standard wavelet, a few remarks have to be made regarding the experimental pulse shapes obtained from these detectors. As explained in section 5.5.1, the detector pulse shapes consist of slow varying signals in certain intervals, bordered by sharp steps. Due to the filtering of the preamplifier, the large-band frequencies corresponding to the discontinuities in the signal, are drastically cut being shaped by the preamplifier transfer function (see fig. 31). Unfortunately, for a preamplifier optimized for good energy resolution, the transfer function is far from being an ideal low-pass filter, which results in a very bad transmission of the high-frequency components. As a consequence, in order to obtain information about the position of the discontinuities in the signal, the small scale wavelet coefficients, and the corresponding high-pass filter should cover as good as possible those frequency intervals where significant power is given by discontinuities. This is the case when the high-pass filter is well extended into the low frequency region. Correspondingly, the ideal low-pass filter should cover the frequency intervals which correspond to the slow variations of the signal, which for the present case, assuming a sampling frequency of 50 MHz, goes up to $\omega = \pi/6$. For this case, the *wide-band* wavelet transform (WB4) is introduced. Due to restraints in the design of orthogonal wavelets, symmetric low-pass and high-pass filters are assumed. Since a good time resolution of the low-scale coefficients is needed, a wavelet with small support is chosen. Hence, a length-4 wavelet is considered. It was found that for a value of $\alpha = 2\pi/3$ in the Resnikoff parametrization [66], acceptable half-band filters are produced (see fig. 32).

According to the Resnikoff parametrization [66] of orthonormal wavelet basis, the length-4 scaling coefficients are:

$$\begin{aligned} a0 &= (1 - cos(\alpha) + sin(\alpha))/2, \\ a1 &= (1 + cos(\alpha) + sin(\alpha))/2, \\ a2 &= (1 + cos(\alpha) - sin(\alpha))/2, \\ a3 &= (1 - cos(\alpha) - sin(\alpha))/2, \end{aligned} \tag{5.30}$$

One should note that this choice of wavelet transform will not produce a sparse representation of the signal, but is mainly designed to sort and separate the structures in the given signal, and to emphasis the small scale DWT coefficients. In the present case a data reduction is not intended, since anyhow, the number of available samples which provide useful information is low. Why is then multiresolution important for the present case? The answer is that from the determination of low scale coefficients, localized temporal information of the fast varying features of the signal can be obtained, whereas for the higher scale coefficients, the more global features of the signal can be emphasized, being also more independent on the noise. This feature allows for noisier signals to be correctly identified by the subsequent

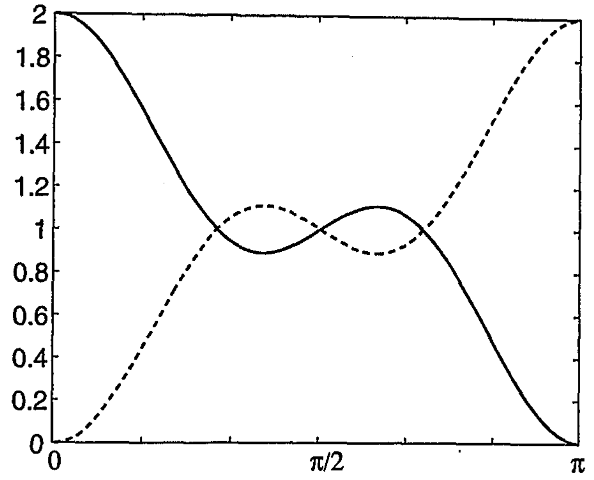

Figure 32 The transfer function of the low-pass and high-pass filters corresponding to the *wide-band* discrete wavelet transform (WB4).

identification system, by weighting more on the large scale coefficients. Another important advantage is that an orthogonal wavelet transform is invertible. The inverse transformation matrix which transforms data from the wavelet domain into the time domain is just the transpose of the direct transformation matrix. This creates the possibility to recover the initial experimental shapes, if needed.

5.6 Systems for the identification of interactions

5.6.1 Introduction

In the previous sections of this chapter, were presented methods for the conditioning and preprocessing of the detector segment signals. Of special importance were the presented algorithms for signal triggering, subsampling interval timing algorithm, and the signal shape preprocessing using the "wide-band" wavelet transform WB4. Although the involved procedures were tested on particular detection systems, they are relatively general, allowing for a use with a broad range of segmented semiconductor γ-ray detectors.

In the following, to investigate identification systems which allow effectively to determine the interaction positions using the shapes of the segment pulses, the detection system has to be clearly defined. Although the main principles described in the following can be used also for other detector designs, the algorithm as a whole is rather particular. In this section an 8x4 segmented coaxial Ge detector is assumed for identifying interactions in full three dimensional coordinates. The choice of this design, was explained in section 5.2 along with its main features. As a simplified example, an 8x1 segmented coaxial detector will be also considered, which is able to identify interactions in two dimensions. Actually, this design has the same physical dimensions as the other design, but does not have the 4-fold longitudinal segmentation.

The final aim of the identification system is to obtain relevant information which can be subsequently used by the tracking algorithm to reconstruct the sequence of interactions of a γ-ray in the Ge detector. Ideally, the relevant information is given by the full 3D positions and energies of each of the γ-ray interactions. To obtain this, the identification system can only use the pulse shapes of the detector segments. Since an analytical method to analyze the pulse shapes is hardly feasible, due to the complexity of the pulse shape formation, induced especially by the complexity of the weighting fields, an approach involving *pattern recognition* concepts is considered. For an effective pattern recognition system, a preprocessing of the raw data has to be made. In the present case this is accomplished with the help of the "wide-band" wavelet transform. The use of a pattern recognition system involves also the availability of "patterns" which are determined beforehand and are stored in a data base. In our case, this data base can be formed by storing the wavelet transform coefficients of the pulse shapes obtained either by simulations considering the real detector design, or by making pulse shape measurements with a Compton spectrometer. For either case, the data base produced for each segment has to contain a number of *pattern classes* which are characteristic for each interaction position possible to discriminate in that segment.

Since following an interaction, the power of the induced signals is significant not only in the irradiated segment, but also in its first neighbours, besides the recognition of the segment "patterns", the identification system has to provide an algorithm which correlates the information obtained from the neighbouring segments, and is finally able to determine the positions and energies of the interactions. This *correlation system* has also to decompose the different components found in the case of multiple interactions. Unfortunately, the decomposition will not be "unique" due to a series of factors which will be presented in the next section. In this chapter, identification systems for single interactions will be presented for position determination in full 3D coordinates for an 8x4 segmented Ge detector, and in 2D coordinates for an 8x1 segmented detector. At the end of the section, the identification systems are extended for multiple interactions.

5.6.2 Factors which limit the attainable position resolution

Intrinsic factors

A number of physical aspects closely related to the detection process are imposing a first limit in the attainable position resolution. The finite length of the photoelectron path, and the spatial distribution of the charge carrier clouds formed following photoelectron induced excitations, makes it difficult to find the initial position of the interaction, since already the formation of charge carriers takes place in an extended volume. The only way to get around would be to track also the paths of the photoelectrons, which is hardly feasible with Ge detectors. In the present work, all these factors were considered to affect the position resolution, and the identification methods were developed taking into account these realistic expectations.

The path length of photoelectrons The photoelectrons produced following a γ-interaction in the Ge detector loose their energy in the detector material through ionizations and excitations according to the formula derived by Bethe for the linear stopping power S_c [16] (see Eq. 4.4). Besides the energy loss through excitations and ionizations, the electrons are loosing energy by radiating *bremsstrahlung* due to deflections of their trajectories, but the proportion of energy loss through this process is small for the energies of interest here. The Eq. 4.5 represents the radiative stopping power S_r for energetic electrons. An approximation for the ratio between the two specific energy losses is given by the formula:

$$\frac{S_r}{S_c} \approx \frac{EZ}{700} \tag{5.31}$$

with the photoelectron energy E expressed in MeV, and $Z = 32$ for Ge. Fortunately, the produced *bremsstrahlung* is of small energy and is absorbed in close proximity.

Due to interactions with the orbital electrons and nuclei, the path of the electrons is not a straight line. However, the overall spatial distribution of the charge carriers produced by excitations, has a macroscopic value. Thus depending on the released energy, the photoelectron range and the corresponding spatial extent of the charge carriers is of about 1mm/MeV for Ge detectors.

The diffusion of the charge carrier clouds. Besides the spatial range of the charge carrier formation, during their drift in the detector electric field, the charge carriers diffuse in Ge leading to an increased cloud. As a consequence, the individual electrons and holes will have different pathes through the weighting fields of the segments, thus forming different induced signals in the detector segments. In this way, the overall influence on the detector segment will be an integral over a distribution of signal shapes.

Technical factors

In the category of *technical factors* which influence the position sensitivity are those which result from the design of the detector and of the read-out electronics. Theoretically, these factors can be adjusted for better performances, through a better knowledge of the involved physical processes, or a better technical design.

Uncertainties related to the charge collection process. To have a good control on the signal shapes corresponding to any position of interaction, and to be able to accurately simulate these signals, the charge collection process has to be well known for each interaction position, and the weighting fields of each detector segment have to be carefully calculated. There are a few factors which hinder a good knowledge of these aspects, though. The normal design of any Ge detector involves the existence of at least one **"open" surface** between the electrodes of opposite polarity.

This surface is treated against surface leakage currents by etching and passivation. Unfortunately, the influence of the passivation material on the electrostatic fields is not very well defined. Ideally, such surfaces should behave as electrostatical mirrors, which would correspond to Neumann border conditions. Since for the moment the technology is not fully developed and the knowledge of the influence of surfaces on the electrical field is approximative, one should count for the existence of electric field inhomogeneities especially at the edges of the detector. This limits the knowledge of the charge collection process, as well as the accuracy of the calculated weighting fields of the segments which are adjacent to the "open" surfaces.

As presented in chapter 4, the electrostatic field in the detector varies with the **concentration of the spatial charges** which exist in the depleted detector volume. These charges are formed at the places where impurities exist, and therefore, the distribution of the impurity concentration will determine the charge distribution, and consequently, will affect locally the electrostatic field. In the detector production, **variations of the impurity concentration** are normally unavoidable. An accurate determination of this distribution will help for a better estimation of the local electrostatic field. Furthermore, the variation of the impurity concentration in the normal operation time of the detector is of concern, especially if the detector is exposed to neutrons in in-beam experiments with fusion-evaporation reactions.

The theoretical estimation of the **charge carrier drift velocity** and its variation with the electric field is still an approximation. Moreover, if during the operation of detector, variations of the bias voltage or temperature exist, the electrons and holes will change their drift velocities, inducing different signals.

Electronical shaping of the detector signal and noise. The influence of the **limited preamplifier bandwidth** on the shapes of the detector segment signals has been already discussed in section 5.5. This is an important limitation, since valuable information which exist in the detector signal will be lost in the preamplifier output signal. Moreover, the unavoidable **detector and electronics noise** will further disturb the signal shapes.

Consequences

Due to uncertainties in the charge collection process, the assumptions taken for pulse shape simulations used in creating the database of patterns have to be checked and directly compared with experimental values. By measuring experimental signals produced by single interactions in several well defined regions using a Compton spectrometer, the parameters used in the simulation can be corrected to adapt the experimental shapes. In this way, the distribution of the impurity concentration and the charge carrier drift velocity can be estimated.

Another possibility of getting around the missing knowledge in the signal shape formation, is to precisely scan the detector in its whole volume, and to directly use the experimental shapes in the data base of patterns. Eventually, for a more fine grid of signal types, interpolations can be made from the experimentally determined pulse shapes. Obviously, such a procedure is time-consuming, and not practical, when applied to a very large number of detectors, as would be required for a nuclear spectroscopy array. Anyhow, one of the two methods have to be applied since otherwise, if the drift of the electrons and holes are not known precisely for all interaction points within the detector, systematical errors can be made in position determination.

For single interactions, the position resolution will be also finite, the ultimate limitation being the dimension of the charge carrier clouds. Besides this, depending on the local variations of the signal features, which can have different discriminatory degrees for different positions, the positioning precision will vary for various interaction locations. Finally, the S/N ratio of the detected signal, which is a function of the deposited energy, will influence also the precision of the positioning. Ultimately, the signal-to-noise ratio S/N can be improved by reducing the noise, by an improved design of the analog section of the electronics, and by using sampling ADC's with a larger number of bits.

For multiple interactions, due to the distribution of the charge carrier clouds, electronic noise and preamplifier shaping, the decomposition of the signals will be a mathematical ill-posed problem. Especially for interactions lying close together, for other particular combinations of interactions, it will not be possible to decompose them uniquely. In principle, this limitation has to be considered in the design of an optimized tracking algorithm. Moreover, to optimally extract the available information by pulse shape analysis, a Bayesian approach for the decomposition of multiple interactions can be followed by taking into account the statistics of the γ-ray scattering process. Thus, the distribution of the multiple interactions can be estimated by calculating an a-priori probability using the known released energies. This information can then be included in the pulse shape analysis methods to estimate the relative positions and energies of the interactions.

5.6.3 Identification of single interactions

Creation of a data-base with pattern classes

The aim of the statistical pattern recognition is to determine to which class a given object belongs [67]. The same problem has to be solved here. In general, to create a pattern recognition system, a "classifier design" is involved. In this process, data are collected, and the corresponding classes are formed, by *supervised* or *unsupervised* training. In the present case, the involved "classes" are very well known, and no "classifier design" is needed. Nevertheless, the creation of a data base containing the features of the classes still has to be made. In principle, for each detector segment, a particular data base has to be created. Since in the present case the design of the detector is fully symmetric, all the segments are the same, being characterized by the same weighting fields, hence a unique data base with pattern classes common to all detectors can be made. The edge effects of the detectors, and its corresponding inhomogeneities of the electric fields are not considered here. The data base was created by storing the wavelet transform coefficients of simulated pulse shapes. The positions taken for the pulse shape simulations were on a grid raster, with distances of 1mm between points. For the 8x1 fold segmented Ge detector, one single set of data was required, corresponding to grid points placed on a section of a disk in the azimuthal plane of the detector, starting at the median of the segment (0°) and finishing at the opposite border of the neighbouring segment (67.5°). Due to the symmetries involved in this design, the data stored from these points, are completely covering the variation of pulse shapes.

For the 8x4 fold segmented Ge detector, the characteristic pulse shapes vary with all three coordinates of the interaction position. Nevertheless, it was found that, in a good approximation, it is possible to store two reduced sets of data corresponding to two plane sections. One set includes data corresponding to pulse shapes obtained for interaction positions situated on a grid in a longitudinal median plane of segments, for various radii and longitudinal distances to the segment border, whereas the other set contains data corresponding to pulse shapes obtained for interaction positions situated on a grid in the azimuthal median plane of the segments, for various radii and azimuthal angles with respect to the segment border. Actually, there is a fine variation in the full 3D space, since the 2D segmentation breaks the longitudinal symmetry which exist in the 8x1 fold segmented detector. But since the variation of the induced shapes depends firstly on the interaction radius, and secondly on the distance between the collection point of the holes and the segment border, a full storage of the pulse shapes corresponding to all possible positions in 3D is redundant. This is the reason why the two sets of points are approximating all the possible pulse shapes of such a 3D system.

Calculation of the membership function

Once the data base containing the features of all pattern classes $\mathbf{C_j} = [c_1^j, c_2^j, ..., c_N^j]$ is produced, the determination of the class to which an unknown vector of features $\mathbf{X}[x_1^j, x_2^j, ..., x_N^j]$ corresponds, requires that a measure of similarity between the unknown vector $\mathbf{X}$ and the pattern vectors $\{\mathbf{C_j},\ j = 1, 2, ..., M\}$ has to be found. The measure of similarity between the vector $\mathbf{X}$ and the pattern vector $\mathbf{C_j}$, is named a *membership function*, and is written $m_j(\mathbf{X})$. In the above notations, N was used for the number of features for each class, and M for the number of pattern classes $\{P_j, j = 1, 2, ..., M\}$.

The definition of the membership function is related to the "distance" between the features of the unknown data $\mathbf{X}$ and its expected values in the pattern classes $\mathbf{C_j}$:

$$d(\mathbf{X}, \mathbf{C_j}) = \sqrt{\sum_{n=1}^{N} [W_n(x_n - c_n^j)]^2} \qquad (5.32)$$

where W_n is a parameter which weights each feature of the pattern. If all the features are considered to have the same importance in the membership calculation, then all weights W_n should be one. The membership function of the unknown pattern $\mathbf{X}$ to the pattern class P is determined as the inverse of the distance weighted as:

$$m_j(\mathbf{X}) = \frac{1}{1 + \left(\frac{d(\mathbf{X}, \mathbf{C_j})}{E}\right)^F} \qquad (5.33)$$

where E is an arbitrary positive constant, and F is an integer. These two constants have the effect of changing the variation of the membership function with the distance. For the present case it is assumed $E = 1$ and $F = 2$. One should note that the membership value is unity only if the separation distance is zero.

Identification algorithm in two-dimensions

As a simplified design, an eight-fold segmented Ge detector is considered. The segmentation takes place in the azimuthal direction, allowing a discrimination of the pulse shapes with different radii and azimuthal angles of interaction.

There are three main steps in the identification of a single interaction occurring in the detector. Firstly, by analyzing the deposited charge in each segment of the detector, it is determined in which segment the interaction took place. Having found the segment which "fired", the wavelet transform coefficients of the pulse shapes of the irradiated segment and its two neighbours containing mirror signals are forming three sets of unknown patterns. For the second step, the three unknown patterns are feed into a system which calculates the distance to the features of the pattern classes. For the irradiated segment, only the pattern classes corresponding to a "real charge" are considered, whereas for the neighbouring segments, only the ones corresponding to "mirror charges". This is normal since we expect to have a "real charge" in the irradiated segment, and "mirror charges" in the first neighbours due to the influence of the moving charge carriers on those segments. The minimum distance from vector X to the vectors C_j is calculated as:

$$d_{min}(\mathbf{X}, C_k^{type}) = \min_j \sum_{n=1}^{N} (x_n - c_n^{type,j}) \tag{5.34}$$

Of special interest is the pattern class P_k for which the distance is minimum. The word "*type*" stands in Eq. 5.34 for the type of signal which is expected, namely, *real* or *mirror*. One should point out again that each of the pattern class indices (j or k) correspond to clearly defined positions inside the detector, and are specific to the considered segment.

For each of the three segments, only the pattern classes P_k^{type} which fit best are memorized, and are correlated to each other in the third step of the analysis, which determines the final position of interaction by comparing the information obtained for the three segments. For this aim, a correlation matrix is used which contains as elements the index values of the interaction position, depending on the index of the "mirror charge" pattern classes $\{P_k^{mirror}, k = 1, 2, ..., M^{mirror}\}$ on one matrix dimension, and the "real charge" pattern classes $\{P_k^{real}, k = 1, 2, ..., M^{real}\}$ on the other. The calculation of the correlation matrix can be performed beforehand and used as a look-up table during the analysis process. In the calculation, the product between two membership values $m_{(i,k)}^{real}$ and $m_{(j,k')}^{mirror}$ is maximized. The first value represents the membership of the "real" signal of pattern class P_k^{real} to the class P_i^{real}, whereas the second represents the membership of the "mirror" signal of pattern class $P_{k'}^{mirror}$ to the class P_j^{mirror}. The "real" pattern coefficient k corresponds to the same physical position inside the detector as the "mirror" pattern coefficient k'. The correlation values will represent how good fit together a recognized interaction of index j from the "mirror" signal, to the recognized interaction of index i from the "real" signal:

$$Corr_{(i,j)} = \max_k [m_{(i,k)}^{real} * m_{(j,k'(k))}^{mirror}] \tag{5.35}$$

The index of k which determines $Corr_{(i,j)}$, is named l, and corresponds to the final interaction position obtained from the correlation of the "mirror" class j with the "real" class i. The figure 33 visualize an example of membership values obtained in an irradiated segment and its first neighbours due to one interaction. One can observe a better discrimination of the radial position than of the azimuthal angle, for the irradiated segment b as well as for the neighbours a and c. Since the signals in the irradiated segment are the same for interaction positions symmetric to the segment median, analyzing the signals from the irradiated segment alone does not allow to deduce in which half the interaction took place. Therefore, the correlation between the irradiated and neighbouring segments is absolutely necessary to determine the position of interaction. The results of the identification system are represented in Figure 34. Simulated pulse shapes covering the whole surface of the segment, con-

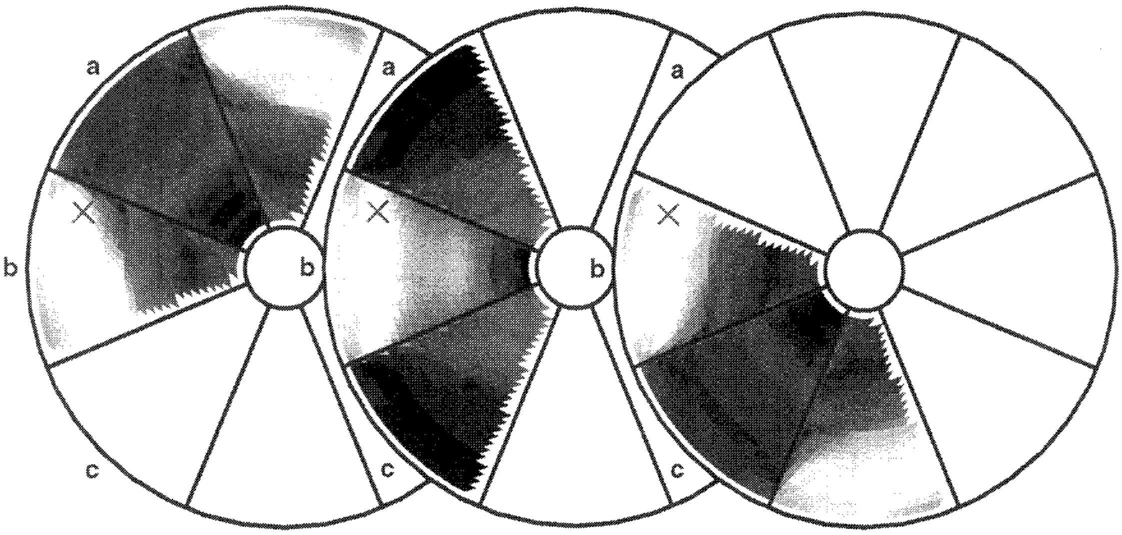

Figure 33 Surface plots of membership values for the segments *a*, *b* and *c* corresponding to a simulated single interaction, represented by the cross, in an 8x1 segmented detector. Lighter colors correspond to higher membership values. Here, the simulated interaction is noisefree.

taining three noise levels were feed into the system for position identification. For an added noise level of 1% from the total charge amplitude, the interactions are identified within 1mm in 80% of the cases. For the worst noise level of 5%, the interactions are identified within 2mm in 75% of the cases. Better positioning precision takes place for interactions close to the segment border, and worst toward the segment median, at intermediate radii.

Identification algorithm in three-dimensions

The use of a 2D segmented detector, gives the possibility to identify the interaction positions in full 3D coordinates, but it also rises problems, since longitudinal symmetries are broken, and the variation of pulse shapes with the position of interaction appears to be more complicated. For this case, another strategy will

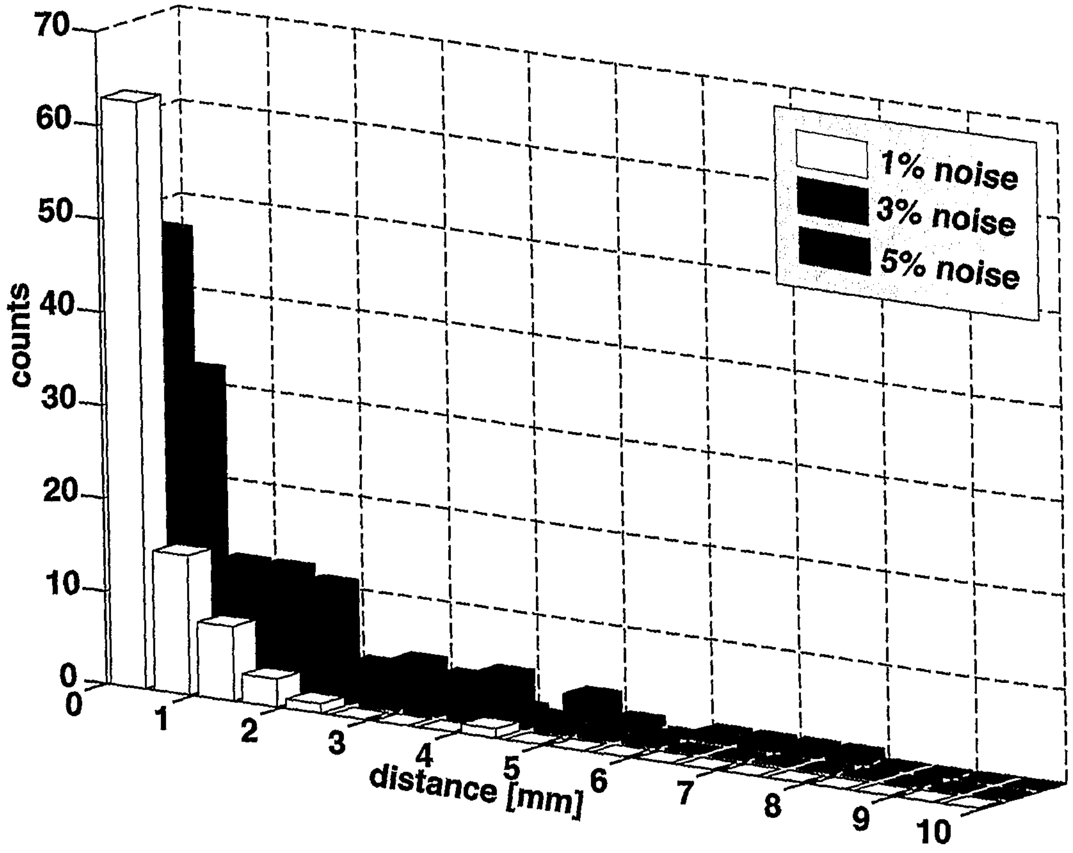

Figure 34 The position resolution in 2D for three noise levels.

be used than the one used in the algorithm for identification in 2D. The main idea followed here is that the power of the induced signals in the segments which are neighbours of the irradiated one decrease with the distance from the radial direction of the interaction point to the segment border. This feature will help to find the 3D coordinates of an interaction within a segment.

In the present case, an 8x4 fold segmented coaxial detector is taken. Its geometry and features are described in section 5.2.2. In principle, the identification algorithm used for this geometry has also 3 steps as in the 2D case. Although the first step is identical with the one described previously, involving only the identification of the irradiated segment, the second step is already different, where the best pattern class is found only for the signal of the irradiated segment. Once the pattern class has been found, the radius of the interaction point can already be inferred. Even if the determined pattern class will indicate also the distance to the segment border, the most reliable parameter which can be obtained at this stage is considered to be the radius. The step three, which determines the final position, is here completely different than the correlation method presented for the 2D case. The figure 35 gives an image about the features of the wavelet coefficients corresponding to signals induced in a 2D segmented detector. The figure presents two cases of interactions taking place at the same radius, at the same distance to the segment border, but in one case, close to the border with the neighbouring segment "South" -in the longitudinal direction-, and in the other case, close to the border with the neighbouring segment

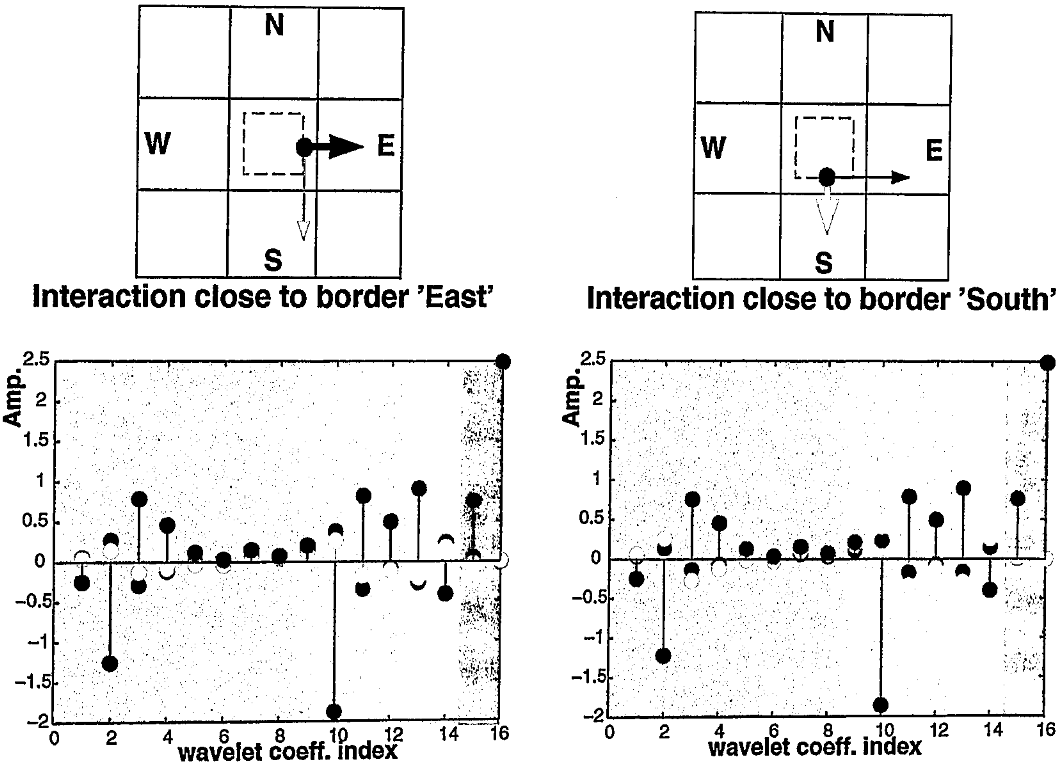

Interaction close to border 'East'

Interaction close to border 'South'

Figure 35 Picture of interactions occurring, left: close to the segment *East*, right: close to the segment *South*. In the upper portion the positions of interaction are shown, in the lower portion, the corresponding wavelet coefficients for the irradiated segment (green), for segment *East* (blue), and for segment *South* (red).

"East" -in the azimuthal direction- (see notations in the figure). The corresponding wavelet coefficients of the signal from the irradiated segment, displayed in the lower part of the figure, are almost identical for the two cases. The difference appears in the amplitudes of the wavelet coefficients of the neighbouring segments. There is also an approximate proportionality between the amplitude of the "real" wavelet coefficients $\mathbf{X}^{\mathbf{real}}$ and the amplitude of the corresponding "mirror" wavelet coefficients $\mathbf{X}^{\mathbf{mirror,E}}$ and $\mathbf{X}^{\mathbf{mirror,S}}$. Here, the indices E and S stand for *East* and *South.* If one calculates the projections of the "mirror" wavelet vector on the "real" wavelet vector, one gets the inner products:

$$\begin{aligned} A_E &= \langle \mathbf{X}^{\mathbf{mirror,E}}, \mathbf{X}^{\mathbf{real}} \rangle \\ A_S &= \langle \mathbf{X}^{\mathbf{mirror,S}}, \mathbf{X}^{\mathbf{real}} \rangle \end{aligned} \tag{5.36}$$

The normalized ratio:

$$Q_{E,S} = \frac{A_E - A_S}{A_E + A_S} \tag{5.37}$$

gives the measure which determines the position of the interaction relative to the two neighbouring segments. If the interaction takes place in a different quadrant of the segment, the segments which are neighbours with that quadrant will be considered. The variation of the parameter Q with the interaction position within the quadrant is common for all interaction radii, thus the values Q can be memorized in a data base, and used as a look-up table in the identification system.

5.6.4 Decomposition and identification of multiple interactions

The two-dimensional case

Due to the factors described in section 5.7.2, the decomposition of multiple interactions will not lead towards a unique solution. The number of interactions, their relative energies and positions are the free parameters which have to be found. The assumption on the number of interactions to be identified has to be made according to the Compton scattering statistics for the energies of interest. An assumed much larger number of interactions would be unphysical and besides, it would give a completely undetermined system, therefore constraints should be put to minimize the number of interactions intended to be identified. The main features of the processing flow are represented in fig. 36. It contains three major parts. Firstly, the irradiated segments are identified by determining the deposited energy. If the deposited energy is not zero, it can be concluded that at least one interaction took place in that particular segment. Then, for each irradiated segment and its neighbours, the pulse shape wavelet coefficients (the unknown pattern features) are identified with a procedure similar to the one described for identification of single interactions in 2D. If the obtained distance from the unknown pattern $\mathbf{X}$ to the identified pattern C_k is bigger than a threshold, it can be inferred that the pattern $\mathbf{X}$ contains more than one component. The next significant component is found in a second step, after an estimated amplitude of the already identified pattern $\mathbf{C_i}$ is subtracted from the vector $\mathbf{X}$:

$$\mathbf{X_{new}} = \mathbf{X} - A_i\mathbf{C_i} \tag{5.38}$$

The iteration can continue until all components are identified. In practice, the iterative procedure is interrupted if a reasonable number of components (4-5) is exceeded. Finally, the obtained pattern classes are correlated between the involved segments using the same correlation matrix as the one used for the identification of single interactions. Final positions are deduced and relative amplitudes representing the released energies are computed for segments with multiple interactions.

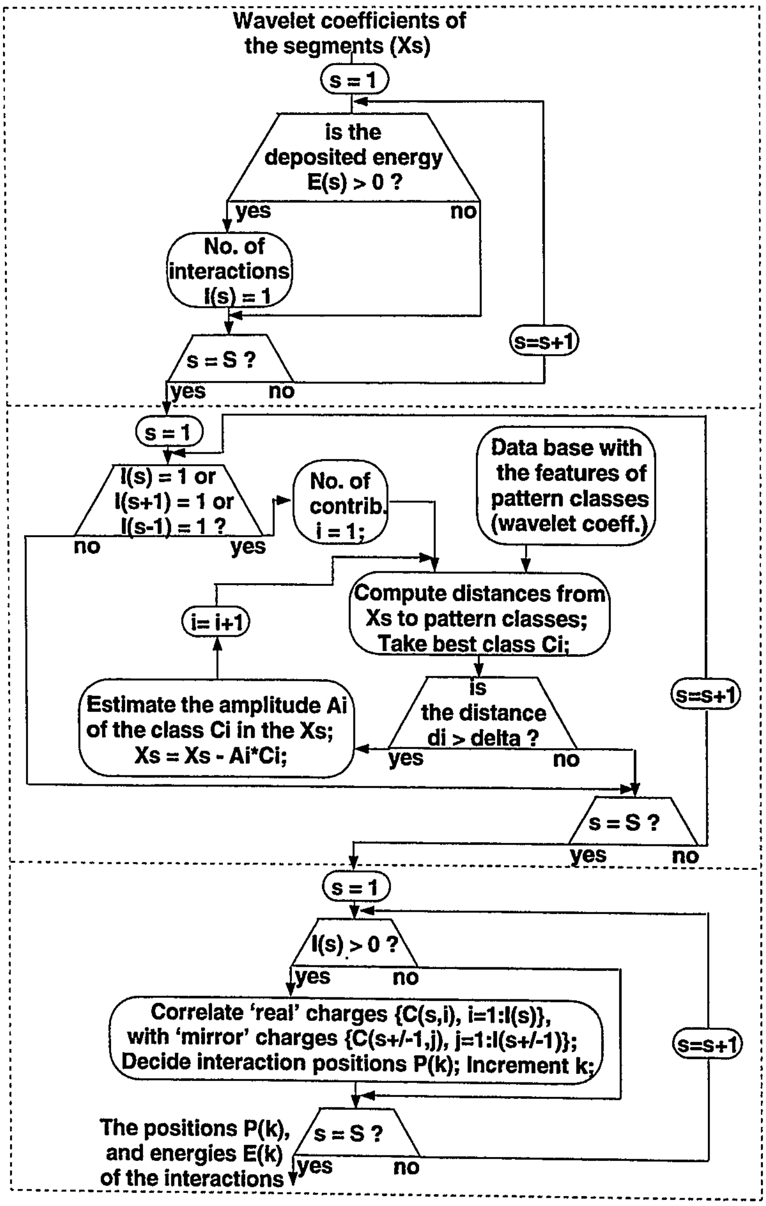

Figure 36 Flow diagram of the system for identification of multiple interactions in 2D. Notations: s = segment index; S = total number of segments; $E(s)$ = measured energy in segment s; $I(s)$ = No. of interactions in segment s; Xs = unknown pattern of segment s (the pulse shape wavelet coefficients); Ai = estimated amplitude of the pattern class Ci in the unknown pattern X; $delta$ = threshold for the distance di; $P(k)$ = the final interaction position;

The three-dimensional case

The most important aim of γ-ray tracking detectors is to provide the energies and positions of multiple interactions in full 3D coordinates. These values represent the experimental information needed for a tracking algorithm. The decomposition-identification system has a structure based on the algorithm for the identification of single interactions in 3D, modified to recognize multiple "real" signals, and to decompose the "mirror" signals.

Figure 37 pictures the simplified flow diagram of the identification system for multiple interactions in 3D. Similar in its main structural parts with the algorithm used in the 2D case, the algorithm was developed considering the simplicity required for an efficient on-line implementation. Similarly to the 2D case, firstly, the segments with deposited energies are identified. For each such segment, a number of "real" pattern classes C^{real} are extracted for the unknown pattern X. Having determined the number of "real" signal components, the segments in which "mirror" signals are expected due to these interactions can therefore be identified. For each such segment with "mirror" signals, a set of values $M(s', j) = \{s, i, Ci\}$ are memorized containing for each "mirror" signal of index j in the segment s', the corresponding "real" charge identified as Ci in the segment s. For each of these segments with "mirror" signals, having known the corresponding "real" signals, the induced amplitudes due to various interactions are decomposed. The amplitudes A_j are found by minimizing:

$$\left(\mathbf{X} - \sum_{j=1}^{J_s} A_j \mathbf{C_j}\right)^2 \tag{5.39}$$

For a superposition of two mirror charges, their amplitudes are determined by:

$$A_1 = \frac{\langle \mathbf{X}, \mathbf{C_1} \rangle - \langle \mathbf{C_1}, \mathbf{C_2} \rangle \langle \mathbf{X}, \mathbf{C_2} \rangle}{\langle \mathbf{C_1}, \mathbf{C_1} \rangle - \frac{\langle \mathbf{C_1}, \mathbf{C_2} \rangle^2}{\langle \mathbf{C_2}, \mathbf{C_2} \rangle}}$$

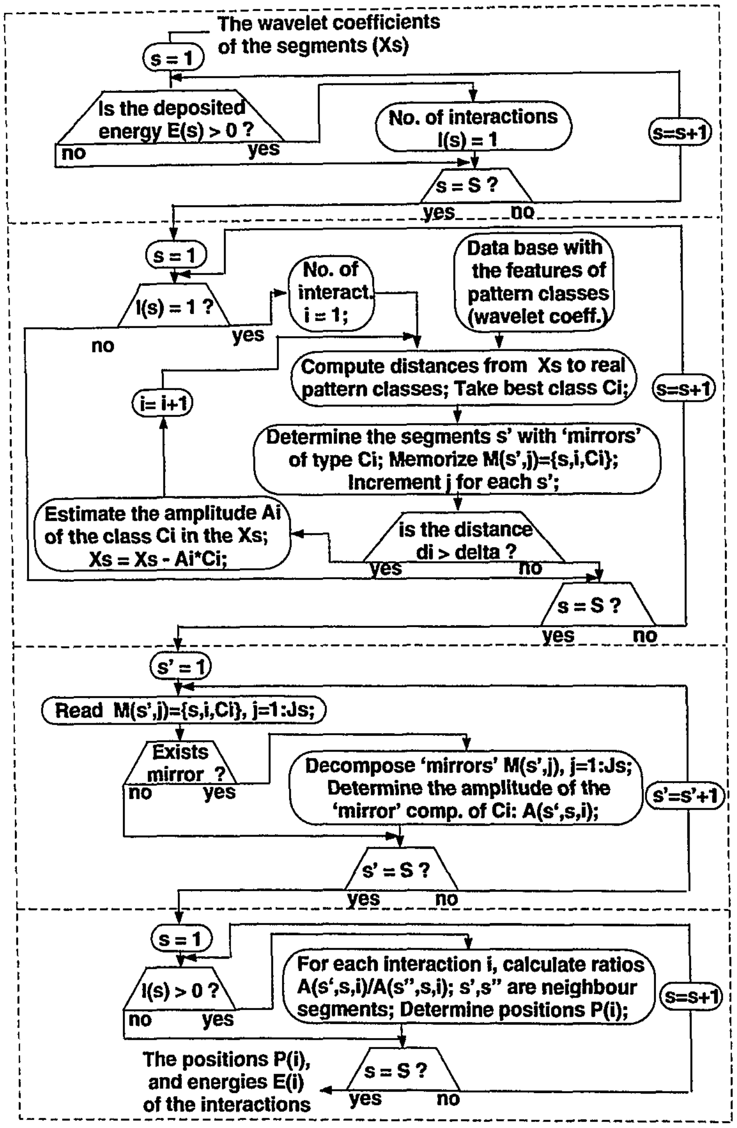

Figure 37 Flow diagram of the system for identification of multiple interactions in 3D. Notations: s = segment index; S = total number of segments; $E(s)$ = measured energy in segment s; $I(s)$ = No. of interactions in segment s; Xs = unknown pattern of segment s (the pulse shape wavelet coefficients); Ai = estimated amplitude of the pattern class Ci in the unknown pattern X; $delta$ = threshold for the distance di; $P(k)$ = the final interaction position; $M(s', j)$ = array of data containing for each 'mirror' signal j in segment s' the corresponding 'real' component Ci in segment s. Js' = no. of 'mirror' signals in segment s'; $A(s', s, i)$ = amplitude of 'mirror' in segment s', due to the 'real' component of index i in segment s.

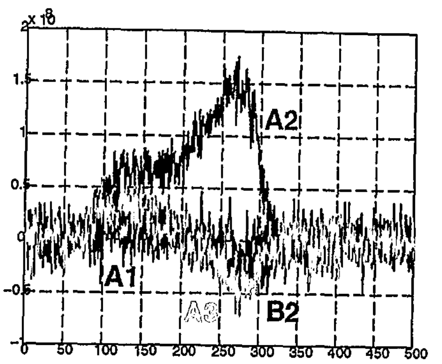

Signal shapes of the segments which are neighbours of the irradiated segment A2.

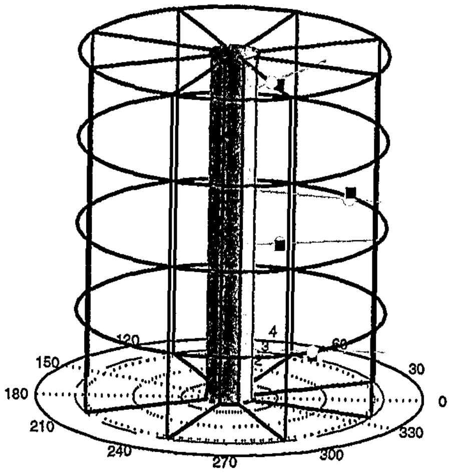

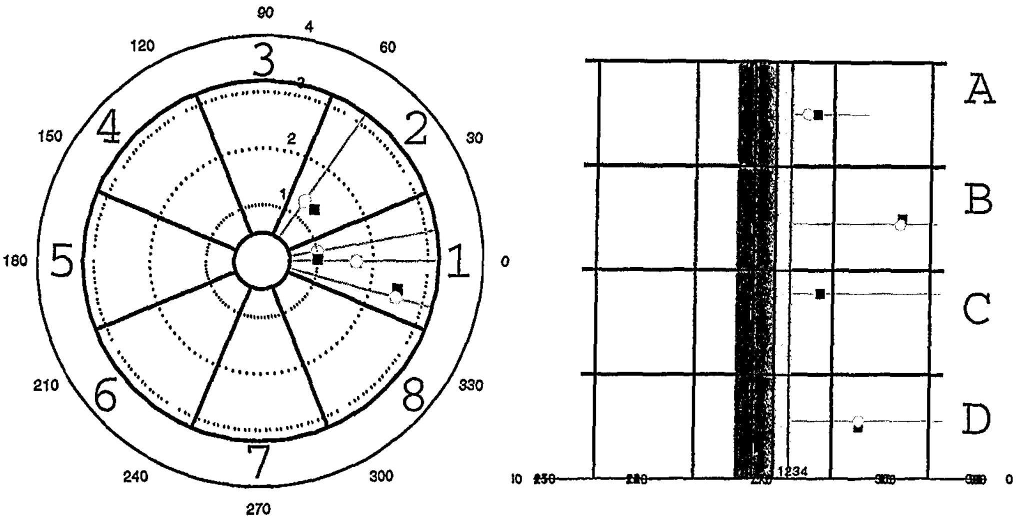

Top view **Side view**

Figure 38 Example of identification of multiple interactions in 3D.

$$A_2 = \frac{\langle X, C_2\rangle - \langle C_1, C_2\rangle\langle X, C_1\rangle}{\langle C_2, C_2\rangle - \frac{\langle C_1, C_2\rangle^2}{\langle C_1, C_1\rangle}} \tag{5.40}$$

An identification example is presented in fig. 38. A particular combination of four interactions were simulated and identified within 2mm. Various examples with different combinations of interactions were taken to test the identification system.

The complexity limit imposed in these examples involves a maximum number of one "real" and three "mirror" signal components per segment. The interactions are found with a much better precision in the radius than in the other directions. For segments being exposed to more components, the positioning resolution decreases, especially in the azimuthal and longitudinal coordinates.

5.6.5 Comments. Relations with the tracking algorithm.

The identification systems based on DWT coefficients were proven to work for particular cases. For a more general approach, the system has to be optimized along with the tracking algorithm, taking into consideration the scattering features of γ-rays. Since, as noted in the introduction, the decomposition of the signals is a mathematical ill-posed problem for multiple interactions, for determining the combination of scattered events, supplementary information has to be utilized by employing the statistics of the γ-ray scattering process. Thus, the combination of multiple interactions can be estimated by using the *Bayes theorem*, where the a-priori probability regarding the statistics of Compton scatterings is determined from the released energies. In our case, having denoted: the experimental data with X, the prior information about the scattering process with I, and the combination of interactions with C, the Bayes theorem is written:

$$P(C|XI) = \frac{P(X|CI)P(C|I)}{P(X|I)} \tag{5.41}$$

This can be understood as : the probability of having the combination of interactions C, given the experimental data X, and knowing the prior information I, is determined by the likelihood of having the experimental data X, given C and I, and the probability of having the combination C, given I. Since the result of this approach has to be meaningful for the tracking algorithm, and since it depends on the choice of the tracking concept, in the present study, the Bayesian approach was not further investigated.

CHAPTER 6

OTHER APPLICATIONS OF THE NEW TRACKING SYSTEM

6.1 Introduction

The presented tracking system based on large volume Ge detectors could offer unprecedented γ-ray imaging capabilities due to its high resolution in energy and position. Using this improved detection system, an accurate reconstruction of the Compton scattering sequence can be made, leading towards an improved imaging of γ-ray sources in the energy region from 100keV to 3MeV.

Three important pieces of information which are of interest for γ-ray imaging can be extracted. The main, most accurate information which can be obtained is the position of the first interaction. In most existing systems for γ-ray imaging, like Single Photon Emission Computed Tomography (SPECT) and Positron Emission Tomography (PET), this is the most important parameter. However, the position resolution offered by the normally used scintillators is not better than 4mm for a γ-ray energy of 511keV. Besides, the energy resolution which can be obtained with those scintillators is in the range of 5-10%, compared for example, with $\approx 0.2\%$ for Ge.

Using the proposed γ-ray tracking system, the γ-ray events with incomplete energy deposition can be identified. Having estimated the events with full energy deposition, a big reduction of the background can be made by rejecting the γ-ray events which Compton scattered out of the detection system.

The third kind of information obtained by tracking is the estimation of the direction of the incoming γ-ray to the precision of the cone surface determined by the scattering angle of the first Compton interaction in the detector system. Given the short distances between two Compton interactions in the Ge detectors, the precision of the scattering angle can not fulfill the requirements of a γ-ray telescope, for example, but, by increasing the statistics of the events, it can provide information about the position of a localized source within some reasonable solid angle. The precision for the determination of the scattering angle can be significantly improved by using a position-sensitive planar "scatterer" detector in front of the large volume Ge detectors. By operating the two detector systems in coincidence, and using the Compton scattered events from the "scatterer" to the Ge tracking array, a high precision of the scattering angle can be obtained.

Subsequently, a short description of three possible applications of γ-tracking Ge detectors will be made.

6.2 Industrial applications

6.2.1 Compton scattering tomography

The non-invasive investigations of materials made an important progress with the advent of tomographic methods. In particular, the Transmission Computed Tomography has found important uses in industrial applications.

For practical situations when, for the investigation of an object, the access to all sides of the object is limited, the concept of Compton scattering tomography (CST) was recently introduced [68]. Unlike the Conventional Transmission Tomography which is using the unscattered γ-rays to make a mapping of the internal density distribution in the sample material, the Compton scattering tomography is using the

Compton scattered γ-rays of a monoenergetic source to determine the distribution of the electron density in the sample material.

In conventional transmission tomography, the efficiency drops drastically if the energy of the used γ-ray source is increased, due to the predominance of the Compton scattering. For large volume, high-Z materials this is a sensitive problem, since the use of strong sources emitting high energy γ-rays are involved. In these situations, the CST concept would give the advantage of an improved scanning efficiency due to the fact that most of the scattered γ-rays are used in the reconstruction.

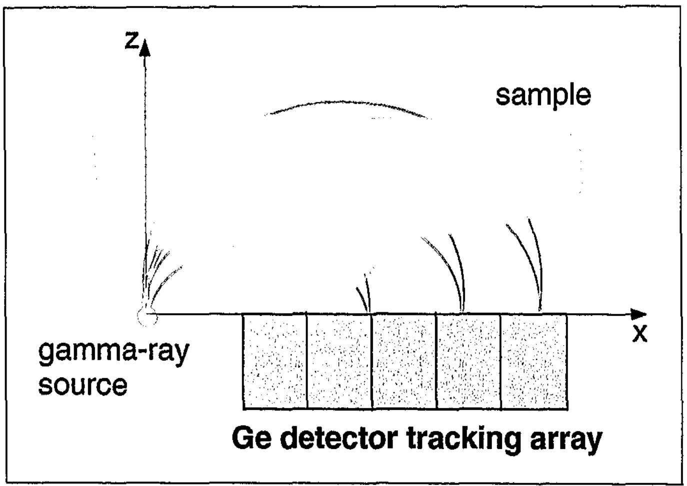

Figure 39 Concept of a Compton scanner using Ge detector tracking array.

To allow for a tomographic reconstruction using CST, a detection system with a high position and energy resolution is required. Actually, the imaging capabilities will depend on the precision to which the energy and position of the interaction can be measured. For a visualization of the working principle, figure 39 presents a detection system for Compton scattering tomography. A monoenergetic source is placed together with the Ge detector tracking array in close vicinity to the sample to be investigated. The γ-rays resulting from Compton scatterings in the sample are detected in the array.

Considering that the position at which the γ-ray hits the Ge detector and its energy can be accurately measured, an "isogonic" sphere can be calculated characterizing the spatial region in which the Compton interaction might have occured. The isogonic surfaces are represented in figure 39 by the red arcs. The γ-rays of energy E_d scattered at an angle θ are hitting the detector array at the position x_d. Assuming that the source is located at the origin of the coordinate system, the radius R of an isogonic sphere is determined by the position of interaction in detector x_d, and by the angle θ corresponding to the Compton scattering of a source γ-ray of energy E_0, having an energy E_d after scattering:

$$R = \frac{x_d}{2\sin\theta} \tag{6.1}$$

where the angle θ is determined by the Compton scattering formula:

$$\cos\theta = 1 - \frac{E_0}{E_d\left(1 + \frac{E_0}{m_0c^2}\right)} \tag{6.2}$$

For a scattered γ-ray detected at (x_d, y_d), the center of the sphere is given by the coordinates (x_0, y_0, z_0) as:

$$(x_0, y_0, z_0) = \left(\frac{x_d}{2}, \frac{y_d}{2}, \frac{-\sqrt{x_d^2 + y_d^2}}{2\tan\theta}\right) \tag{6.3}$$

The isogonic spheres will become the spatial "projections" which are used for the tomographic reconstruction method [69].

For the tomographic system explained, the use of an array of Ge tracking detectors would give an unprecedented resolution in both energy and position of the γ-rays, as well as a high efficiency for medium to high energy γ-rays. If the γ-ray scattered in the sample performs a Compton scattering in the Ge detector, then the direction of the impinging γ-ray can be determined with an improved accuracy by tracking, resulting in a limitation of the region of the sample in which the Comton scattering took place. An array of large volume Ge detectors as the one proposed in Chapter 5 would be most efficient for γ-rays which have energies larger than 400keV. For softer γ-rays, smaller planar position sensitive semiconductor detectors are more suitable [70, 71].

6.2.2 Imaging of unknown sources

There are many applications, especially related to environmental protection and radionuclide control of radioactive waste which require the identification of a compact radioactive source. In many of these situations, an exact image of the spatial distribution of the radioactive material is not necessarily required.

In this field, a single tracking Ge detector could be used as a compact, mobile device. Acquiring events with sufficient statistics, and electronically observing the superposition of the "Compton cones" determined by the tracking method, a fast decision can be made about the existence of a localized radioactive source. Then, by further increasing the statistics, the source can be identified within a finite solid angle. The term "Compton cone" refers to the virtual surface formed by all possible directions of the incident γ-quanta which give a certain Compton scattering angle θ, which can be determined by γ-ray tracking. The openning angle of the cone is determined by the angle θ, and its symmetry axis by the scattering direction.

6.3 γ-ray Astronomy

6.3.1 Astrophysical objectives

Much of the astronomical γ-ray data obtained up to now, are suffering from a poor energy and position resolution of the used detector systems. However, recent Compton scatter imaging instruments, like the COMPTEL spectrometer aboard NASA's COMPTON Gamma Ray Observatory (CGRO) satellite, were able to give a glimpse on several astronomical issues: An all-sky map of γ-rays in the 1-30 MeV energy range was produced, indicating a concentration of γ-ray emission from the galactic plane, which suggested that most of the γ-radiation comes from regions or objects inside the Galaxy. The ^{26}Al sources in the Galaxy, with a half-life of 700,000 years were mapped, revealing the distribution of relatively recent supernovae remnants in the Galaxy. Furthermore, the determination of the lines corresponding to ^{44}Ti, with a half-life of 60 years, allowed the discovery of new, very young supernovae remnants in the Galaxy. Other achievements include the map of the Orion Region in the 3-7 MeV range, an all-sky map of γ-ray bursts, study of pulsars and active galactic nuclei (AGN) [72].

Some of the astrophysical objectives involving γ-ray line spectroscopy were already addressed above, in the description of the COMPTEL results. In the following, a short overview on the major topics will be made.

The **accretion of matter** which takes place in cataclismic events, and some binary systems are sources of powerful X- and γ-ray emmissions. A characterisation of these sources would allow, for example, the identification of stellar black holes in a binary system.

The detection and characterization of a statistical number of **type Ia supernovae**, would allow a check and further refinement of the models developed to describe these catastrophic explosions of the dwarf stars. Moreover, the supernovae, being the brightest astronomical phenomena observed, serve also as distance indicators. According to the models, the type Ia supernovae should produce large quantities of ^{56}Ni, which emits γ-rays in the $^{56}Ni \rightarrow^{56} Co \rightarrow^{56} Fe$ β decay chain.

Refined observation of the supernova γ-ray lines, including the **type II supernovae**, will make possible a better understanding of the nucleosynthesis of heavy elements.

At present, two γ-ray lines which result from a **diffuse galactic emission** were detected. They are the 1,809keV line of ^{26}Al, which is believed to come from supernovae remnants, and the 511keV annihilation line. The sources appear to have a diffuse distribution in the galaxy. A high resolution γ-ray telescope would allow for an identification of other lines, providing valuable insights about the nuclear processes in the galaxy.

The γ-**ray pulsars** are young neutron stars, displaying maximum luminosity in the γ-ray energy range. For a characterisation of these objects γ-ray observations are crucial.

Measurement of γ-ray polarisation can provide powerful information in the study of solar flare emissions and accreting binaries.

Further astrophysical topics which can be approached with an improved γ-ray telescope are the detection of ^{22}Na and ^{7}Be expected to exist in **novae**, and the characterisation of γ-radiation emitted by the **Active Galactic Nuclei** (AGN).

6.3.2 Existing γ-ray telescopes

The instruments used for spectroscopy and imaging of astrophysical γ-ray sources are variations of three main detection concepts:

(i) The **Compton telescopes** work on the general principle of a Compton camera. They are formed by two position-sensitive detector arrays, a "scatterer" detector, which is a thin detector meant to Compton scatter the γ-rays, and an "absorber" detector, which has to detect the scattered γ-rays, by absorbing them. Using high-energy resolution detectors, these telescopes are powerful instruments providing good definition and large field of view. The most effective Compton telescope built is the COMPTEL telescope addressed above, which had as detectors a liquid scintillator (NE213) as scatterer and a NaI(Tl) scintillator as absorber [73]. With the improved energy and position resolution provided by Ge tracking detectors, a new Compton telescope can provide unprecedented capabilities.

For a given detector energy resolution, a higher imaging definition can be achieved either by improving the angular resolution of the first Compton scattering angle, requiring also a total absorption of the γ-ray, a scheme followed in the

COMPTEL instrument [73], or by requiring an exact determination of the energies and scattering angles of the first two Compton interactions [74]. In the second case a complete energy deposition is not required. Although a higher detection efficiency could be achieved, a disadvantage of the second approach is that if for the first three-four interactions two of them take place very close to each other and cannot be accurately discriminated, wrong results are obtained. This approach is followed by the Advanced Compton Telescope (ACT) project [75].

(ii) Although the imaging principle is different, the **coded aperture** (or modulated aperture) instruments are similar in design to the Compton telescopes, where the scatterer detector is replaced by a passive coded mask containing a pattern of holes made in a heavy material. In this way, the γ-radiation can be detected only if it passes through the holes. The coded mask provides the imaging capabilities of the telescope, by the shadows made on the detector arrays. Using a deconvolution algorithm on the shadowed images, it is possible to reconstruct the image of the source. A telescope of this type which is under development is the SPI telescope of the INTEGRAL project[76].

(iii) The **Laue diffraction telescopes** are using arrays of crystals to focus low energy X-rays of selected energy on a detector array. With a very small field of view, the Laue diffraction telescopes are suited for the observation of discrete sources with narrow lines.

6.3.3 A new γ-ray tracking telescope

The use of Ge tracking detectors would give an important advantage for the spectroscopic and imaging capabilities of a γ-ray telescope. With an improved energy and position resolution, they would give improved capabilities to a Compton telescope, if used as "absorber" detectors together with an array of high resolution thin planar Si or Ge detectors as scatterer. Figure 40 presents the schematics of such

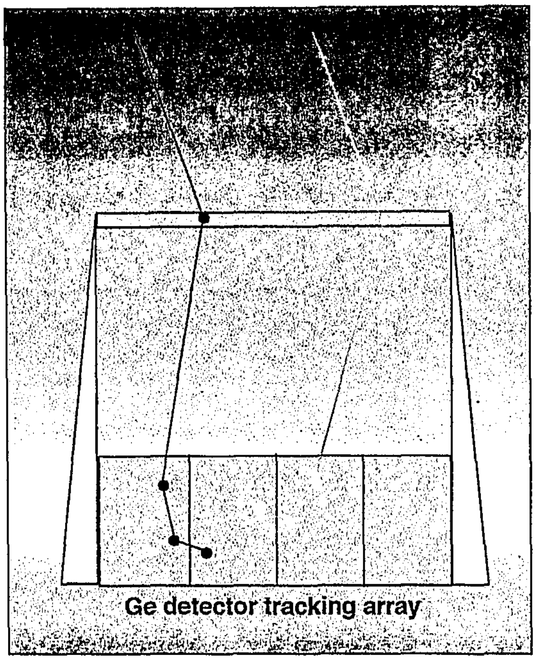

Figure 40 Schematics of a γ-ray telescope based on a Ge detector tracking array.

a system. Due to the tracking capabilities of the proposed Ge detector, an electronic background rejection will be also possible, avoiding in this way the need for heavy collimation. If γ-rays are detected by the absorber detector, but a coincident Compton event is missing in the scatterer detector, an approximate image of the source can still be made by using the concept presented in the previous section. For this mode of operation, a complete 4π field of view would be available.

6.4 Nuclear medicine: Positron Emission Tomography

6.4.1 Features of PET scanners

Positron Emission Tomography (PET) is a powerful imaging technique used in clinical and medical research applications [77]. The most important advantage of

PET in comparison with other imaging techniques is that it allows a visualization of the biological functions. Its role is expected to further expand with the advance of genetic research. By labelling certain genes and following their path, a functional characterization of the genes can be made.

The radiation which is used for such imaging techniques are the 511keV annihilation quanta of β^+ emitting nuclei. By labelling certain biological tracers with β^+ emitters like ^{18}F, ^{11}C, ^{13}N or ^{15}O, it is possible to observe the tracer path by a position sensitive detection of the coincidences of the two 511keV quanta emitted under an angle of 180°. Using coincidence events, tomographic reconstruction methods allow a determination of the spatial tracer distribution in the biological system [78]. The most popular detectors used for PET scanners are scintillators like bismuth germanate (BGO), and more recently, lutetium oxyorthosilicate (LSO). The PET detection system contains thousands of small such crystals placed usually in a ring around the investigated body.

For a good imaging capability, a high position resolution of the detectors is required. The high density scintillators refered above provide an acceptable position resolution. Unfortunately, due to their poor energy resolution, it is not possible to set a very accurate window on the 511keV peak. Since many of the γ-rays will Compton scatter in the sample, by the detection of scattered γ-rays in the large energy window, wrong coincidences will be counted. These are named *scattered coincidences* and contribute to a degradation of the image, since they indicate wrong positions of the γ-emitters. This is the main factor contributing to image degradation in PET scanners. With good timing characteristics, the negative effects induced by *accidental coincidences* are not of main concern.

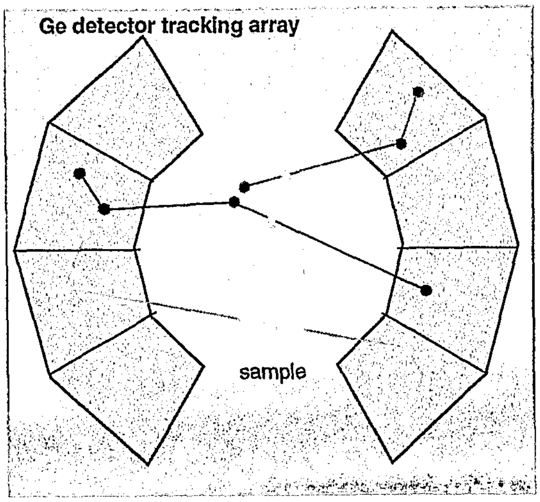

Figure 41 Schematics of a PET scanner based on a Ge detector tracking array.

6.4.2 A new scanner concept based on γ-ray tracking

A PET scanner employing high energy resolution detectors would have important advantages with regard to the scattered coincidences problem, being able to accurately identify the γ-rays Compton scattered in the sample. In this respect, the Ge tracking detector has the potential to accuratly measure the energy and position of the scattered γ-rays. By determining the coincident scattered γ-rays with a good energy resolution, it becomes possible to use also these events in the tomographic reconstruction method, by using the principle of Compton scattering tomography presented in section 6.2.1. On the other hand, its good position resolution will make possible to improve the imaging characteristics of the present-days PET scanners. Figure 41 presents a simplified scheme of a PET scanner employing Ge tracking detectors. Three events representing different possible event cases are also shown. The position resolution in depth of the Ge tracking detector gives the possibility to correct for parallax errors which are not corrected in presently available PET scanners. With a lower precision, also non-coincident single events can be used for a rough but fast estimation of the tracer position by using the tracking of the γ-rays in the detector.

All these facts will lead towards an improved efficiency of the scanner, having as main consequence a reduced dose. In a first development phase, such an instrument could become of special importance for small research PET systems, where an improved imaging sensitivity is required.

CHAPTER 7

CONCLUSIONS

A superior γ-ray detector array is required for the study of new challenging nuclear structure topics, especially of the nuclear structure under extreme conditions of spin, isospin and temperature. Detection systems based on γ-ray tracking concepts are the next logical step in the development of spectroscopic methods. A γ-ray tracking system will consist of an array of highly-segmented Ge detectors and digital signal processing electronics for pulse shape analysis, which allows for the detection of the γ-ray interactions with a high energy and position resolution. A reconstruction of events will be possible by determining the Compton scattering sequences utilizing tracking algorithms.

For an efficient γ-ray tracking, dedicated detectors have to be developed. Considering present days technologies, the best performance will be obtained with large coaxial Ge detectors which need to have segmented electrodes.

Features of the charge collection process in Ge have been studied. Measurements of detector pulse shapes have shown the anisotropic character of the charge carrier drift velocity. It was demonstrated for the first time that this effect has to be taken into account in the analysis of Ge detector pulse shapes for position determination. A model for realistic calculations of the electron drift velocity has been developed for the electric fields and temperatures of interest. Furthermore, programs to simulate realistic pulse shapes in segmented Ge detectors have been made.

The main objective of this work was to find out whether the position resolution required for γ-ray tracking can be achieved by employing digital signal processing methods. Pulse shape analysis methods for position identification in medium segmented Ge detectors were developed. Furthermore, new digital algorithms for event triggering and timing were created. The on-line implementation of the timing algorithm on a digital signal processing electronics provided a time resolution similar to the one obtained with analog electronics. For a full dynamic range, a FWHM of 8.5ns was obtained with the developed Normalized Step Response (NSR) algorithm. Further improvements are foreseen.

For an efficient determination of the positions of γ-ray interactions by employing pulse shape analysis methods, a dedicated preprocessing of the digitized signal is required. In this context, concepts for preprocessing of the detector signals have been studied. The wavelet transform was finally choosen to process the detector signals, being able to emphasize their features. To find an optimum wavelet transform, their properties were studied in connection with our particular application. A "wide-band", small support wavelet transform (WB4) has been selected for the preprocessing of the pulse shapes of the detector signals. The subsequent algorithms for position determination gave best performances when the WB4 transform was used.

Finally, algorithms were developed for the determination of the interaction position of γ-rays in segmented coaxial Ge detectors for single and multiple interactions. Based on pattern recognition concepts, the algorithms were designed considering realistic experimental conditions. From simulations, a position resolution of up to 2mm is obtained even for very noisy signals. A proof of the possibility to decompose multiple interactions using a wavelet analysis was given. It was shown that the position resolution required for γ-ray tracking is achievable. Further work is required to improve the decomposition of multiple interactions, eventually in connection with the tracking algorithms.

Instruments using the proposed tracking detection system can find applications not only in γ-ray spectroscopy, but also in astronomy, medicine and industrial applications.

REFERENCES

[1] R. Lieder, Experimental Techniques in Nuclear Physics, ed. D.N. Poenaru and W. Greiner, W. de Gruyter Berlin, pp.137 (1997);

[2] I.Y. Lee, Nucl. Instr. Meth. in Phys. Res. A422,pp. 195(1999);

[3] A. Johnson, H. Ryde and J. Sztarkier, Phys. Lett. 34B, pp.605 (1971);

[4] R.M. Lieder and H. Ryde, Advances in Nuclear Physics 10, pp.1 (1978);

[5] P. Twin et al., Phys. Rev. Lett. 57, pp.811 (1986);

[6] P.J. Nolan et al., Ann. Rev. Nucl. Part. Sci. 45, pp.561 (1994);

[7] J. Gerl and R.M. Lieder, Eds., "EUROBALL III Proposal", GSI Darmstadt Report (1992);

[8] M.A. Deleplanque and R.M. Diamond, Eds., "GAMMASPHERE Proposal", Lawrence Berkeley Laboratory Report 5202 (1988);

[9] D. Bazzaco et al., "GASP proposal, Padova (1990)", in Proc. Workshop on Large Gamma-ray Detector Arrays, Chalk River, Canada, AECL-10163, pp.376 (1992);

[10] J. Eberth et al., Nucl. Phys. A520, pp. 669c (1990);

[11] D. Bazzaco, Proceedings of the TMR user meeting, Cologne (2000);

[12] J. van der Marel and B. Cederwall, Nucl. Instr. Meth. in Phys. Res. A437, pp.538-551 (1999);

[13] G. J. Schmid et al., Nucl. Instr. Meth. in Phys. Res. A430, pp.69-83 (1999);

[14] P.N. Luke et al., IEEE Nucl. Sci. Symp. Conf. Record, (1999);

[15] J. Singh, Physics of Semiconductors and Their Heterostructure, McGraw-Hill, (1993);

[16] K. Siegbahn (editor), "Alpha-, Beta- and Gamma-ray Spectroscopy, vol. 1, North-Holland Publ. Co., Amsterdam, (1965);

[17] The MAFIA Colaboration, The static solver (1994);

[18] G. F. Knoll, Radiation Detection and Measurement, Wiley (1989);

[19] W. Shokley, Phys. Rev 78, pp.173 (1950);

[20] G. Dresselhaus, A. F. Kip and C. Kittel, Phys. Rev. 98, pp.368 (1955);

[21] E. O. Kane, J. Phys. Chem. Solids 1, pp.249 (1957);

[22] S. H. Groves and W. Paul, Phys. Rev. Lett. 11, pp.194 (1963);

[23] E. O. Kane, J. Phys. Chem. Solids 1, pp.82 (1956);

[24] S. Bosi, C. Jacoboni and L. Reggiani, J. Phys. C12, pp.1525 (1979);

[25] M. Shibuya, Phys. Rev. 99, pp.1189 (1955);

[26] H. G. Reik and H. Risken, Phys. Rev. 126, pp.1737 (1962);

[27] M. I. Nathan, Phys. Rev. 130, pp.2201 (1963);

[28] C. Jacoboni and L. Reggiani, Rev. Mod. Phys. 55, pp.645 (1983);

[29] W. Sasaki and M. Shibuya, J. Phys. Soc. Japan 11, pp.1202 (1956);

[30] W. Sasaki, M. Shibuya and K. Mizuguchi, J. Phys. Soc. Japan 13, pp.456 (1958);

[31] S. H. Koenig, M. I. Nathan, W. Paul and A. C. Smith, Phys. Rev. 118, pp.1217 (1960);

[32] G. Ottaviani, C. Canali and A. Alberigi Quaranta, IEEE Trans. on Nucl. Sci. NS-22, pp.192 (1975);

[33] L. Mihailescu et al., Nucl. Instr. Meth. in Phys. Res. A447, pp.350(2000);

[34] C. Canali, G. Ottaviani and G. Majni, Solid State Comm. 15, pp.1213 (1974);

[35] L. Reggiani, C. Canali, F. Nava and G. Ottaviani, Phys. Rev. 16B, pp.2781 (1977);

[36] L. Reggiani, Phys. Rev. 17B, pp.2800 (1978);

[37] A. Neukermans and G. S. Kino, Phys. Rev. 7B, pp.2693 (1973);

[38] M.A. Omar, L. Reggiani, Solid State Electronics 30, pp.1351 (1987);

[39] V. Radeka, Ann. Rev. Nucl. Part. Sci. 38, pp.217 (1988);

[40] E. Gatti et al., Nucl. Instr. and Meth. 193, pp.651 (1982);

[41] J. Blair et al., Nucl. Instr. Meth. Phys. Research A 422, pp.331-336 (1999);

[42] F.S. Goulding and D.A. Landis, IEEE Trans. Nucl. Sci., NS-29, No.3, pp.1125, (1982);

[43] J. Eberth et al., Prog. in Part. and Nucl. Phys., 38, pp. 29 (1997);

[44] C. Gund, "The sixfold segmented MINIBALL module. Simulation and experiment", PhD thesis, MPI-K Heidelberg, (2000);

[45] D. Bazzacco et al., "Test of the MARS prototype segmented germanium detector", LNL Annual reports, (1999);

[46] M.A. Deleplanque et al. Nucl. Instr. Meth. in Phys. Res. A430 (1999) 292-310

[47] K. Vetter et al., Nucl. Instr. Meth. in Phys. Res. A452 (2000) 105-114

[48] A. Georgiev and W. Gast, IEEE Trans. Nucl. Sci., 40, No. 4, 770 (1993);

[49] A. Georgiev et al., IEEE Trans. Nucl. Sci., 41, No. 4, 1116 (1994);

[50] G. Ripamonti, Proc. of TMR User Meeting, Padova (1998);

[51] W. Gast et al., Proceedings of the IEEE (2000);

[52] D.A. Gedcke and W.J. McDonald, Nucl. Instrum Meth.55,377 (1967);

[53] R. Craig Olson, Handbook of Pattern Recognition and Computer Vision, World Scientific Publishing Co., pp.541-568 (1993);

[54] D. Gabor, J. of IEE, vol. 93, pp.429-457 (1946);

[55] I. Daubechies, "Ten lectures in wavelets", SIAM

[56] S. Mallat, Trans. of American Math. Soc. 315, pp.69-87 (1989);

[57] G. Strang and T. Nguyen, Wavelets and Filter Banks, Wellesley-Cambridge Press, (1996);

[58] W.M. Lawton, J. Math. Phys. 32(1), (Jan. 1991);

[59] O. Rioul and M. Vetterli, IEEE Signal Proc. Magazine, pp.14-38, (oct. 1991);

[60] D.L. Donoho and I.M. Johnstone, Biometrika, 81, 3, pp.425-455 (1994);

[61] A. Aldroubi and M. Unser, "Wavelets in medicine and biology ", Boca-Raton,FL : CRC Pr. , (1996)

[62] S. Mallat, Proceedings of the IEEE, 84, no.4, pp.604-614 (1996);

[63] K. Yomogida, Geophys. J. Int. 116, pp.119-130, (1994);

[64] J. Liang and T.W. Parks, IEEE Trans. Image Process., 7 ,no. 5, pp.762-769 (1998);

[65] S. Mallat, IEEE Trans. on Pattern Analysis and Machine Inteligence, 11(7), pp.674-693 (1989);

[66] H.L. Resnikoff, AWARE Inc. Tech. Rep. AD9000810 (1989);

[67] K. Fukunaga, "Introduction to Statistical Pattern Recognition", New York: Academic Press, (1973);

[68] S.J. Norton, Journal of Applied Physics, 76, no. 4, pp.2007-2015 (1994);

[69] S.J. Wilderman et al., IEEE Trans. on Nucl. Sci., 45, no.3, pp. 957-962 (1998);

[70] B.L. Evans et al., IEEE Trans. on Nucl. Sci., 45, no.3, pp.950-956 (1998);

[71] J.W. LeBlanc et al., IEEE Trans. on Nucl. Sci., 45, no.3, pp.943-949 (1998);

[72] J.D. Kurfess, IEEE Transactions on Nuclear Science, 45, no.3,pp.936-942 (1998);

[73] V. Schönfelder et al., Astrophys. J. Suppl. 86, pp.657-692 (1993);

[74] J.D. Kurfess et al., "Considerations for the Next Compton Telescope Mission", 5th Compton Symposium, Portsmouth, New Hampshire, AIP Conference Proceedings, (1999);

[75] R.A. Kroeger et al., "Position Sensitive Germanium Detector for the Advanced Compton Telescope", 5th Compton Symposium, Portsmouth, New Hampshire, AIP Conference Proceedings, (1999);

[76] P. Madrou et al., ESA SP-382, pp.591-598 (1997);

[77] B. Bendrie and D.W. Townsend, eds., "The theory and practice of 3D PET", Kluwer Academic Publishers, (1998);

[78] D.W. Townsend and M. Defrise, "Image Reconstruction Methods in Positron Tomography", Lectures given in the academic training program of CERN, RD/904-2000-juin. Geneva (1993);

Forschungszentrum Jülich

Jül-3871
Mai 2001
ISSN 0944-2952